

QUANTUM CHAOS: SPECTRAL FLUCTUATIONS AND OVERLAP
DISTRIBUTIONS OF THE THREE LEVEL LIPKIN-MESHKOV-GLICK MODEL

Thesis by
Dawn C. Meredith

In Partial Fulfillment of the Requirements
for the Degree of
Doctor of Philosophy

California Institute of Technology
Pasadena, California

1987

(Submitted May 11, 1987)

Acknowledgements

I am grateful for the help, advice, and encouragement of my friends: Anne Alder, Ted Allen, Mary Barsony, Malcolm Butler, Ming Chu, Ruth Erlanson, Sam Finn, Mark Muldoon, Volker Pönisch, James Theiler, Dave Wasson, Roy Williams, Elizabeth Wood, and Cathleen Woodward.

I would especially like to thank Prof. Steve E. Koonin and Dr. Martin Zirnbauer, without whose help this thesis would not be possible.

This work was supported by the National Science Foundation. Computational work was done on the San Diego Supercomputing Center CRAY X-MP.

Abstract

We test the prediction that quantum systems with chaotic classical analogs have spectral fluctuations and overlap distributions equal to those of the Gaussian Orthogonal Ensemble (GOE). The subject of our study is the three level Lipkin-Meshkov-Glick model of nuclear physics. This model differs from previously investigated systems because the quantum basis and classical phase space are compact, and the classical Hamiltonian has quartic momentum dependence. We investigate the dynamics of the classical analog to identify values of coupling strength and energy ranges for which the motion is chaotic, quasi-chaotic, and quasi-integrable. We then analyze the fluctuation properties of the eigenvalues for those same energy ranges and coupling strength, and we find that the chaotic eigenvalues are in good agreement with GOE fluctuations, while the quasi-integrable and quasi-chaotic levels fluctuations are closer to the Poisson fluctuations that are predicted for integrable systems. We also study the distribution of the overlap of a chaotic eigenvector with a basis vector, and find that in some cases it is a Gaussian random variable as predicted by GOE. This result, however, is not universal.

TABLE OF CONTENTS

Acknowledgments	ii
Abstract	iii
Table of Contents	iv
List of Figures	vi
I Introduction	1
II Classical Systems from Regular to Random	
2.1 Integrable Systems	6
2.2 Surfaces of Section and Classical Perturbation Theory	8
2.3 KAM and Poincaré-Birkhoff Theorems	12
2.4 Lyapunov Exponents and Entropy	16
2.5 Degrees of Irregularity	23
III Random Matrix Theories	
3.1 Motivations	37
3.2 Derivation of Matrix Ensembles	40
3.3 Global vs. Local Behavior	45
3.4 Spectral Fluctuations	47
3.5 Eigenvector Distributions	50
3.6 Ergodicity and Stationarity	52
3.7 Comparison with Experiment	53
IV Quantum Chaos	
4.1 Billiards	60
4.2 Transition from Regular to Irregular Spectra	62
4.3 Semiclassical Results	64

V Three Level Lipkin-Meshkov-Glick Model

5.1 Motivations	76
5.2 Classical Limit	80
5.3 Chaos in the Classical Limit	86
5.4 Quantum Calculations	92
5.5 Density of States	95
5.6 Spectral Fluctuations	97
5.7 Overlap Distributions	106
VI Summary And Conclusion	141
Appendix	145
References	150

List of Figures

Figure 2.1: Motion on a Two-torus	27
Figure 2.2: Surface of Section	28
Figure 2.3: Surface of Section for the Toda Lattice	29
Figure 2.4: Surface of Section for the Henon-Heiles Potential	30
Figure 2.5: Twist Mapping	31
Figure 2.6: Illustration of Poincaré-Birkhoff Theorem	32
Figure 2.7: Changes in Invariant Tori under Perturbation	33
Figure 2.8: Phase Space of a Nonintegrable Hamiltonian	34
Figure 2.9: Wild Behavior of Separatrices	35
Figure 2.10: Stretching and Non-stretching Flows	36
Figure 3.1: Ensemble Averages for Finite and Infinite N	56
Figure 3.2: Spacing Distributions for Three Ensembles	57
Figure 3.3: Comparison of GOE Spectral Fluctuations with the Nuclear Data Ensemble	58
Figure 3.4: Comparison of GOE Strength Fluctuations with Nuclear Data	59
Figure 4.1: Symmetries of Circular, Sinai, and Stadium Billiards	68
Figure 4.2: Defocusing in Sinai's Billiard	69
Figure 4.3: Nodes of the Wavefunction for Stadium Billiards	70
Figure 4.4: Comparison of GOE with Stadium and Sinai Billiards Spectral Fluctuations	71
Figure 4.5: Comparison of GOE with Circular and Stadium Billiards	72
Figure 4.6: Transition from Irregular to Regular Spectra	73
Figure 4.7: $P(s)$ when Phase Space Is Not Ergodic	74
Figure 4.8: Δ_3 Statistic for Rectangular Billiards	75

Figure 5.1: Schematic Illustration of the Lipkin Model	109
Figure 5.2: Potential Energy Surface of the Classical Lipkin Model	110
Figure 5.3: Running Lyapunov Exponent	115
Figure 5.4: Chaotic Volume for $\chi = 100$	116
Figure 5.5: Classical Density of States for $\chi = 0.75, 100$	117
Figure 5.6: Comparison of Classical and Quantum Density of States	118
Figure 5.7: Checks on Nearest Neighbor Distribution $P(s)$	119
Figure 5.8: $P(s)$ for Chaotic Eigenvalues	120
Figure 5.9: $P(s)$ for Quasi-Chaotic Eigenvalues	121
Figure 5.10: $P(s)$ for Quasi-Integrable Eigenvalues	122
Figure 5.11: $P(s)$ for all Symmetry and Dynamics Classes	123
Figure 5.12: Checks on the Δ_3 Statistic	124
Figure 5.13: More Checks on the Δ_3 Statistic	125
Figure 5.14: Δ_3 for Different Dynamics Classes	126
Figure 5.15: Δ_3 for Different Symmetry Classes	127
Figure 5.16: Chaotic Volume for $\chi = \infty$	128
Figure 5.17: $P(s)$ for ooo Symmetry Class, $\chi = \infty$	129
Figure 5.18: $P(s)$ for eee Symmetry Class, $\chi = \infty$	130
Figure 5.19: Δ_3 for ooo Symmetry Class, $\chi = \infty$	131
Figure 5.20: Δ_3 for eee Symmetry Class, $\chi = \infty$	132
Figure 5.21: Convergence of the Running Lyapunov Exponent	133
Figure 5.22: Saturation of the Δ_3 Statistic	134
Figure 5.23: Overlaps of Chaotic Eigenvectors	135
Figure 5.24: Overlaps of Quasi-Chaotic and Quasi-Integrable Eigenvectors	136
Figure 5.25: Overlaps of Different Symmetry Class Eigenvectors with Basis Vector $\lambda = 500$	137
Figure 5.26: Overlaps of Different Symmetry Class Eigenvectors with Basis Vector $\lambda = 451$	138

Figure 5.27: Overlaps of Different Symmetry Class Eigenvectors with Basis Vector $\lambda = 823$	139
Figure 5.28: Trajectories and Surfaces of Section for the LMG model	140

Chapter One

Introduction

Nonlinear (irregular, chaotic) systems have been overshadowed by the solvable (integrable, regular) systems in the study of classical mechanics. In classes we study the harmonic oscillator, Keplerian systems, linearly coupled oscillators, and one dimensional systems. Texts give no indication that these regular systems are an unfair representation of Hamiltonian systems: for most Hamiltonian systems we cannot solve for $\vec{x}(t)$ as $t \rightarrow \infty$. This is true even for a system as simple as a single particle in a two-dimensional potential well. In fact, most Hamiltonians give rise to deterministic yet (practically) unpredictable long time behavior.

A simple example of unpredictability in a deterministic system is seen in the left shift map which takes the interval $[0,1)$ onto itself:

$$x_{n+1} = 2x_n \pmod{1}.$$

If we write a number in this interval in binary form

$$x_0 = .000101100101000011\dots,$$

the map shifts the digits one place to the left and drops the digit to the left of the decimal place. If we know a particular x_0 to n digits, we know the trajectory for n iterations, but after that we lose all powers of prediction.

The precision of the initial conditions plus the information entropy of the system determine how far our powers of prediction reach. (Information entropy is a measure of information gain which results in loss of precision; it is unrelated to thermodynamic entropy. See §2.4.) If we had either infinite precision, or a system with no information gain, all deterministic systems would indeed be predictable.

Integrable systems are zero-entropy systems - systems with no information gain, and so the myth of predictability took hold.

This practical unpredictability has its origin in a more fundamental concept. Consider the left shift map again: if x_0 and y_0 are equal to n digits, their trajectories will be close for n iterations; after that they will be completely uncorrelated. This instability with respect to initial conditions is chaos. In the first chapter we will make this intuitively appealing definition quantitative.

The presence of chaos changes the questions a physicist might ask. We do not ask for $\vec{x}(t)$ for arbitrary t . Even if we wished to work hard enough to find $\vec{x}(t)$, the solution would depend very sensitively on initial conditions. We would have found the solution for one point, and it would not give us any clues about the solution for nearby points. This work is too hard and the results too limited to make this the correct approach. Instead, the relevant physics questions for a chaotic system pertain to the topology of the phase space as defined by the trajectories: Do single trajectories cover all space, or do they lie on submanifolds? How much of phase space is covered by chaotic trajectories? The methods used by nonlinear dynamicists to describe and quantify phase space are also discussed in the first chapter.

A dominant feature of classical phase space are the invariant submanifolds defined by trajectories. For integrable systems with N degrees of freedom these submanifolds are N dimensional. In the phase space of the action-angle variables, these surfaces have the topology of an N -torus (§2.1), and are defined by the N action variables I_k which remain constant on each torus. For integrable systems all phase space is filled by these tori, but as a perturbation is added some tori distort, while others disappear and are replaced by island chains and chaotic regions.

These tori are important for quantum mechanics as well. According to Einstein, Brillouin, and Keller, we quantize the system by demanding that the actions are quantized:

$$I_k = (n_k + \text{constant})\hbar .$$

If there are no tori, there are no actions and no good quantum numbers. This line of reasoning led Percival [Pe73] to hypothesize that the spectra of integrable and non-integrable systems would be completely different. This was the beginning of quantum chaology.

Percival dubbed the two different spectral types as regular (corresponding to integrable classical analog) and as irregular (corresponding to a non-integrable analog). However, this difference was qualitative only; he offered no quantitative tests to distinguish the two spectral types. It was not until a few years later that Berry and Tabor [BT77] quantified the differences between regular and irregular spectra. They looked at $P(s)$ - the probability that two consecutive energy levels are a distance s apart; they adapted this approach from the nuclear physicists' statistical theory of spectra.

This statistical theory is a subject in its own right [Br81]. It began in the 1950's, and grew out of a need to predict the highly excited levels of heavy nuclei which could not be calculated using traditional techniques, e.g., shell model calculations. In analogy with statistical mechanics they used ensembles. The thought was that nuclei were so complicated that a statistical approach was viable. These were not ensembles of points in phase space, but ensembles of random Hamiltonians, i.e., real symmetric matrices whose elements are chosen from a distribution. Using an ensemble, we can calculate ensemble averages of spectral fluctuation measures such as the nearest neighbor spacing distribution $P(s)$. The Gaussian Orthogonal Ensemble (GOE) was particularly useful because it allowed analytical calculations of fluctuation measures, although its relevance to real physical systems was in doubt. Then in 1982 a careful study of experimental neutron resonance levels from many nuclei showed GOE fluctuations [HBP82]; this revitalized Random Matrix Theory.

Because the statistical theory plays an important role in the description of quantum chaos, Chapter Two will be devoted to a discussion of the GOE, and Random Matrix Theory (RMT) in general.

Meanwhile, the quantum chaologists continued to focus on the nearest neighbor distribution $P(s)$. Their main subject was billiards, i.e., a single particle in a box. Depending on the shape of the box the classical analog was regular or chaotic. For regular spectra they found level clustering: $P(s)$ large for $s = 0$. For irregular spectra they found level repulsion: $P(s) \sim s$ for small s . Level repulsion is characteristic of the GOE. This observation, and the success of GOE in describing nuclear level fluctuations led Bohigas, Giannoni, and Schmidt [BGS84] to look at higher order correlations in the spectra of chaotic billiards. They found that these correlations were also in agreement with GOE. This was surprising because the complexity present in nuclei, which justified the statistical approach, was not present in the simple billiard. In conclusion, they suggested that there is a universality of the laws of level fluctuations: “Spectra of time-reversal invariant systems whose classical analogs are K [chaotic] systems show the same fluctuation properties as predicted by GOE.” [BGS84] Chapter Three will look at recent work in quantum chaos which supports this hypothesis, and other theories that extend beyond and complement the GOE theory.

Chapter Four will focus on our original work. Our purpose is to test the universality hypothesis using the Lipkin-Meshkov-Glick model [LMG65]. This simple but non-trivial model was introduced to check the approximate techniques of nuclear and many-body physics, and so was designed to mimic the nucleus, or at least the shell model picture of the nucleus. The version we consider consists of three M -fold degenerate single particle levels and M nucleons. The two-body interaction plays the role of the residual interaction of valence nucleons, i.e., the difference between the true nuclear two-body interaction and the mean field. This intrinsically quantum mechanical Hamiltonian, expressed in terms of fermionic creation and annihilation operators, may be written in a compact basis, thus simplifying the quantum calculations as well as providing a unique testing ground for the GOE hypothesis.

To test GOE we first investigate the dynamics of the classical analog. This is obtained from the collective behavior in the $M \rightarrow \infty$ (thermodynamic) limit. The classical Hamiltonian has quartic momentum dependence - it does not describe a particle in a potential well. We find the parameters and energies for which classical chaos exists, and then examine spectral averages of the fluctuations of the corresponding eigenvalues and the distributions of the eigenvectors for agreement with GOE ensemble averages.

Chapter Two

Classical Systems from Regular to Random

Physics is a reductionist endeavor: we focus first on the simplest problems in a field to gain expertise and then move on to more elusive topics. In the past thirty years we have broadened our vision in classical dynamics to include the nonlinear systems as well as integrable systems. In this chapter we will examine the spectrum of classical systems from regular to random and the methods of the dynamicists to quantify chaos present in these systems.

The subject of this section is the set of conservative classical Hamiltonians with N degrees of freedom. Because energy is a constant of the motion, the trajectories don't cover the entire $2N$ phase space, but lie on a $2N - 1$ dimensional energy surface. The ignored variable may always be recovered from energy conservation if the sign is also specified:

$$p_N = \pm \sqrt{2m_N \left(E - \sum_{i=1}^{N-1} \frac{p_i^2}{2m_i} - V(\vec{x}) \right)},$$

where we have assumed canonical momentum dependence. We will also confine our discussion to systems for which the motion is bounded.

2.1 Integrable Systems

A classical system with N degrees of freedom is integrable if there exist N functionally independent constants of the motion, $F(\vec{p}, \vec{q})$. This implies that all conservative systems with one degree of freedom and all conservative separable systems are integrable. For an integrable system we may make a canonical transformation to the action-angle coordinates $(\vec{J}, \vec{\theta})$ so that the new Hamiltonian is a function of the actions alone:

$$H = H(\vec{J}).$$

The time evolution of the variables is obtained from Hamilton's equations:

$$\begin{aligned} \frac{\partial \vec{J}}{\partial t} = -\frac{\partial H}{\partial \vec{\theta}} = 0 & \quad J_i(t) = \text{constant} \\ \frac{\partial \vec{\theta}}{\partial t} = \frac{\partial H}{\partial \vec{J}} \equiv \vec{\omega}(\vec{J}) = \text{constant} & \quad \vec{\theta}(t) = \vec{\omega}(\vec{J})t + \vec{c} \pmod{2\pi}. \end{aligned}$$

The solution for $\vec{J}(t)$ and $\vec{\theta}(t)$ is trivial, although the canonical transformation may not be so easy.

Because there are N constants of the motion, the trajectories all lie on N dimensional submanifolds of phase space. These submanifolds in action-angle space have the topology of a torus. To see this, first consider the $N = 2$ case. In two dimensions, we usually consider a torus as a doughnut, but this conceptualization vigorously resists generalization to higher dimensions. Instead, consider a two-torus as a rectangle with periodic boundary conditions: θ_1 is measured along the horizontal; θ_2 , along the vertical; $\vec{\theta}(t)$ gives a straight line trajectory on the rectangle. When an edge is reached, the trajectory jumps to the parallel edge with the height along that edge preserved. (Figure 2.1) The familiar doughnut is recovered if you imagine each edge physically joined with its parallel (a little stretching will be required). Generalizing to higher dimensions, the N -torus is an N -dimensional hypercube with periodic boundary conditions, and the integrable motions is again a straight line trajectory on such a torus.

Each torus is defined by the value of \vec{J} . Once it is known, the value of $\vec{\omega}$ is fixed, and the motion is completely specified. These are "invariant" tori because a trajectory will remain on this surface for all time, not wandering into other energetically accessible regions.

The constant slope of the trajectory is given by the ratio of ω_2 to ω_1 . These parallel trajectories will never intersect themselves, a feature required of solutions to the deterministic Hamilton's equations. If there exists a vector \vec{m} with integer components ($\vec{m} \neq 0$) such that

$$\vec{m} \cdot \vec{\omega} = 0, \tag{2.1.1}$$

then the trajectory eventually closes on itself, and is one-dimensional. If $\vec{m} = (1, -1)$, it will close after one period of θ_1 and θ_2 ; if $\vec{m} = (2, -1)$, it will close after one period of θ_2 and two periods of θ_1 , and so on. Any torus for which such an \vec{m} can be found is called a rational torus. If there is no such \vec{m} , then the trajectory will densely cover the torus as time goes to infinity, and the torus is called irrational. A semi-rational torus obeys relation 2.1.1, but only for a proper subset of the frequencies.

2.2 Surfaces of Section and Classical Perturbation Theory

When the Hamiltonian is not integrable, and we cannot write $\vec{x}(t)$ in analytic form, we need a new approach. In this section we will look at surfaces of section and classical perturbation theory; both give us a method to see and understand the general nature of the classical flow (i.e., the continuous time evolution). The next two sections are also devoted to a general description of phase space for non-integrable systems; we will return to the classification of Hamiltonian systems in §2.5.

A surface of section is a cross section of phase space filled with trajectories. One variable is singled out as the “trigger”. Whenever this variable is equal to a specified constant, the values of the remaining $2N - 2$ variables are plotted. (Figure 2.2) Several sets of these points, each set from different initial conditions, is a surface of section. When $N = 2$ this procedure makes the three dimensional trajectory two dimensional, which is a distinct advantage. These surfaces of section (also called Poincaré sections) are area preserving (recall Liouville’s Theorem) maps of the plane onto itself. Recalling from the last section that integrable systems lie on tori, the presence of toroidal cross sections in the sections would be a sign of integrability. (We must now think in terms of the previously maligned doughnut-tori. The rectangle-tori are discontinuous and cannot exist in physical phase space.) As an historical example, integrals of motion for the Toda lattice were vigorously

sought and consequently found when surfaces of section displayed nothing but tori for all initial conditions. (Figure 2.3)

The necessary presence of toroidal cross sections, i.e. closed curves, for an integrable system can be made clear in another way. For $N = 2$, if we have two conserved quantities E and L we may write

$$E = E(x_1, x_2, p_1, p_2) \quad L = L(x_1, x_2, p_1, p_2),$$

which can be inverted to give

$$p_1 = F_1(E, x_1, x_2, p_2) \quad p_2 = F_2(E, L, x_1, x_2).$$

On the surface of section defined by $x_1 = \text{constant}$, p_2 becomes an analytic function of x_2 alone; we see this as a closed curve.

Chaos, on the other hand, is seen in a surface of section as a sea of dots with no apparent structure. This is because the tori have disappeared. The Henon-Heiles potential [HH64],

$$V(x, y) = \frac{1}{2}(x^2 + y^2) + x^2y - \frac{1}{3}y^3, \quad (2.2.1)$$

gives rise to a rich variety of surfaces of section. (Figure 2.4, right column) As the energy increases from 0 to $\frac{1}{6}$ (where the motion becomes unbounded) the sections change in character. At first the sections are filled with tori, then small chaotic regions appear, and finally the whole surface is filled with chaotic dots.

Surfaces of section can never prove integrability or chaos, but they do provide a clear and immediate picture of phase space trajectories.

Classical perturbation methods, on the other hand, can provide a rigorous proof of integrability or chaos, but are much less accessible [LL83]. The strategy is to transform any Hamiltonian into action-angle form, order by order in the perturbation. We begin with a Hamiltonian of the form

$$H(\vec{J}, \vec{\theta}) = H_0(\vec{J}) + \epsilon H_1(\vec{J}, \vec{\theta}),$$

where H_0 is integrable, ϵ measures the deviation from integrability, and H_1 is a multiply periodic function of the angles:

$$H_1 = \sum_{\vec{m}} H_{1\vec{m}}(\vec{J}) e^{i\vec{m}\cdot\vec{\theta}} .$$

We may attempt to find new variables $\vec{I}, \vec{\phi}$ such that $H_0 + \epsilon H_1$ is independent of $\vec{\phi}$. Using the generating function

$$S = \vec{I} \cdot \vec{\theta} + \epsilon S_1(\vec{I}, \vec{\theta}) + \dots .$$

we find relations between the old and new variables:

$$\begin{aligned} \vec{\phi} &= \frac{\partial S}{\partial \vec{I}} = \vec{\theta} + \epsilon \frac{\partial S_1}{\partial \vec{I}} + \dots \\ \vec{J} &= \frac{\partial S}{\partial \vec{\theta}} = \vec{I} + \epsilon \frac{\partial S_1}{\partial \vec{\theta}} + \dots . \end{aligned}$$

We may write the new Hamiltonian K according to the rules of canonical transformations

$$\begin{aligned} K(\vec{I}, \vec{\phi}) &= H(\vec{J}, \vec{\theta}) + \frac{\partial S}{\partial t} \\ &= H(\vec{J}(\vec{I}, \vec{\phi}), \vec{\theta}(\vec{I}, \vec{\phi})) . \end{aligned}$$

But we may also write the new Hamiltonian as a power series in ϵ

$$K(\vec{I}, \vec{\phi}) = K_0 + \epsilon K_1 + \epsilon^2 K_2 + \dots .$$

Matching powers of ϵ we find

$$K_0(\vec{I}, \vec{\phi}) = H_0(\vec{I}) ,$$

and

$$\begin{aligned} K_1(\vec{I}, \vec{\phi}) &= \frac{\partial H_0}{\partial \vec{I}} \cdot \frac{\partial S_1(\vec{I}, \vec{\phi})}{\partial \vec{\phi}} + H_1(\vec{I}, \vec{\phi}) \\ &= \vec{\omega}(\vec{I}) \cdot \frac{\partial S_1(\vec{I}, \vec{\phi})}{\partial \vec{\phi}} + H_1(\vec{I}, \vec{\phi}) . \end{aligned}$$

K_0 is already in action-angle form, and we will choose S_1 so that K_1 is also in that form. We write

$$H_1(\vec{I}, \vec{\phi}) = \langle H_1(\vec{I}, \vec{\phi}) \rangle + \{H_1(\vec{I}, \vec{\phi})\},$$

where $\langle \rangle$ indicates the average over all angular variables, and $\{ \}$ indicates the angular dependent part. We delete the $\vec{\phi}$ dependence in K_1 by demanding that

$$\vec{\omega}(\vec{I}) \cdot \frac{\partial S_1}{\partial \vec{\phi}} = -\{H_1(\vec{I}, \vec{\phi})\}.$$

Fourier expanding S_1 and H_1 we find

$$\vec{\omega} \cdot \frac{\partial S_1}{\partial \vec{\phi}} = \sum_{\vec{m}} i\vec{m} \cdot \vec{\omega} S_{1\vec{m}} e^{i\vec{m} \cdot \vec{\phi}} = \sum_{\vec{m}} H_{1\vec{m}} e^{i\vec{m} \cdot \vec{\phi}}.$$

Matching coefficients for each Fourier component we obtain

$$S_{1\vec{m}}(\vec{I}) = i \frac{H_{1\vec{m}}(\vec{I})}{\vec{m} \cdot \vec{\omega}(\vec{I})}. \quad (2.2.2)$$

We have thus defined to first order in ϵ our new variables $\vec{I}, \vec{\phi}$. We could continue in this manner to arbitrary order in ϵ , but the calculations become increasingly difficult increasingly rapidly.

But we must be careful. The series does not converge in the neighborhood of a rational torus where the denominator in 2.2.2 vanishes. This lack of convergence may indicate that we are using an incorrect series expansion, or that the series does not converge. Lack of convergence implies that the Hamiltonian is non-integrable, while a series that is everywhere convergent gives integrability.

Finding all the terms in an infinite series is not a practical exercise. Usually these calculations are carried out only to first or second order. What perturbation theory can give is a reasonable guess for the integrals of the motion. The new actions \vec{I} are the conserved quantities, and plotting $\vec{I}(\vec{J}, \vec{\theta}) = \text{constant}$ in $\vec{J}, \vec{\theta}$ phase space gives an approximation to the true invariant tori. Near rational tori this method is very inaccurate, but in some regions of phase space it yields good results. The

meaning of “near” depends on the size of ϵ . This is illustrated by the figures for the Henon-Heiles potential. (Figure 2.4) The four sets of pictures are for four different energies; ϵ in this system is measured by the energy. The left hand pictures were generated by second order perturbation theory, the right are surfaces of section obtained from numerical integration. The agreement between the two columns gets worse as the perturbation (energy) increases.

2.3 KAM and Poincaré-Birkhoff Theorems

We have seen that invariant tori are the dominant feature of integrable phase space. The changes in phase space arising from perturbations in the Hamiltonian are described by two theorems: Kolmogorov-Arnold-Moser (KAM) theorem proves the fate of irrational tori, and the Poincaré-Birkhoff theorem describes the changes in rational tori. These two classes must be separated because of the problem of small or vanishing denominators mentioned in the last section.

The importance of the KAM theorem cannot be understated. Canonical perturbation methods are usually unsatisfactory because of the presence of small denominators; although they may not affect the motion on short time scales, on long time scales they may alter the character of the motion completely. KAM avoids the problem of small denominators, and provides analytical (infinite time) results concerning nonintegrable Hamiltonian systems. KAM states that for small perturbations of an integrable Hamiltonian, most of the invariant tori persist, although their shape will be distorted. Therefore the general structure of phase space remains unchanged even though the system is no longer integrable.

The proof of KAM requires [Ar78] finding a region in action space, and therefore a $\vec{\omega}(\vec{J})$, so that not only are the tori of the unperturbed system irrational, but they are also sufficiently far from resonance so that

$$|\vec{\omega} \cdot \vec{m}| \geq C|\vec{m}|^{-\nu}$$

for all integer vectors $\vec{m} \neq 0$, and for some C, ν . Next we look for a nearby invariant torus of the *perturbed* system with the same frequencies. Successful searching requires that

$$\det \frac{\partial^2 H}{\partial J^2} = \det \frac{\partial \omega}{\partial J} \neq 0$$

so that the ω 's can be used as a local coordinate system. The final requirement is that $H_0 + \epsilon H_1$ be sufficiently smooth. The searching is done in a convergent iterative fashion similar to Newton's method of tangents. The small divisor problem is never encountered because the frequencies are required to remain far from degeneracy.

The existence of these (distorted) KAM tori has important implications for motion in a system with two degrees of freedom. Because the tori are two dimensional and reside in a three dimensional space, they partition that space. A trajectory lying between two KAM tori, even if it does not lie on a torus itself, is nevertheless greatly restricted in its motion in phase space. This argument does not hold in higher dimensions since an N -dimensional torus will not partition $2N - 1$ -dimensional space for $N > 2$. Therefore, in higher dimensions, a trajectory can wander over the entire energy surface even if KAM tori exist. This is known as Arnold diffusion, and takes place on very long time scales [LL83].

Now that we know the fate of irrational tori under small perturbations, we turn to the rational tori. These tori have zero measure in phase space, just as the rationals occupy zero measure on the number line, but they generate the chaotic behavior.

Why might we expect such novel behavior near rational tori? Let $r\omega_1 + s\omega_2 = 0$ on the rational torus. Then we define

$$\text{winding number} \equiv \alpha \equiv \frac{r}{s}.$$

Note that α will be irrational for an irrational torus. If we look at the surface of section in the J_1, θ_1 plane, and trigger on every s 'th crossing, every point on the rational torus is a fixed point, i.e., a point that is invariant under the mapping. This

is an unusual situation: we don't have simple isolated fixed points, but a continuous curve of fixed points. Therefore, it should not be surprising to discover that this topology doesn't persist after the perturbation. Instead, we find that the curve of fixed points breaks up into a finite number of alternating elliptic and hyperbolic points (stable and unstable fixed points).

This change in topology is proved by the Poincaré-Birkhoff theorem, which we will motivate by looking at the surface of section. The two dimensional surface of section for an integrable system is equivalent to a twist mapping (Figure 2.5)

$$\begin{aligned}\theta_n &= \theta_{n-1} + 2\pi\alpha(J_{n-1}) \\ J_n &= J_{n-1},\end{aligned}\tag{2.3.1}$$

where the subscript now indicates the iterate of the two dimensional map, and α is the winding number defined above. The twist mapping keeps the radial variable (the action in this case) constant, but twists or rotates the angle by an amount that may depend on the action. The surface of section for a nonintegrable system is a perturbed twist mapping, for which both the radial and angular variables change.

For reasonable Hamiltonians, α is a continuous function of the actions. Denoting the value on resonance by α_0 , for smaller J 's we have $\alpha_1 < \alpha_0$, for larger J 's we have $\alpha_2 > \alpha_0$, or vice versa. Looking at the s 'th iterate of the map in the unperturbed system, the points on rational torus are stationary; those above resonance move counterclockwise; those below resonance, clockwise. Adding the perturbation does not change the winding numbers significantly, and we still expect this progression of clockwise, to stationary, to counterclockwise as J changes, even though the stationary points shouldn't be expected to occur at exactly the same values of the action as for the unperturbed system.

Therefore, there exists some curve for which the angular variable is stationary under the s 'th iterate of the perturbed map, although the radial variable will change. Consider the two curves made up of the s 'th and $2s$ 'th iterates of this angular-stationary curve. (Figure 2.6) Because the surface of section is an area preserving

mapping, these curves must intersect each other. And because the curves are closed, they must intersect in an even number of points. These points are then completely stationary, and it has been shown that they are alternately hyperbolic and elliptic fixed points [LL83].

The structure of phase space is becoming clearer (Figure 2.7). It is filled with KAM tori, and between the tori where rational tori used to be, we have a ring of stable and unstable fixed points. What happens about these fixed points?

Using secular perturbation theory, we investigate phase space near the elliptic points. In a small neighborhood about the fixed point, the Hamiltonian has the form of a one-dimensional pendulum to first order in ϵ [LL83]. But such a system is integrable, so there are invariant tori about the elliptic point. However, if we include the higher order terms as a perturbation, we find that the system is not integrable, and therefore can invoke the KAM and Poincaré-Birkhoff theorems in this small region of phase space, and so we again expect to see KAM tori (now called second order islands) and the alternating stable and unstable fixed points. This scenario is repeated *ad infinitum* (though the higher order islands are proportionately smaller and smaller) showing that detail exists on every scale. (Figure 2.8)

The chaotic behavior appears when we look at the unstable (hyperbolic) fixed points and their stable and unstable separatrices. The stable and unstable directions are given by the eigenvectors of the linearized equations of motion evaluated at the hyperbolic point and projected onto the surface of section. A stable (unstable) separatrix on a surface of section is operationally defined as the backward (forward) iteration of the small line segment emanating from the hyperbolic point and in the direction of stability (instability); it is therefore not just a single trajectory. The stable and unstable separatrices do not coincide for non-integrable systems [He80], however, they may intersect in “homoclinic” points. Consider a trajectory which includes one homoclinic point. By the definition of a separatrix, the mapping of this point is also a homoclinic point. Therefore the entire trajectory is made up of

homoclinic points, and although the stable and unstable trajectories don't coincide, they intersect in an infinite number of points.

Consider the area enclosed by the two separatrices and bounded by two homoclinic points. (Figure 2.9) This will map into another area of the same size, but the base between the homoclinic points will be smaller since they are approaching the hyperbolic point as e^{-t} . To compensate, the other sides must become exponentially longer. Somehow these long separatrices fold themselves in the area of phase space given to them between the KAM tori. This generates chaotic behavior. The long time behavior of a trajectory will depend on where it lies among the folds and pleats of the separatrices. Two points which are initially close together may actually be separated by many layers of folds, and therefore their long time trajectories must be quite different.

2.4 Lyapunov Exponents and Entropy

In the last section, we began to see the onset of chaos with the wild behavior of intersecting separatrices. In this section we become more quantitative about the “instability with respect to initial conditions” known as chaos. The calculable, useful quantities are the Lyapunov exponents which measure the stability of a single orbit, and the entropy which measures the rate of information gain for the entire system.

The subject of this section are the trajectories $\vec{x}(\vec{x}_0, t)$ which depend on initial conditions \vec{x}_0 and on time t . (In this section \vec{x} stands for all $2N$ phase space coordinates.) These trajectories evolve in time according to Hamilton's equations

$$\dot{\vec{x}} = \vec{F}(\vec{x}) .$$

Now we define $\vec{\xi}$ as the vector between two trajectories initially separated by $\vec{\delta}$

$$\vec{\xi}(\vec{x}_0, t, \vec{\delta}) \equiv \frac{\vec{x}(\vec{x}_0 + \vec{\delta}, t) - \vec{x}(\vec{x}_0, t)}{|\vec{\delta}|} .$$

To find the equations of motion for $\vec{\xi}$, we Taylor expand the equations of motion for $\vec{x}(\vec{x}_0 + \vec{\delta}, t)$ about $\vec{x}(\vec{x}_0, t)$. As long as $|\vec{\delta}|$ is small, we need only retain terms to first order in $|\vec{\delta}|$:

$$\dot{\vec{\xi}}(\vec{x}_0, t) \simeq \mathbf{D}^F \vec{\xi}(\vec{x}_0, t),$$

where

$$D_{ij}^F \equiv \left. \frac{\partial F_i}{\partial x_j} \right|_{\vec{x}(\vec{x}_0, t)}.$$

These are the usual linear equations of motion for small separations.

The evolution of $\vec{\xi}(t)$ gives the linear stability of the trajectory $\vec{x}(t)$. To see this, consider the case when \mathbf{D}^F is constant. Let its eigenvalues and eigenvectors be $\lambda_1 \geq \lambda_2 \geq \dots \geq \lambda_{2N}$ and $\hat{\zeta}_1, \hat{\zeta}_2, \dots, \hat{\zeta}_{2N}$. Each eigenvector has exponential time dependence

$$\vec{\zeta}_i(t) = e^{\lambda_i t} \vec{\zeta}_i(0).$$

If $\lambda_i > 0$, then the motion is unstable in the $\hat{\zeta}_i$ direction; small perturbations grow with time. While if $\lambda_i < 0$, the motion is stable in that direction, and the linear approximation remains good for all time. In general, we begin with a vector which is a linear combination of the eigenvectors,

$$\vec{\xi}(t=0) = \sum_{\mathbf{i}}^N c_{\mathbf{i}} \hat{\zeta}_{\mathbf{i}},$$

with $\sum_{\mathbf{i}=1}^N c_{\mathbf{i}}^2 = 1$. In this case the evolution is given by

$$\vec{\xi}(t) = \sum_{\mathbf{i}}^N c_{\mathbf{i}} e^{\lambda_{\mathbf{i}} t} \hat{\zeta}_{\mathbf{i}}.$$

We define the Lyapunov exponent:

$$\lambda(\vec{x}_0, \vec{\delta}) \equiv \lim_{t \rightarrow \infty} \frac{1}{t} \log \frac{|\vec{\xi}(\vec{x}_0, t, \vec{\delta})|}{|\vec{\xi}(\vec{x}_0, 0, \vec{\delta})|}.$$

If $\vec{\delta} \parallel \hat{\zeta}_i$ then $\lambda = \lambda_i$, otherwise

$$\begin{aligned}\lambda &= \lim_{t \rightarrow \infty} \frac{1}{t} \log \left| \sum (c_i e^{\lambda_i t}) \right| \\ &= \lim_{t \rightarrow \infty} \frac{1}{t} \log |(c_{\max} e^{\lambda_{\max} t})| \\ &= \lambda_{\max},\end{aligned}$$

where λ_{\max} is the largest eigenvalue for which $c_i \neq 0$. In general $c_1 \neq 0$, therefore if the motion is unstable in any direction, the Lyapunov exponent will be positive, while if the motion is stable in all directions, it will be zero or negative.

Now we turn to the general case where D^F is not constant [SN79, Wo85]. Because we have no eigenvalues in this case, the notions are not so clear, nor the proofs so easy, yet the general ideas persist. First, we define a vector in tangent space

$$\vec{\eta}(\vec{x}_0, t, \hat{\delta}) \equiv \lim_{|\vec{\delta}| \rightarrow 0} \vec{\xi}(\vec{x}_0, t, \vec{\delta}).$$

Now the equations of motion are exact because the initial separation is zero:

$$\dot{\vec{\eta}}(\vec{x}_0, t, \hat{\delta}) = D^F \vec{\eta}(\vec{x}_0, t, \hat{\delta}). \quad (2.4.1)$$

We may consider the D^F as constant at each point in phase space and varying continuously from point to point. Therefore the eigenvalues and eigenvectors change in size and direction from point to point. The analogously defined Lyapunov exponent,

$$\lambda(\vec{x}_0, \hat{\delta}) = \lim_{t \rightarrow \infty} \frac{1}{t} \ln \frac{|\vec{\eta}(\vec{x}_0, t, \hat{\delta})|}{|\vec{\eta}(\vec{x}_0, 0, \hat{\delta})|}, \quad (2.4.2)$$

gives, in some loose sense, the infinite time average of the local Lyapunov exponent; telling us if, on the average, the trajectory is stable or unstable. Again, if we choose $\hat{\delta}$ at random, we will pick out the largest Lyapunov exponent (therefore the dependence on $\hat{\delta}$ is usually suppressed). However, if we force $\vec{\eta}(t)$ always to be perpendicular to the fastest growing direction, we will pick out the second largest exponent, and so on.

There are many rigorous proofs concerning the Lyapunov exponents [Os68, ER85, Pe77]; we will simply quote the results here without attempting any proofs. Oseledec showed [Os68] that the limit given in 2.4.2 does exist for a compact phase space, and is independent of metric. He also showed that there exists a spectrum of Lyapunov exponents. The $2N$ exponents defined above, corresponding to the $2N$ dimensions, are first order Lyapunov exponents. A p th order Lyapunov exponent gives the exponential rate of growth or decay of a p -dimensional volume in phase space. This is equal to the sum of the p distinct first order exponents. For a Hamiltonian system, the sum of all $2N$ Lyapunov exponents must be zero because phase space neither expands nor contracts. For dissipative systems the sum is negative.

From simple considerations we may learn more about these exponents for Hamiltonian systems. The Lyapunov spectrum for the time-reversed system is just minus the original spectrum [ER85]. But Hamiltonian systems are time-reversal invariant, therefore, $\lambda_i = \lambda_{2N-i}$. Moreover, as long as we avoid fixed points, the exponent along the direction of motion is zero [ER85]. By the above argument, if one exponent is zero, two must be zero. The second zero exponent is associated with the direction perpendicular to the energy surface, because we are restricting ourselves to motion on the surface. Combining all these facts, we see that the Lyapunov spectrum for a two dimensional Hamiltonian system is given by $(\lambda_0, 0, 0, -\lambda_0)$.

The existence of positive exponents is often loosely associated with “exponential divergence of trajectories”, a sadly misleading phrase. Positive exponents indicate only that small perturbations do not remain small; first order perturbation theory is no longer applicable. We can make no more predictions about the separation of close trajectories using 2.4.1. The claim of exponential divergence is clearly incorrect if the motion is bounded; the separation must always be finite. However, it is correct to associate first order stability or instability of an orbit with negative or positive characteristic exponents.

From the Lyapunov spectrum, which characterizes a single orbit, we may calculate the entropy which characterizes the entire system. This entropy is not the fa-

miliar thermodynamic entropy, but information entropy which measures the average rate of information change in a flow. The amount of information in a measurement is defined [Sh81]

$$\text{information} \equiv - \sum_{i=1}^N p_i \log p_i , \quad (2.4.3)$$

where there are N possible outcomes of the measurement, each with probability p_i .

Why is this a reasonable definition? Consider a measurement that has two possible outcomes, one with probability one, the other with probability zero; the information of the system is zero (with the convention that $0 \log 0 = 0$). We learn nothing from the measurement; there is no surprise in the outcome. Alternatively, if there are two possibilities, each with probability $\frac{1}{2}$, the information is maximum for this partition. We are most unsure of the outcome; we are “maximally” surprised by the results of measurement. If we increase the number of possibilities to m , the information is maximum if all $p_i = 1/m$, i.e., we are completely unbiased before the measurement. In this case we may write

$$\text{information} = - \sum_{i=1}^m \frac{1}{m} \log \frac{1}{m} = \log m ;$$

the information increases as $\log m$. The finer our measurements, the greater information is given by each measurement. These are all intuitively reasonable features of something we call information.

But information may change because of the flow. Consider a contracting flow. If the original space was covered by m boxes of a given size, after some time, the contracted space will be covered by n boxes, with $m > n$. The boxes are the same size since the measuring instrument is the same. Using the formula above, the change in information is

$$\text{change in information} = \log m - \log n = \log \frac{m}{n} < 0 ,$$

and information has been lost.

This terminology may be confusing: gain and loss always depend upon your perspective. For information, loss and gain are judged by experimentalists who have measuring devices of finite precision. They know the initial conditions to only a certain accuracy; if the flow is contracting, future measurements give them no more information about those initial conditions. Theorists, on the other hand, prefer contracting flows, since the finite precision of the initial conditions does not affect their predictive powers as $t \rightarrow \infty$.

Experimentalists gain information from expanding flows. Take as an example the left shift map given in the introduction. The map takes an interval Δx into an interval of $2\Delta x$. After each iteration, the points that used to be in one box are now in two. The change in information is $\log 2$, and information is gained. Therefore, the experimentalists who make repeated measurements of the iterates of one point will learn with greater and greater precision the initial conditions of that point. However, the theorists will not find this a happy situation. If they know which box a certain point was in at $n = 1$, they will not know which of two boxes it was in at $n = 2$, and its long time trajectory will be completely unknown.

It is the stretching in the left shift map that is responsible for information gain. Similarly, in Hamiltonian flows, if there is a positive exponent, indicating stretching in at least one direction, there is information gain. Consider a set of points covering the experimental box at $t = 0$ as an incompressible fluid. If the flow stretches in one direction, this fluid will evolve into a long tube. Although the fluid covers the same volume as it did originally, it covers many more boxes; hence the measurements will tell us something. On the other hand, if all the exponents are zero, the fluid retains its general shape as well as volume, and will cover approximately the same number of boxes as time goes by. (Figure 2.10)

Before we define entropy, we must first define a partition of the $(2N - 1)$ -dimensional energy surface. Such a partition is specified by a set of $L \geq 2$ non-overlapping surfaces which completely cover the energy surface. Let

$$\mathcal{A}(0) \equiv (\mathcal{A}_1(0), \mathcal{A}_2(0), \dots, \mathcal{A}_L(0))$$

be the set of surfaces (i.e., the partition) at $t = 0$. Now evolve $\mathcal{A}(0)$ backwards for one unit of time to obtain a new partition given by

$$\mathcal{A}(-1) \equiv (\mathcal{A}_1(-1), \mathcal{A}_2(-1), \dots, \mathcal{A}_L(-1)),$$

and so on to obtain $\mathcal{A}(-n)$. Then we define the partition $\mathcal{B}(-n)$ as the set of surfaces defined by the intersection of surfaces at all previous times:

$$\mathcal{B}_l(-n) \equiv \mathcal{A}_i(0) \cap \mathcal{A}_j(-1) \cap \dots \cap \mathcal{A}_k(-n).$$

Therefore the number of surfaces defined by $\mathcal{B}(-n)$ cannot decrease with increasing n .

Entropy is defined as the change in information for one time unit, as time goes to infinity [ER85]:

$$\text{entropy} \equiv h(\mathcal{A}_i(0), \mu, \mathbf{D}^F) \equiv \lim_{n \rightarrow \infty} (I_n - I_{n-1}), \quad (2.4.4)$$

where

$$I_n \equiv - \sum_{\text{surfaces}} \mu(\mathcal{B}_i(-n)) \log \mu(\mathcal{B}_i(-n)),$$

and μ gives the measure of each surface. The entropy clearly depends on the original partition. If at $t = -n$ there are more surfaces in the partition $\mathcal{B}(t)$ than at $t = -n + 1$, we have gained information. If this gain persists to infinite n , this implies positive entropy. Yet for periodic motion, after some finite n , the number of surfaces will no longer increase, and the entropy will be zero. Positive entropy indicates that no finite number of measurements will allow you to predict the next measurement. Note that, unlike the thermodynamic entropy which depends on the state of the system, the information entropy is an intrinsic property of the flow or map.

Positive entropy is related to stretching, as discussed above; therefore, it should not be surprising to find that the entropy is related to the Lyapunov exponents. For a Hamiltonian flows Pesin proved [Pe77]

$$h_{KS}(\mu, \mathbf{D}^F) = \int_{\Sigma(E)} \sum_{\lambda_i > 0} \lambda_i(\vec{x}) d\mu(\vec{x}), \quad (2.4.5)$$

where $\Sigma(E)$ is the energy surface. For a system with two degrees of freedom, the sum over positive exponents has only one term. This entropy is actually the Kolmogorov-Sinai entropy which is the maximum information entropy over all the possible finite partitions $\mathcal{A}(0)$.

In summary, positive Lyapunov exponents imply stretching of the Hamiltonian fluid, which cause information gain and instability with respect to initial conditions. In this strict sense positive Lyapunov exponents imply chaotic motion.

2.5 Degrees of Irregularity

We began in §2.1 discussing the spectrum of classical behavior by introducing integrable and quasi-integrable Hamiltonian flows. Now that we understand the general features of phase space, and the notions of chaos, we can complete the cataloging of Hamiltonian systems. In order of increasing irregularity these are ergodic, mixing, K systems, and B systems.

We begin with the ergodic systems for which almost every trajectory comes arbitrarily close to almost every point in phase space. The phrase “almost every” has a precise meaning. Those points not included in “almost every” have no measure in phase space. This qualification is necessary because even in the most chaotic systems there are trajectories with finite period which do not explore all of phase space. In the shift map, for example, $x = .\overline{100}$ (one half) is a periodic point.

An example of an ergodic mapping is the twist mapping mentioned in §2.3

$$\theta_n = \theta_{n-1} + 2\pi \alpha$$

$$J_n = J_{n-1}$$

if α is irrational. As time goes to infinity, the points of the mapping will densely cover the circle of radius J_n making the time average equal to an average over the circle.

But we said previously that this twist map is equivalent to the surface of section for an integrable system. Are we claiming now that it is irregular because it is

ergodic? No. Every mapping or flow is ergodic on some manifold. The trajectories of rational tori are ergodic on a line, the trajectories of an irrational torus are ergodic on the torus, there may be ergodic trajectories in the region between KAM tori. The important calculation determines the manifold on which the motion is ergodic. If a Hamiltonian system is ergodic on the energy surface, then the flow is maximally ergodic. From now on the term ergodic will be used in this strong sense. Because KAM tori partition phase space for $N = 2$, the phase space of a 2-dimensional ergodic flow must be KAMless.

It is important to note the effect of ergodicity on $\lambda(\vec{x}_0)$. Lyapunov exponents are time averages of the growth rate of the vectors in tangent space. For an ergodic flow, time averages equal space averages; space averages are independent of initial conditions; therefore, the Lyapunov exponents of ergodic flows are independent of initial conditions.

The next stage in complexity is reached by the mixing systems. Mixing requires that any finite element of Hamiltonian fluid on the energy surface be spread evenly over the entire surface as $t \rightarrow \infty$. This is entirely analogous to the coarse-grained mixing of coffee and cream: in any small but finite bit of the fluid we find the same proportions of coffee and cream as we find in the entire cup. This spreading over phase space is caused by the stretching discussed in the last chapter. However, it is now important to note that a positive Lyapunov exponent indicates an exponential growth rate. For mixing the stretching need only be linear in time; mixing systems aren't necessarily chaotic.

K systems are defined as systems with positive entropy for any finite partition $\mathcal{A}(0)$ (2.4.4); they are chaotic. Note that this is stronger than having positive Kolmogorov-Sinai entropy (2.4.5), since h_{KS} is the *maximum* value for all partitions.

B systems are even more chaotic: the flow in a B system is as unpredictable as possible, in the sense that consecutive measurements are uncorrelated. As an

example, consider once again the left shift map and this experiment. Choose an initial point at random and look at the iterates of that point. Those iterates will jump between the boxes $[0, \frac{1}{2})$ and $[\frac{1}{2}, 1)$, landing in each an equal number of times on average. Thus the map is as random as a coin toss, as random as possible.

These classifications of Hamiltonian flows form a hierarchy

integrable	N constants of the motion
quasi integrable	$1 < m < N$ constants of the motion
nonintegrable	only energy is conserved
ergodic	time averages = space averages
mixing	uniform spreading as $t \rightarrow \infty$
K system	instability with respect to initial conditions
B system	random as a coin toss.

B system implies K, which implies mixing, which implies ergodic, but the converses are not true. For example, the ergodic twist map given above is not mixing since any arc of the circle remains unstretched for all time. This classification is more formal than practical: it is a monumental task to prove that any given system has any of these properties.

In §5.3 we quantify the degree of chaos in the classical limit of the three level Lipkin-Meshkov-Glick model. We would like to show that, at some value of the coupling parameter and energy, it is a K-system. We will have to be satisfied with numerical evidence of ergodicity and chaos which together add up to a K-system. Ergodicity is necessary; otherwise, there are partitions of phase space, \mathcal{A} , that are invariant under backwards time evolution (e.g., for $N = 2$, a partition whose surfaces are bordered by KAM tori) and give zero entropy (2.4.4). If the unique Lyapunov exponent of an ergodic system is positive, this indicates that the system is mixing at an exponential rate, and is therefore chaotic.

There are implications in this classification scheme for classical thermodynamics. Thermodynamic equilibrium requires mixing, but we have seen that there is a wide

gap between integrable systems and mixing systems. The systems that fall between are those of interest to nonlinear dynamicists.

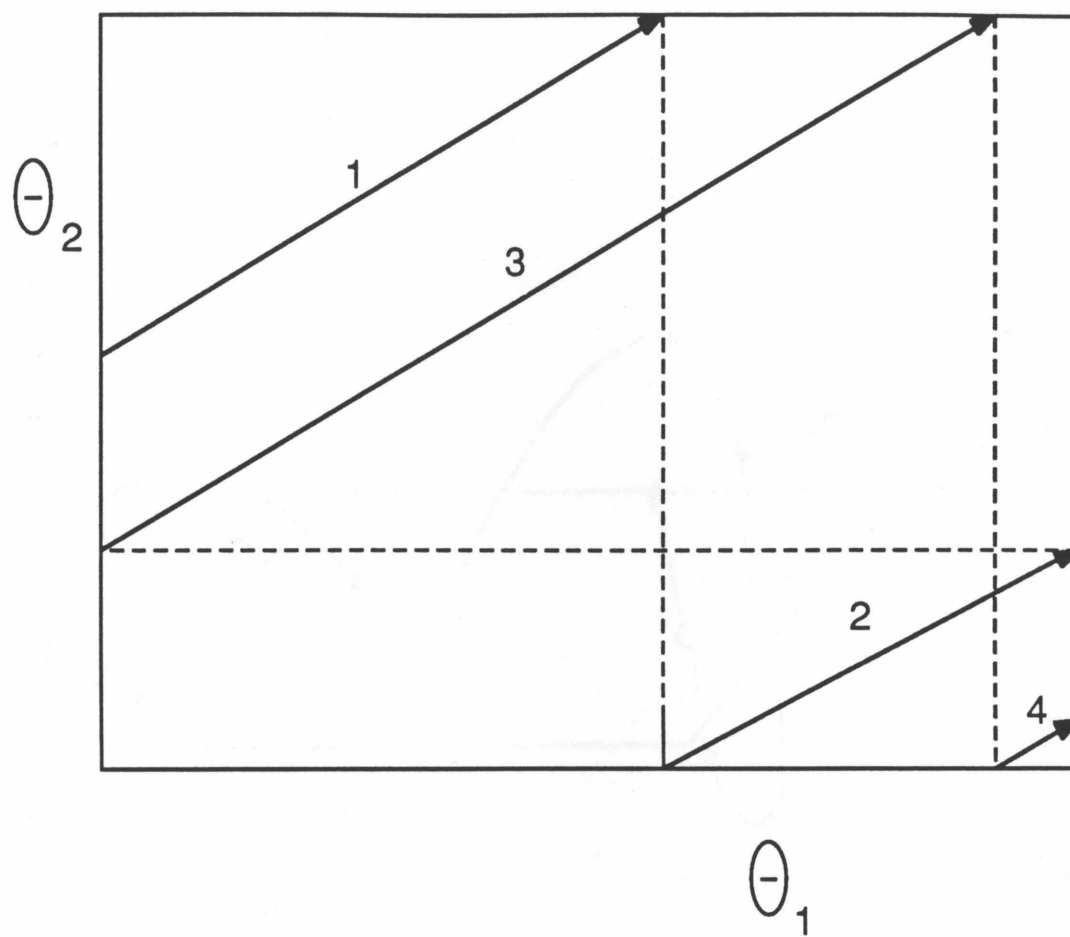


Figure 2.1 The solid line shows a trajectory on a two-dimensional torus, the dashed lines indicate the periodicity of the boundary conditions; numbers indicate the order of the crossings. Because the trajectory has a constant slope, it can never intersect itself.

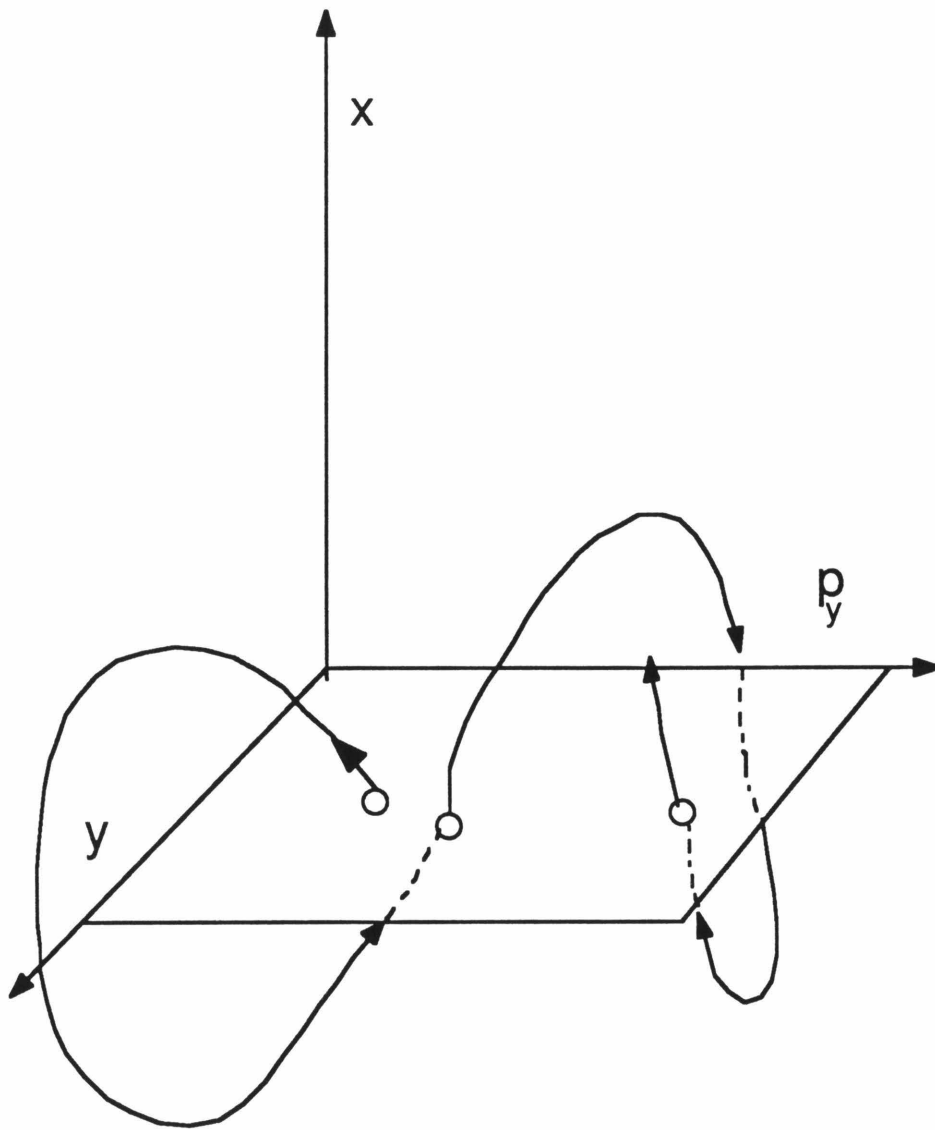


Figure 2.2 The surface of section is the set of points (y, p_y) whenever $x = x_0$ and $p_x > 0$. Pictorially, these are the upward piercings of the plane $x = x_0$ by a trajectory, indicated by the open circles.

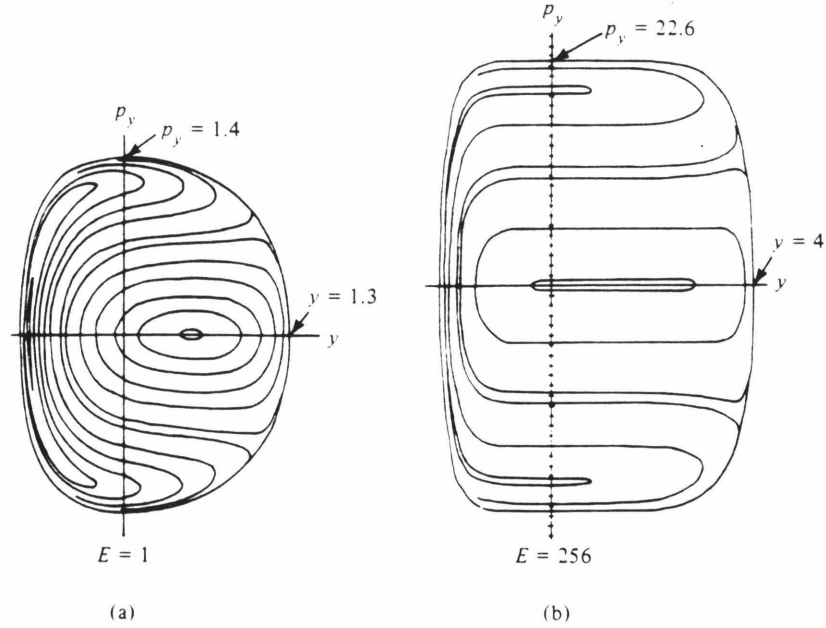


Figure 2.3 Surfaces of section for the Toda Lattice,

$$H = \frac{1}{2}(p_x^2 + p_y^2) + \frac{1}{24} \left[\exp(2y + 2\sqrt{3}x) + \exp(2y - 2\sqrt{3}x) + \exp(-4y) \right] - \frac{1}{8},$$

which is not obviously integrable. However, the surfaces show closed curves (i.e., tori) at any energy ((a) $E = 1$ and (b) $E = 256$). This numerical evidence of integrability prompted a search for another isolating integral of the motion. This integral calculated by Henon [He74] is written

$$I = 8p_x(p_x^2 - 3p_y^2) + (p_x + \sqrt{3}p_y) \exp(2y - 2\sqrt{3}x) - 2p_x \exp(-4y) + (p_x - \sqrt{3}p_y) \exp(2y + 2\sqrt{3}x) = \text{constant}$$

The numerical work and graphs are due to Ford [Fo73].

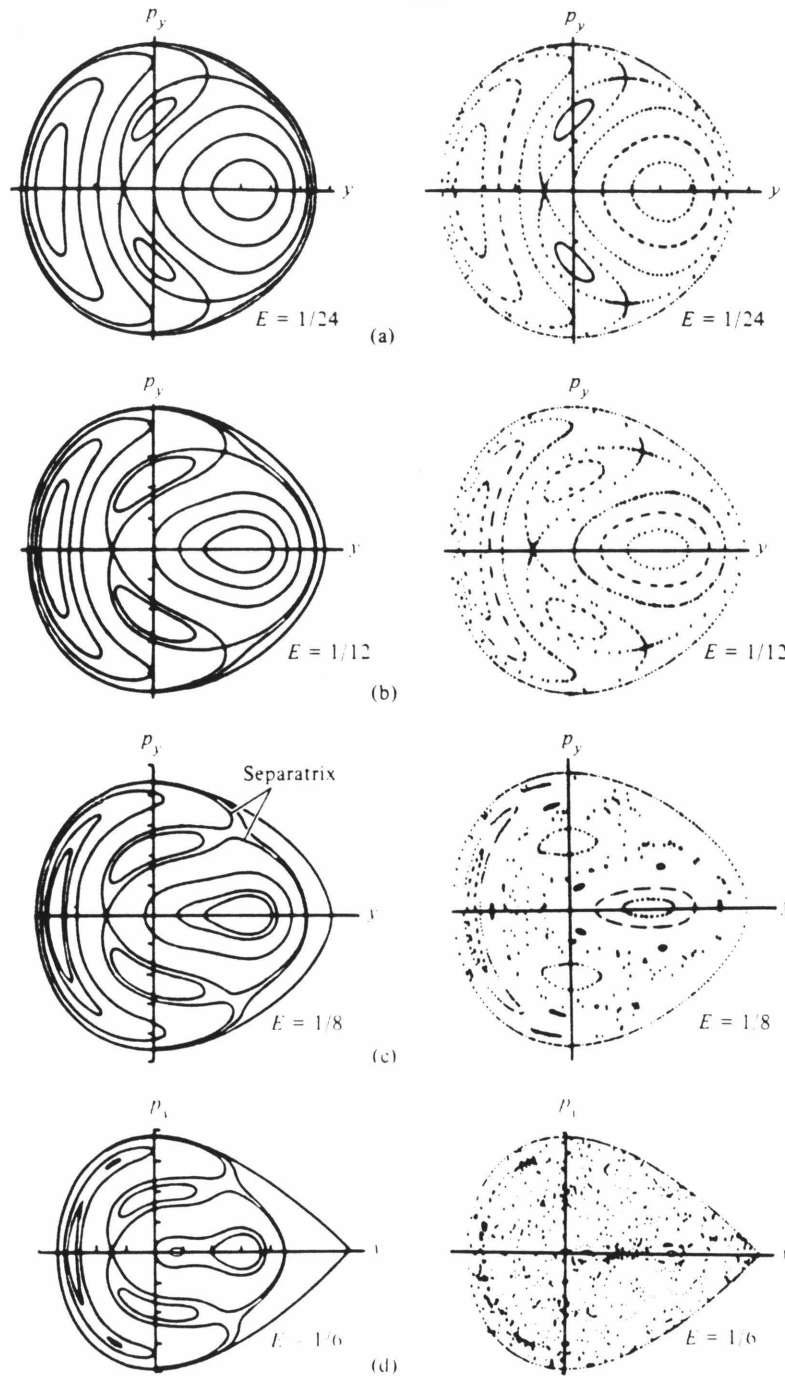


Figure 2.4 The surfaces of section for the Henon Heiles potential (2.2.1) at four different energies, calculated from perturbation theory (left column) and from numerical integration of the trajectories (right column). As the energy increases the chaotic regions become larger, and perturbation theory calculations become less accurate. [Gu66]

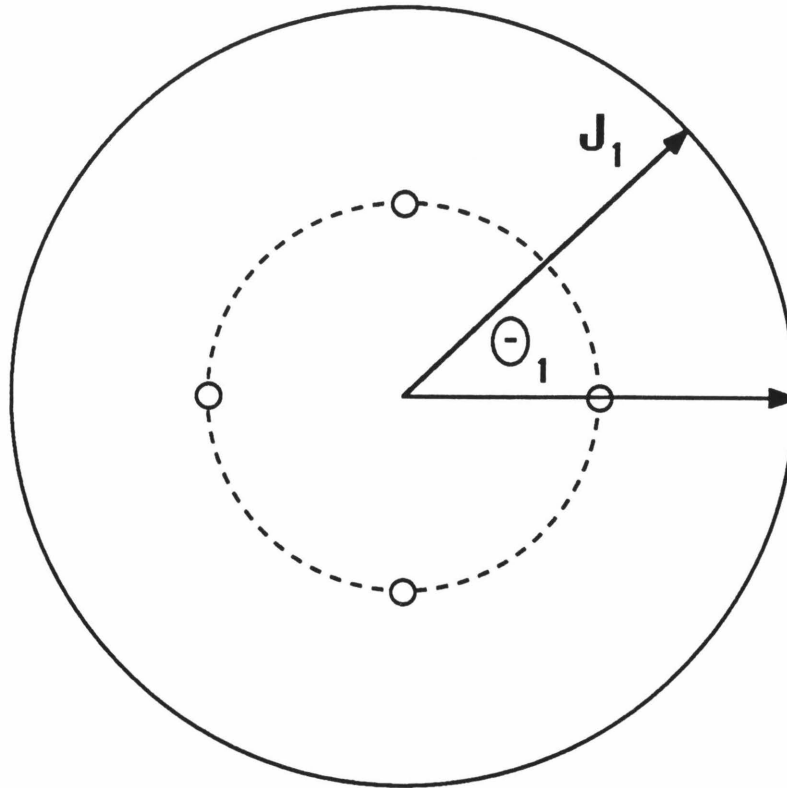


Figure 2.5 The surface of section of an integrable system is formally a twist mapping (2.3.1). J , the radial variable, is constant, while $\Delta\theta = 2\pi\alpha(J)$. The solid curve is an irrational torus; as $t \rightarrow \infty$ a trajectory will densely cover the torus. The dashed curve is a rational torus. The open circles show a typical trajectory for $s = 4$. If we were to graph only every fourth crossing, each of these rational trajectories would become a stable fixed point.

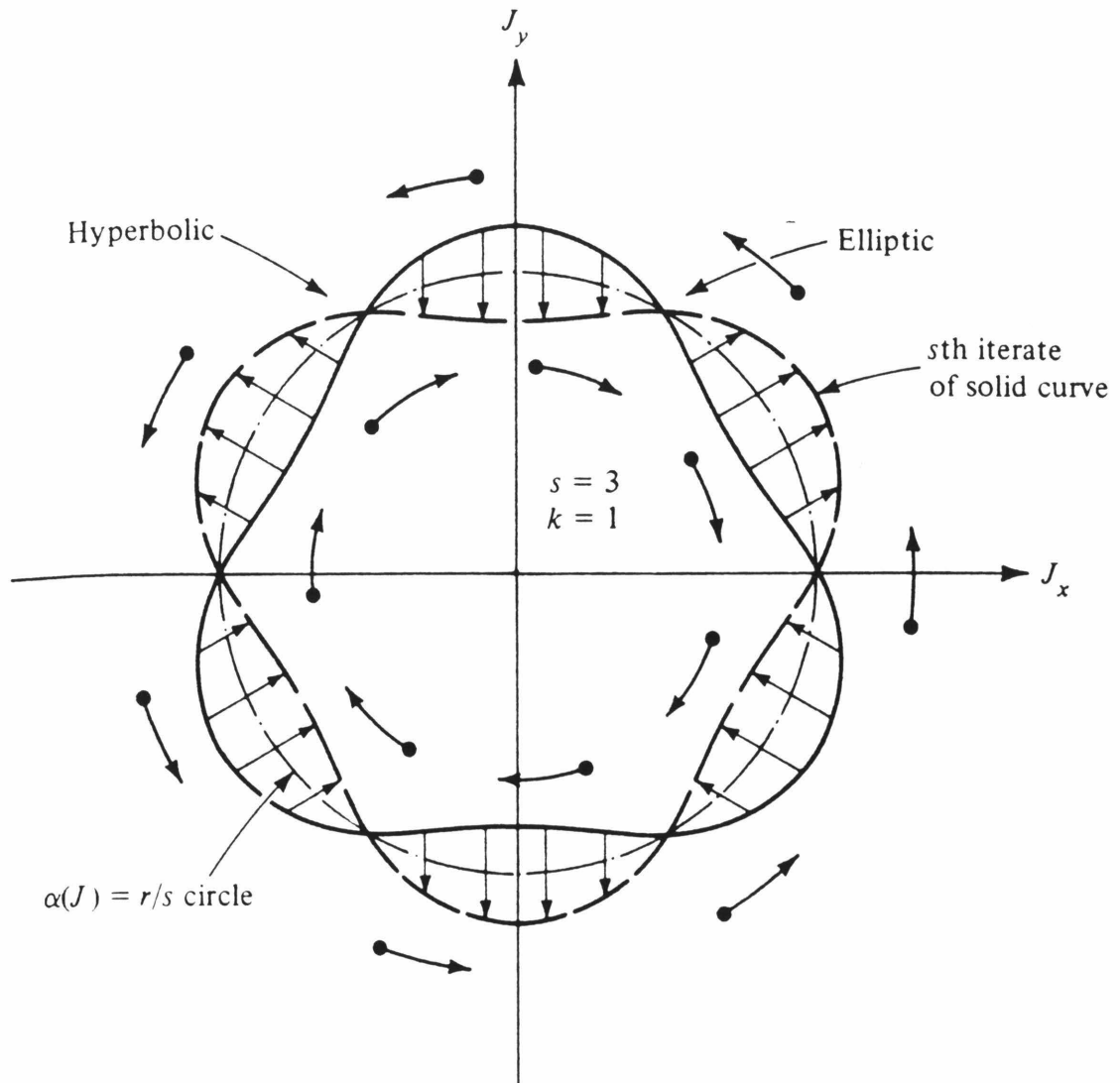


Figure 2.6 Illustration of a perturbed twist mapping for which both J and θ change. The rational torus of the unperturbed map is shown by the dash-dot line. For the perturbed map there is a curve which maps only radially (i.e., $\Delta\theta = 0$) under the s 'th iteration of the map; this is the dashed line. The $2s$ 'th iterate of that curve is the solid line. Where these two lines intersect there are stable and unstable fixed points of the s 'th iterate of the map. This is the Poincaré-Birkhoff Theorem. [LL83]

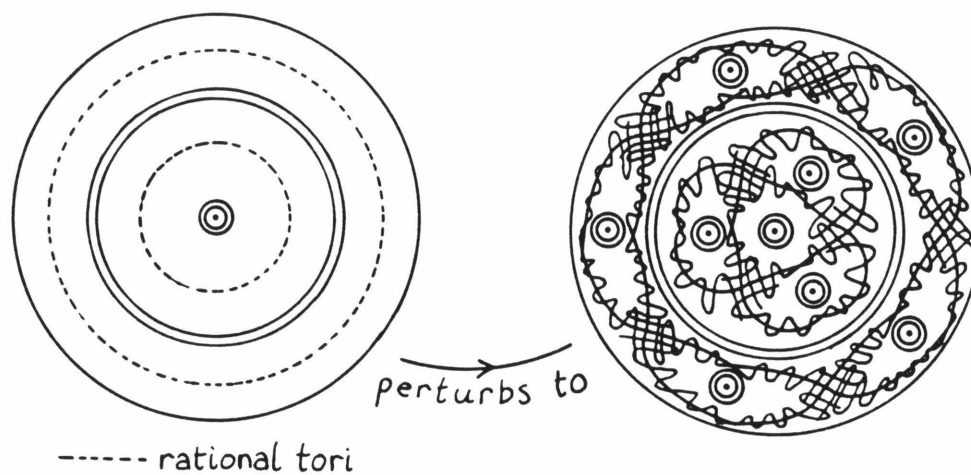


Figure 2.7 Illustration of the changes in the invariant tori under perturbation. The irrational tori are only slightly distorted, while the rational tori break up into alternating elliptic and hyperbolic fixed points. The elliptic fixed points are those that are surrounded by ellipses (i.e., second order islands). Separatrices emanate from the hyperbolic points. The behavior of the separatrices is shown in more detail in Figure 2.9. [Be78]

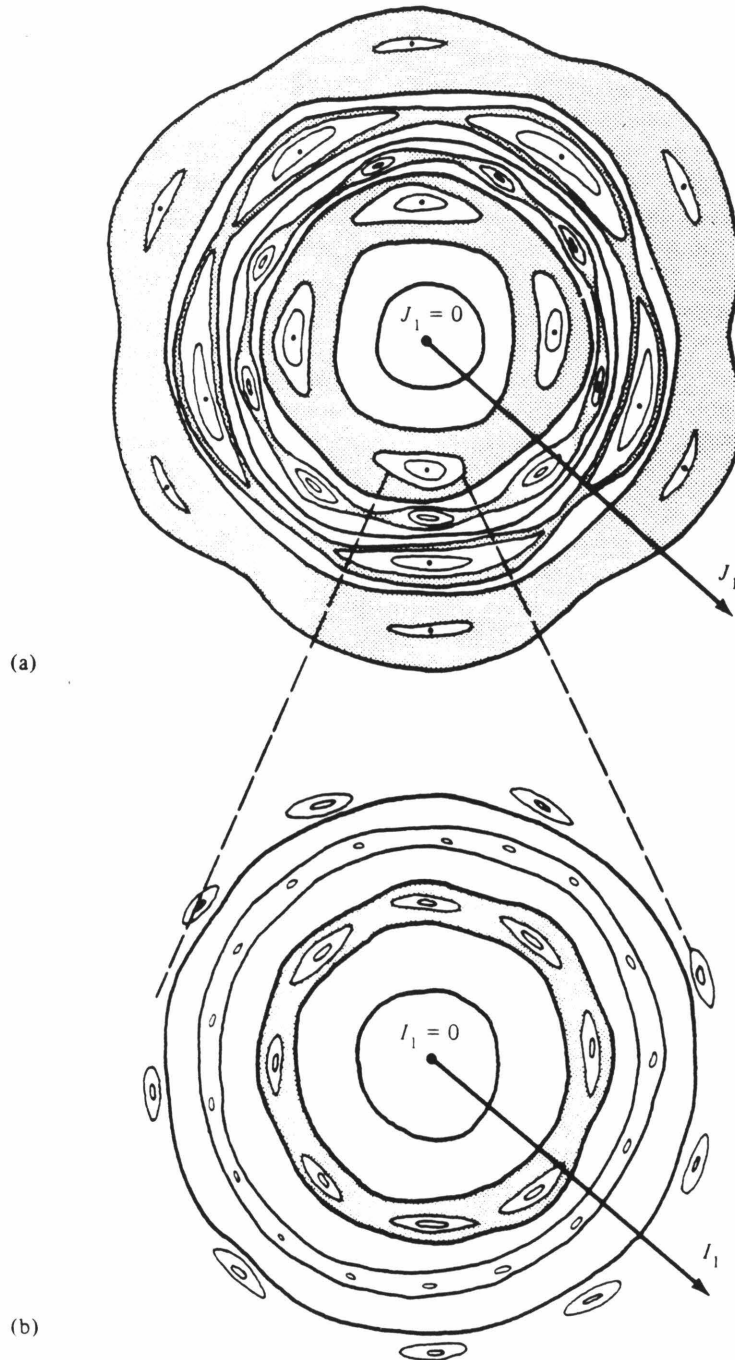


Figure 2.8 An illustration of the general features of phase space for a nonintegrable Hamiltonian. (a) The circles concentric with J_1 are KAM tori, the nonconcentric ellipses are second order islands which are centered on elliptic fixed points. (b) A magnification and circularization of the indicated second order island. Again there are KAM-like tori (actually second order islands) and second order islands (actually third order islands). This structure exists on every scale. The chaotic regions are not shown. [LL83]

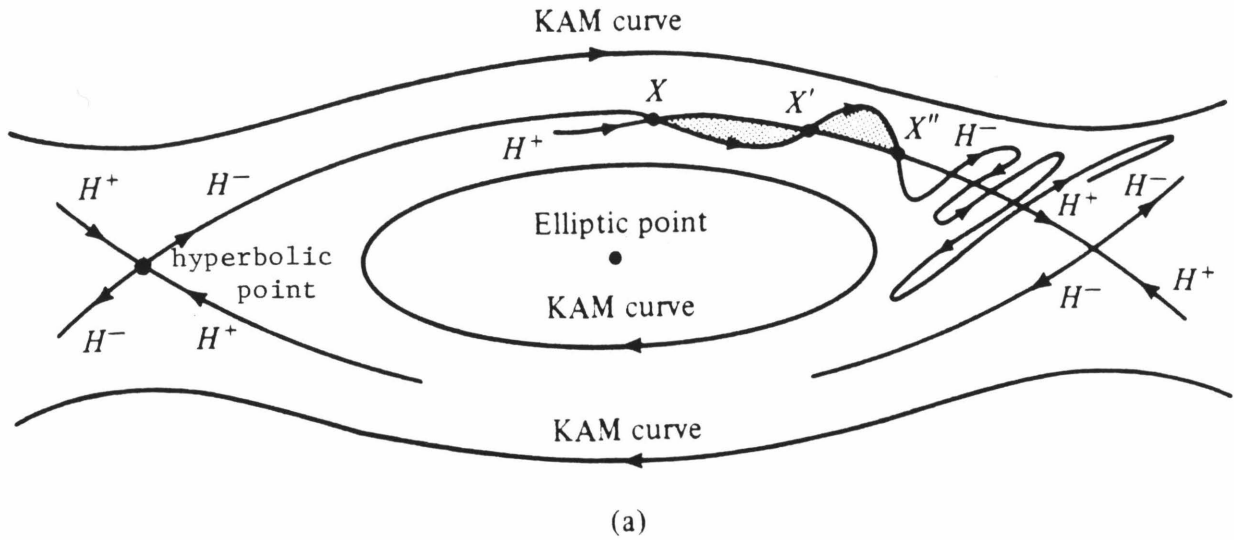


Figure 2.9 Wild behavior of separatrices. H^+ and H^- are the stable and unstable separatrices of a hyperbolic fixed point. Their intersections X, X', X'' are homoclinic points. The shaded areas (quasi-triangles) are equal because the mapping is area preserving. As the homoclinic points approach the hyperbolic fixed point, the “base” of the quasi-triangle becomes exponentially shorter, so the heights must become exponentially longer. This behavior of the separatrices is the origin of chaos. [LL83]

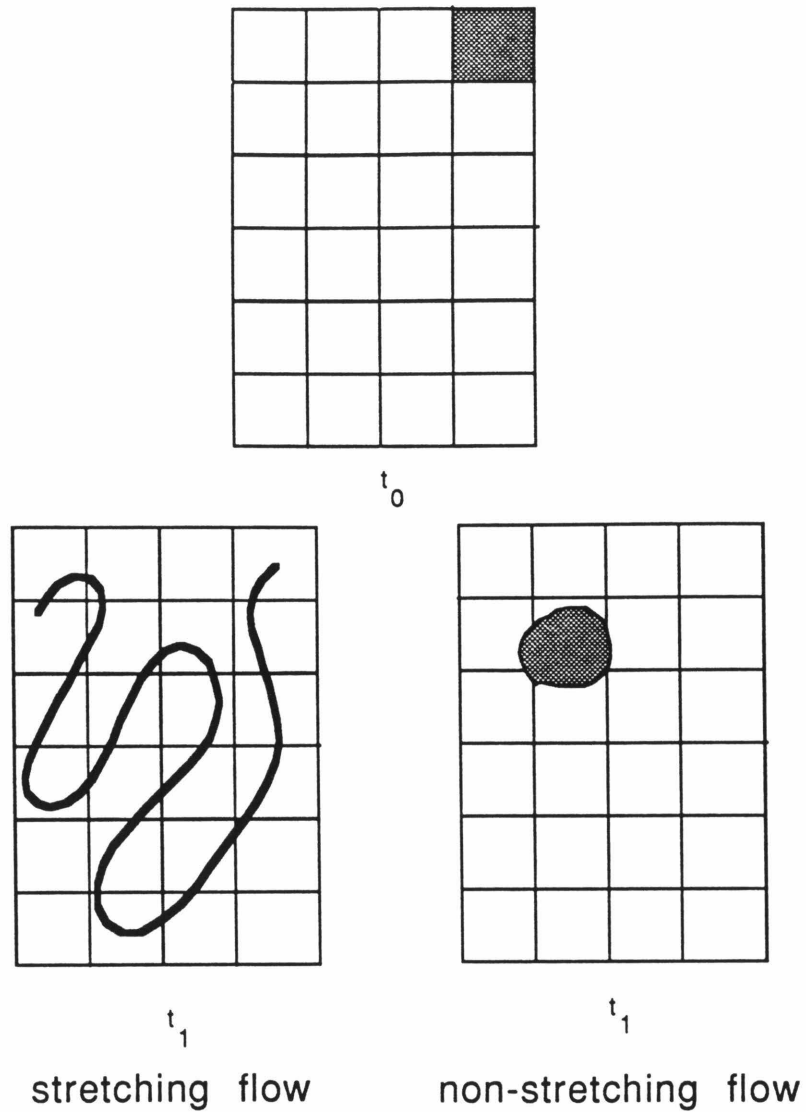


Figure 2.10 The Hamiltonian fluid evolves differently for stretching and non-stretching flows. Consider some bit of fluid which occupies one box at t_0 . For a stretching flow, at $t_1 > t_0$ the fluid covers nearly all the boxes, though its volume has not changed. This flow generates information. For a nonstretching flow the fluid covers approximately the same number of boxes for all times. This flow conserves information.

Chapter Three

Random Matrix Theory

We delay the discussion of quantum chaos to Chapter Four, and digress in order to take up a subject that provides the language to quantify differences between regular and irregular spectra: Random Matrix Theories (RMT). We will show that the salient features of spectra are fluctuation properties, i.e., deviations from some smooth behavior, and that these properties are universal, holding both for many physical systems, and for many kinds of random matrix ensembles.

3.1 Motivations

Dyson's summary [Dy62] gives the historical context and motivation which created this field of physics:

Recent theoretical analyses have had impressive success in interpreting the detailed structure of the low-lying excited states of complex nuclei. Still, there must come a point beyond which such analyses of individual levels cannot usefully go. For example, observations of levels of heavy nuclei in the neutron-capture region give precise information concerning a stretch of levels from number N to number $(N+n)$, where N is an integer of the order of 10^6 . It is improbable that level assignments based on shell structure and collective or individual-particle quantum numbers can ever be pushed as far as the million'th level. It is therefore reasonable to inquire whether the highly excited states may be understood from the diametrically opposite point of view, assuming as a working hypothesis that all shell structure is washed out and that no quantum numbers other than spin and parity remain good. The result of such an inquiry will be a statistical theory of energy levels. The statistical theory will not predict the detailed sequence of levels in any one nucleus, but it will describe the general appearance and degree of irregularity of the level structure that is expected to occur in any nucleus which is too complicated to be understood in detail.

In ordinary statistical mechanics a comparable renunciation of exact knowledge is made. By assuming all states of a very large ensemble to be equally probable, one obtains useful information about the over-all behavior of a complex system, when the observation of the state of the system in all its

detail is impossible. This type of statistical mechanics is clearly inadequate for the discussion of nuclear energy levels. We wish to make statements about the fine detail of the level structure, and such statements cannot be made in terms of an ensemble of states. What is here required is a new kind of statistical mechanics, in which we renounce exact knowledge not of the state of a system but of the nature of the system itself. We picture a complex nucleus as a “black box” in which a large number of particles are interacting according to unknown laws. The problem then is to define in a mathematically precise way an ensemble of systems in which all possible laws of interaction are equally probable.

This quote describes the field at its inception in the 1950’s; a collection of original papers on the subject are found in Porter’s book [P065], and a review article by Brody *et al.* [Br81] gives a summary of the developments in this field over the past thirty years.

The goal of RMT is to find an appropriate ensemble, and we will do this in analogy with the methods of statistical mechanics. We compare the ensemble of points in $2N$ dimensional phase space (for a system with N degrees of freedom) with an ensemble of Hamiltonians, i.e., an ensemble of Hermitian matrices of dimension \mathcal{N} . The general procedure of statistical theories is to substitute a calculation that can’t be done for one that can, losing detail in the process while retaining some physically interesting information. The difficult calculation in standard statistics is the long time evolution of a complicated system (e.g., 6.022045×10^{23} particles in three dimensions); the analogous quantum calculation would be the diagonalization of a large matrix (e.g., $\mathcal{N} = 10^6$).

Statistical mechanics realizes this simplification using the ensemble density ρ and the ergodic hypothesis. This density is defined by requiring that the time average of any observable

$$\bar{A} \equiv \frac{1}{T} \int_t^{t+T} A(t') dt'$$

is equal to the ensemble average

$$\bar{A} = \langle A \rangle ,$$

where

$$\langle A \rangle \equiv \int \rho A d^N q d^N p .$$

The ergodic hypothesis asserts that the ensemble ρ so defined exists. Using this ensemble density, we substitute the difficult time averages for the easier space averages. In this approach we cannot say anything about the details of the motion of a particular particle, or the state of the whole system at a particular time, but we may still calculate properties of the system.

Similarly, we would like for there to be an ergodic ensemble density $P(H)$ of Hamiltonians such that a spectral average for any member of the ensemble equals the ensemble average. Then, we would not need to know the details of the spectrum of a particular Hamiltonian; we would not have to calculate Dyson's millionth level; and we would instead be able to use information from the ensemble averages.

We will judge any ensemble candidate on the following criteria: physical plausibility (is there any reason we should believe that the Hamiltonian of the system of interest belongs to the ensemble we choose), agreement with experiment, ergodicity (otherwise the proposed substitution won't work), and computational tractability of the ensemble averages (the whole point is to make calculations possible).

In the next section, we will give three specific examples of ensembles, but before we begin that discussion, we must consider the proper measure of the matrices in the ensemble.

In statistical mechanics, the measure was simply the phase space measure $d^N p d^N q$ which is unchanged under canonical transformation of the coordinates. For random Hamiltonians, the measure depends on the number of different independent matrix elements. If the Hamiltonian is invariant under rotations and time reversal invariant (more accurately, if it commutes with any anti-unitary operator) then it must be real and symmetric. The other possibilities are quaternion real (time reversal invariant, non-rotationally invariant) and complex hermitian (non-time reversal invariant regardless of rotational symmetry). We will consider only time-reversal invariant and rotationally symmetric systems, and therefore will focus exclusively on real, symmetric matrices. An $\mathcal{N} \times \mathcal{N}$ such matrix has $\frac{1}{2}\mathcal{N}(\mathcal{N} + 1)$ independent matrix elements, and its eigenvalues and eigenvectors are invariant under orthogonal transformations.

Now that we know the independent elements, we return to the question of measure. We begin by defining the general metric $g_{\mu\nu}$ by the differential area ds^2 :

$$ds^2 = \sum_{\mu\nu} g_{\mu\nu} dx_\mu dx_\nu .$$

Demanding that ds^2 be orthogonally invariant, we choose

$$\begin{aligned} ds^2 &\equiv \text{Tr}(dH dH^\dagger) \\ &= \sum_{\mathbf{i}} (dH_{\mathbf{ii}})^2 + 2 \sum_{\mathbf{i} < \mathbf{j}} (dH_{\mathbf{ij}})^2 . \end{aligned}$$

The general metric induces the measure

$$dV = \sqrt{(\det g_{\mu\nu})} \prod_{\mu\nu} dx_{\mu\nu} ,$$

which gives for our real, symmetric matrices

$$dH = 2^{\mathcal{N}(\mathcal{N}+1)/4} \prod_{1 \leq \mathbf{i} \leq \mathcal{N}} dH_{\mathbf{ii}} \prod_{1 \leq \mathbf{i} < \mathbf{j} \leq \mathcal{N}} dH_{\mathbf{ij}} .$$

Just as the statistical mechanical measure is invariant under canonical transformations so that no particular expression of variables is preferred, so this measure of the matrices is invariant under orthogonal transformations so that no particular basis is favored over any other. This is because physics doesn't change under orthogonal transformations, so the measure shouldn't either.

3.2 Derivations of Matrix Ensembles

In the development of random matrix theory, many different ensembles were considered, each satisfying some of the criteria, but not all. As is usually the case, the desire for physical plausibility and mathematical tractability were at odds: no ensemble satisfied both. In this section we will look at two ensembles: the Two Body Random Ensemble (TBRE) which is physically reasonable and the Gaussian Orthogonal Ensemble (GOE) which is mathematically tractable.

The Two Body Random Ensemble belongs to the class of embedded ensembles. These are physically appealing because they contain information about the interaction. Specifically, the matrix elements are consistent with a ν -body interaction,

where ν is arbitrary, but fixed. The formalism of this ensemble is borrowed from second quantization and the shell model of nuclear physics. We consider m particles in Ω possible single particle states and a ν -body interaction, with $\Omega \geq m \geq \nu$. The Hamiltonian may be written using creation and annihilation operators:

$$H = \sum_{\alpha \leq \beta} W_{\alpha\beta} A_{\alpha}^{\dagger}(\nu) A_{\beta}(\nu),$$

where $A_{\alpha}^{\dagger}(\nu)$ creates ν particles with quantum numbers $\alpha_1, \alpha_2, \dots, \alpha_{\nu}$, and $W_{\alpha\beta} = \langle \alpha | H | \beta \rangle$ is a ν -body matrix element. Then the individual matrix elements are written

$$H_{ij} = \sum_{\alpha \leq \beta} W_{\alpha\beta} C_{\alpha\beta}^{ij},$$

with

$$C_{\alpha\beta}^{ij} \equiv \langle i | A_{\alpha}^{\dagger}(\nu) A_{\beta}(\nu) | j \rangle.$$

From this it is clear that the H_{ij} 's are not independent. Taking a specific case of twelve nucleons in the nuclear sd shell with $\nu = 2$, and requiring that spin= $J = 3$ and isospin= $T = 1$, there are 22,488,571 matrix elements, but only 63 are independent [Br81].

The embedded ensembles are defined by specifying the values of ν and the $W_{\alpha\beta}$'s. For the TBRE, $\nu = 2$, and the $W_{\alpha\beta}$'s are random variables chosen from a zero-centered distribution. This choice of the W 's makes all 2-body interactions equally probable, while the C 's keep the symmetries correct.

For any embedded ensemble, problems arise when calculations are attempted. All the difficulty resides in the C 's; these factors contain the angular momentum coupling, and the computational details can be overwhelming. Numerical calculations of ensemble averages are done by Monte Carlo methods; i.e., many (usually hundreds) of members of the TBRE are created by choosing the W 's according to the distribution, and the C 's according to angular momentum constraints. The desired function is then calculated for each matrix, and then averaged over all the matrices. Such numerical work can be informative, but not as satisfying as the analytical results which we will see are available for the GOE.

The GOE was developed from the opposite point of view, ignoring the dynamics of the physical system and demanding a computationally tractable result. The original derivation was given by Freidrichs and Shapiro [FS57], and Porter and Rosenzweig [PR60], but we will repeat a more heuristic, elegant, and general proof by Balian [Ba68]. His approach was to find the least biased distribution subject to given constraints. Such a distribution maximizes the information

$$I[P(H)] = - \int dH P(H) \ln P(H) .$$

This information is the continuum limit of the information defined by 2.4.3; all the ideas about information remain the same. If the constraints are of the form

$$\int dH P(H) F_i(H) = C_i ,$$

then the variational calculation gives

$$\begin{aligned} \delta I[P(H)] &= 0 \\ &= \int dH \delta P(H) \left(\ln P(H) + 1 - \sum_i \lambda_i F_i(H) \right) , \end{aligned}$$

defining the distribution

$$P(H) = \exp - \left(\sum_i \lambda_i F_i(H) - 1 \right) .$$

This is a very general formula and allows for derivation of many ensembles. We obtain the GOE by requiring only

$$\begin{aligned} \int P(H) dH &= 1 && \text{normalization} \\ \int \text{Tr}(H^2) P(H) dH &= C && \text{finite matrix ensemble strength.} \end{aligned}$$

Finally, the GOE result is

$$P_{\mathcal{N}}^{\text{GOE}}(H) = C_{\mathcal{N}} \exp \left(- \frac{\sum_{ij} H_{ij}^2}{4\sigma^2} \right) ,$$

where σ is related to the strength of the matrix elements and $C_{\mathcal{N}}$ is the normalization constant. Note that because the distribution depends only on the trace of H^2 , it

is invariant under orthogonal transformations. The naming of the ensemble should now be clear: the matrix elements are chosen from a Gaussian distribution, and the probability is invariant under orthogonal transformations.

In addition to the two constraints given above, the original derivation required that the matrix elements be statistically independent (in sharp contrast to the TBRE), and that $P(H)$ be invariant under orthogonal transformations; these were used in place of the maximal information requirement. Brody *et al.* point out that the “least biased” requirement implies statistical independence and orthogonal invariance, but the converse is not true, therefore “least biased” is a more fundamental constraint.

The time independent quantum problem focuses on eigenvalues and eigenvectors and not on the matrix elements; therefore, it is useful to change variables. First, we derive the probability distribution of the eigenvalues E_i . We denote the rotation angles that generate the orthogonal transformation to the diagonal basis by α_i . Because $\text{Tr}H^2$ is invariant, the dependence of $P(H)dH$ on α_i will come only from the Jacobian ($\equiv J(E, \alpha)$) of the transformation to the diagonal basis:

$$P(H)dH = P(E) J(E, \alpha) dE d\alpha .$$

General considerations give the E dependence of the Jacobian [Po65], and we integrate out the angular dependence to obtain the distribution of the eigenvalues:

$$P_{\mathcal{N}}^{\text{GOE}}(E) = C_{\mathcal{N}} \exp\left(-\frac{\sum_i^{\mathcal{N}} E_i^2}{4\sigma^2}\right) \prod_{i < j} |E_i - E_j| , \quad (3.2.1)$$

where the product term shows explicitly that there are no degenerate eigenvalues in the GOE.

To calculate the distribution of eigenvectors, we look at the probability distribution of $x_i \equiv \langle \lambda | i \rangle$, where i labels the eigenvector and λ labels a set of \mathcal{N} orthogonal basis vectors. We can derive this distribution on intuitive grounds. Because a given H and all of its orthogonal transformations $OH O^{-1}$ appear in the GOE with equal weight, the i th eigenvector and all its rotations also appear with equal weight.

Therefore the joint probability for the projection of a given eigenvector on each of the basis vectors must be spherically symmetric:

$$P(x_1, x_2, \dots, x_{\mathcal{N}}) = \pi^{-\mathcal{N}/2} \Gamma\left(\frac{\mathcal{N}}{2}\right) \delta\left[\sum_{i=1}^{\mathcal{N}} x_i^2 - 1\right], \quad (3.2.2)$$

where the delta function comes from requiring that the vectors be normalized, and the constants give proper normalization of the probability distribution. By similar arguments, 3.2.2 may also be interpreted as the joint probability for the projection of a given basis vector on all of the eigenvectors, i.e., i varies and λ is fixed.

These two distributions define the GOE. From these we can calculate the ensemble averaged density of eigenvalues, for example, by integrating $P_{\mathcal{N}}^{\text{GOE}}$ over all but one variable. Even for the GOE, the integrations were non-trivial, but the difficulties were solved by Wigner, Dyson, Gaudin, and Mehta [Po65], thus making this ensemble the “winner” in the mathematical tractability category. But there should be strong doubts about its physical relevance. In the language of the embedded ensemble, because all of the matrix elements are independent, the GOE is made up of H 's with all particles interacting simultaneously [Br81]; this is not very reasonable.

In the next few chapters, we will discuss the GOE ensemble averages for several functions of the eigenvalues and eigenvectors, compare these with experiments, and investigate the ensemble's ergodic properties. We will see that this ensemble satisfies three of the four criteria, and therefore deserves the attention which we will proceed to give it.

Before we continue with GOE, we introduce one last ensemble. The joint probability of the eigenvalues for the Poisson ensemble is given by

$$P_{\mathcal{N}}^{\text{Poisson}}(E) = C_{\mathcal{N}} \exp\left(-\frac{\sum_i^{\mathcal{N}} E_i^2}{4\sigma^2}\right), \quad (3.2.3)$$

which looks like the GOE distribution (3.2.1), but without the correlations. We may obtain such a spectrum as follows: take m picket fence spectra, i.e., spectra for which the spacing between eigenvalues is constant and equal to one; superimpose these spectra, each with its initial eigenvalue chosen at random to lie in the interval $[0,1]$; as $m \rightarrow \infty$ the resulting single spectrum has Poisson statistics [Pa79].

This distribution does have physical relevance. Berry and Tabor [BT76] proved that the spectra of completely integrable systems have nearest neighbor spacings characteristic of the Poisson ensemble. We can make this idea plausible by invoking the above theorem. Consider a system with two degrees of freedom, which therefore has two good quantum numbers p and q that label the eigenvalues. The m superimposed spectra are the spectra with fixed p , but varying q or vice versa. In the large energy limit, where many different p values coexist, we would expect the superposition theorem to apply, and for Poisson statistics to hold. Similarly, if there are M conserved quantities ($M < N = \text{degrees of freedom}$), i.e., for a quasi-integrable system, we would still expect Poisson statistics in the high energy limit where many spectra with different values of conserved quantities overlap.

Because Poisson statistics arise whenever there are any conserved quantities, it is imperative that we look at the spectral averages for pure spectra, i.e., spectra with constant values for all conserved quantities. In matrix language, the presence of a conserved quantity means that H may be written in block diagonal form. Therefore to examine pure spectra only, we study each smaller block diagonal matrix separately, and not the whole matrix all at once.

3.3 Global vs. Local Behavior

In this section we begin the investigation of the GOE ensemble averages of various spectral functions. (Only occasional mention will be made of other ensembles.)

The ensemble density of eigenvalues is given by the integration of the joint probability density over all but one variable

$$\begin{aligned} \bar{\rho}(E) &= \int \dots \int P_{\mathcal{N}}^{\text{GOE}}(E, E_2, \dots, E_{\mathcal{N}}) dE_2 dE_3 \dots dE_{\mathcal{N}} \\ &= \begin{cases} \frac{\sqrt{4\mathcal{N}\sigma^2 - E^2}}{2\pi\mathcal{N}\sigma^2} & \text{for } |E| \leq 2\sqrt{\mathcal{N}\sigma^2} \\ 0 & \text{for } |E| \geq 2\sqrt{\mathcal{N}\sigma^2}. \end{cases} \end{aligned} \quad (3.3.1)$$

This result is known as the Wigner semicircle law. This GOE average does not agree with experiment. Highly excited nuclear levels, for example, follow an exponential behavior

$$\rho(E) \approx \frac{C}{(E - \Delta)^{5/4}} \exp(a\sqrt{E - \Delta}),$$

where a , Δ , and C depend on the nucleus. In general, there is no reason to expect nature's variety of Hamiltonians to agree with this prediction. This may indicate that the GOE should be abandoned since it seems to have no connection with physical reality. However, while GOE fails miserably at calculating the global property of the level density, we shall see (§3.4) that it succeeds at predicting local fluctuations from the long range smooth behavior.

There is, however, a good reason for accepting this apparent discrepancy in predictive powers of the GOE. Global and local behavior are on different energy scales, and as such we'd expect them to be uncoupled. We write $N(E)$ = the number of eigenvalues with energy less than E (a staircase function) as the sum of two parts

$$N(E) = N_{\text{ave}}(E) + N_{\text{fluct}}(E)$$

to indicate this decoupling. The separation between average and fluctuating is somewhat arbitrary, but it is important to do it in an unbiased manner (e.g., cubic spline smoothing of $N(E)$).

To study the fluctuations alone, we first “unfold” the spectrum to take out the average behavior. This is done via the mapping of $E_i \rightarrow x_i$

$$x_i = N_{\text{ave}}(E_i) . \tag{3.3.1}$$

Unfolding does not change the average number of levels below a given level, therefore

$$N_{\text{ave}}(E) = \hat{N}_{\text{ave}}(x(E)) ,$$

where N_{ave} and \hat{N}_{ave} have the same meaning, but different functional forms. Combining the last two equations, we see that unfolding makes the average distance between eigenvalues equal to one:

$$\hat{N}_{\text{ave}}(x) = x$$

giving

$$\hat{\rho}_{\text{ave}}(x) \equiv \frac{d\hat{N}_{\text{ave}}(x)}{dx} = 1 .$$

This is equivalent to measuring all spacings in units of the average local energy spacing. Therefore we may compare spectra from very different systems and still hope to see universality in spectral averages of various functions.

3.4 Spectral Fluctuations

Up until now we have spoken in general about spectral averages of functions of eigenvalues, the only specific example has been $P(s)$, the nearest neighbor spacing distribution. In this section we will introduce five eigenvalue functions that measure spectral fluctuations, and their spectral averages.

One way to characterize a spectrum is by the set of spacing distributions $E(\alpha, k, L)$, that give the probability that an interval beginning at $x = \alpha$ of length L contains exactly k levels

$$E(\alpha, k, L) \equiv \lim_{\mathcal{N} \rightarrow \infty} \frac{\mathcal{N}!}{(\mathcal{N} - k)!} \times \int_{\alpha}^{\alpha+L} \dots \int_{\alpha}^{\alpha+L} dx_1 \dots dx_k \left[\int_{-\infty}^{\alpha} + \int_{\alpha+L}^{\infty} \right] \dots \left[\int_{-\infty}^{\alpha} + \int_{\alpha+L}^{\infty} \right] dx_{k+1} \dots dx_{\mathcal{N}} P_{\mathcal{N}}(x_1, \dots, x_{\mathcal{N}}).$$

In general, the function depends on the value of α , but if the ensemble is stationary, as will be discussed in §3.6, this dependence disappears. We will assume that this is the case. The set of $E(k, L)$ for all values of L and k tells us everything about the spectral fluctuations for a given ensemble. We will actually focus on only a few spectral measures for obvious practical reasons. Each measure that we discuss may be written in terms of $E(k, L)$ [BG84], but we will introduce them independently of these measures.

For reference, we will quote results for picket fence and Poisson ensembles as well as GOE. All results quoted will be for ensemble averages in the $\mathcal{N} = \infty$ limit.

The nearest neighbor spacing $P(s)$ is the probability that two consecutive eigenvalues are a distance s apart. To motivate the GOE result, we repeat an early argument due to Wigner [Wi57]. If $\mathcal{N} = 2$, the matrix is defined by three independent matrix elements. The set of points in this three parameter space that gives degeneracy is a line. Therefore the probability of choosing a matrix at random for which $s = 0$ is zero; this is known as level repulsion. The full result for this 2×2 case is known as Wigner distribution

$$P_W(s) = \frac{\pi}{2} s e^{-(\pi/4)s^2}. \quad (3.4.1)$$

The result for $\mathcal{N} = \infty$ [Ga61] is not known in closed form, but is so close to $P_W(s)$, that the latter is often used for comparison (Figure 3.1). We will follow this custom.

The results for a Poisson spectrum may be derived by invoking the lack of correlations between eigenvalues [Wi67]. Let s be the interval $[x_0, x_0 + s]$ and ds the next little interval $[x_0 + s, x_0 + s + ds]$. Then the probability, given a level at x_0 , that the next level is in ds is

$$P(s)ds = P(1 \in ds|0 \in s)P(0 \in s) ,$$

where $P(1 \in ds|0 \in s)$ is the conditional probability that there is one level in ds if there is none in s , while $P(0 \in s)$ is the probability that there is no level in s . For the Poisson spectrum, the conditional probability is independent of s because of the lack of correlations between eigenvalues. We may write

$$P(0 \in s) = C \int_s^\infty P(s') ds' ,$$

since the probability that there is no level in s is the same as the probability that the next level is further away than s . Putting this together and solving, we find

$$P(s) = Ce^{-s} ,$$

where the constant is determined by normalization requirements. In this case degeneracy is most probable, i.e., there is level clustering.

For the picket fence spectrum, $P(s)$ is a delta function spike at $s = 1$.

The number statistic $n(\alpha, L)$ gives the number of levels in the energy interval $[\alpha, \alpha + L]$. Because the spectra are unfolded, the average over an ensemble gives $\bar{n}(L) = L$; therefore, this is not an interesting measure. However, the moments of the number statistic will not be the same for different ensembles. Specifically, we are interested in the ensemble averages

$$\begin{aligned} \Sigma^2(L) &\equiv \overline{(n(\alpha, L) - \bar{n}(\alpha, L))^2} \\ \gamma_1(L) &\equiv \frac{\overline{(n(\alpha, L) - \bar{n}(\alpha, L))^3}}{\Sigma^3(L)} \\ \gamma_2^2(L) &\equiv \frac{\overline{(n(\alpha, L) - \bar{n}(\alpha, L))^4}}{\Sigma^4(L)} - 3 , \end{aligned} \tag{3.4.2}$$

known as the variance, skewness, and excess (or kurtosis). The appearance powers of the variance in the denominator of γ_1 and γ_2 gives the third and fourth moments in terms of a natural scale. Note that both of these statistics are zero for a Gaussian distribution. The results for the three ensembles are [Br81]

	$\Sigma^2(L)$	$\gamma_1(L)$	$\gamma_2(L)$	
picket fence	0	0	0	
GOE	$\frac{2}{\pi^2} \ln L + 0.44 \quad (L > 1)$	-	-	
Poisson	L	$1/\sqrt{L}$	$1/L$	(3.4.3)

The values for GOE skewness and excess are not known in closed form, but are displayed in Figure 3.3. From these formulas it is clear that the Poisson ensemble shows dramatically greater variations than GOE. For example, $\Sigma^2(100) = .93$ for GOE and $= 100$ for Poisson.

The last statistic of interest to us is the Δ_3 measure of spectral rigidity. This is defined by

$$\Delta_3(\alpha, L) \equiv \min_{A, B} \frac{1}{L} \int_{\alpha}^{\alpha+L} [N(x) - (Ax + B)]^2 dx, \quad (3.4.4)$$

where $N(x)$ is the step function giving the number of eigenvalues with energy less than x . The minimization condition may be used to evaluate A and B , giving

$$\Delta_3(\alpha, L) \equiv \frac{1}{L} \int_{-L/2}^{L/2} d\tilde{x} N^2(\tilde{x}) - \left[\frac{1}{L} \int_{-L/2}^{L/2} d\tilde{x} N(\tilde{x}) \right]^2 - 12 \left[\frac{1}{L^2} \int_{-L/2}^{L/2} d\tilde{x} \tilde{x} N(\tilde{x}) \right]^2, \quad (3.4.5)$$

where $\tilde{x} \equiv x - (\alpha + L/2)$.

Δ_3 measures the square of the deviation from the best fit straight line over some subinterval. Over the entire spectrum, the best fit straight line has a slope of one since the spectrum is unfolded, but over a smaller interval of length L , that may not be true. The ensemble averages are [DM63]

	$\overline{\Delta}_3(L)$		
picket fence	1/12		
GOE	$\frac{1}{\pi^2} \ln L - 0.007 \quad (L > 15)$		
Poisson	$L/15$		(3.4.6)

The picket fence value is not zero because Δ_3 tries to fit a straight line to a crooked one. Δ_3 measures the stiffness of a spectrum. For a stiff spectrum, given the location of one eigenvalue one can predict with some certainty the location the the m th nearest neighbor. For a picket fence, this is can be done with absolute certainty, for the GOE with less confidence, and for the Poisson with practically no confidence at all, and the predictions get worse with larger m . We note that, for large L , $\text{Var}\Delta_3(L) = .0017L^2$ for Poisson and $= .012$ for GOE [DM63]. This again confirms that the Poisson variations overwhelm GOE variations.

Figure 3.2 shows the values of $E(k, L)$ for the three ensembles; these graphs are a clear reflection of rigidity of the picket fence and the softness of the Poisson ensemble.

3.5 Eigenvector Distribution

In the last section, we examined ensemble averages of spectral fluctuations; now, we do the same for the eigenvectors. Here the results are for the GOE only; there are no other ensemble results for comparison.

From the joint distribution for $x_i = \langle \lambda | i \rangle$ (3.2.2), we derive the distribution for one x_i

$$\begin{aligned} \rho(x) &= \int \dots \int P(x, x_2, \dots, x_{\mathcal{N}}) dx_2 \dots dx_{\mathcal{N}} \\ &= \frac{1}{\sqrt{\pi}} \Gamma\left(\frac{\mathcal{N}}{2}\right) \Gamma\left(\frac{\mathcal{N}-1}{2}\right)^2 (1-x^2)^{(\mathcal{N}-3)/2} \\ &\rightarrow \left(\frac{\mathcal{N}}{2\pi}\right)^{1/2} \exp(-x^2\mathcal{N}/2), \end{aligned} \tag{3.5.1}$$

the last line obtains only when $\mathcal{N} \rightarrow \infty$. Changing variables to the square of the overlap, $y = x^2$, the probability becomes

$$\rho(y) = \left(\frac{\mathcal{N}}{2\pi}\right)^{1/2} \frac{1}{\sqrt{y}} \exp(-y\mathcal{N}/2)$$

which is commonly known as the Porter-Thomas distribution, or a χ^2 distribution for one degree of freedom.

We may extend these notions to talk about strength fluctuations, where the strength is written

$$y \equiv |\langle f | T | i \rangle|^2,$$

i is a fixed initial state, T is an operator, and f is the final state which varies over the eigenvectors. In the language of the previous paragraph, $T|i\rangle$ is a basis vector.

As an additional complication, we will be interested in f chosen not from the entire set of eigenvectors, but from some smaller set of states. In nuclear physics we might imagine this smaller set to be the states corresponding to highly excited states with many particle-hole pairs. Then if we choose $|i\rangle$ as a low lying state, the transition strength between the highly excited states and this state will be fragmented: no one state will carry most of the weight. In this scenario the statistical treatment of the strengths is a reasonable approach. A basis vector in this d -dimensional subspace is

$$|\lambda\rangle \equiv \mathcal{P}T|i\rangle$$

where

$$\mathcal{P} \equiv \sum_{j=1}^d |j\rangle\langle j|$$

is the projection operator on the subspace. To normalize the basis, we calculate the total strength

$$\sigma_i^2 = \sum_{j=1}^d |T_{ji}|^2 = \langle i|T^\dagger \mathcal{P}T|i\rangle.$$

Redefining y

$$y \equiv \frac{|\langle f|T|i\rangle|^2}{\sigma_i^2}$$

as the overlap between an eigenvector and a normalized basis vector of the subspace, we may invoke the Porter-Thomas result for y . Making one final change of variables $z \equiv yd$, we obtain

$$\rho(z) = \left(\frac{1}{\pi z}\right)^{1/2} \exp(-z/2).$$

But we must consider the secular variations of the strength. The greater $|E_i - E_f|$, the smaller the transition strength. This variation is taken out in a fashion similar to the unfolding of the eigenvalues. We calculate σ_i as a function of the energy:

$$\sigma_i^2(E) \equiv \frac{\sum_{j=1}^d |\langle j|T|i\rangle|^2 \delta(E - E_j)}{\sum_j \delta(E - E_j)}.$$

Histogramming

$$z \equiv \frac{|\langle f|T|i\rangle|^2}{\sigma_i(E_f)^2}$$

for each state f in the subspace will give the Porter-Thomas distribution if the matrix is a member of the GOE.

Finally, we might also be interested in the case where both i and f are in the same subspace. The above discussion still holds, except that $\mathcal{P}_d \rightarrow \mathcal{P}_{d-1}$ where the last operator projects on all states in the subspace except $|i\rangle$ [Br81].

3.6 Ergodicity and Stationarity

We have just examined ensemble averages for various spectral and eigenvector functions for three ensembles, but we need to know if these averages equal the spectral averages for individual members of each ensemble. If this is true, then the original program of substituting ensemble averages for spectral averages may be carried out with confidence.

Denoting a spectral average by $\langle f \rangle$ and an ensemble average by \bar{f} , we may write the ergodic property

$$\langle f(E, \xi) \rangle \rightarrow \bar{f}(E, \xi)$$

where ξ denotes a member of the ensemble and E is energy. Ergodicity only obtains in the large \mathcal{N} limit, just as ergodicity of a dynamical system obtains only in the large time limit. Since the left hand side is independent of E , and the right is independent of ξ , they must both be equal to a constant. Ergodicity is independence of the spectral average from ξ ; stationarity is the independence of the ensemble average from E .

We must take into account a few practical considerations. First, what is the effect of finite \mathcal{N} ? Will ensemble averages for $\mathcal{N} = \infty$ be well approximated by the result for smaller matrices? The answer seems to be yes. For example $P(s)$ for $\mathcal{N} = 2$ is almost indistinguishable from the infinite \mathcal{N} result (Figure 3.2). Early work by Rosenzweig and Porter also shows that the asymptotic form of $\bar{\rho}(E)$ is approached quite rapidly; \mathcal{N} as small as 20 gives good agreement. Working at finite \mathcal{N} , therefore, does not seem to be a problem.

Second, what if we want to average only over a portion of the entire spectrum? In most practical cases there is no way to obtain the complete spectrum. Then we are not interested in global (in terms of energy) ergodicity, but local ergodicity where we average over a part of the spectrum centered at E , of length Δ , and containing on the average p eigenvalues. In the limit that $\mathcal{N} \rightarrow \infty$ and then $p \rightarrow \infty$, a measure f is locally ergodic if

$$\overline{\langle f(E, \xi) \rangle} \rightarrow \bar{f}(E, \xi)$$

and

$$\text{Var}\langle f(E, \xi) \rangle \equiv \overline{\langle f(E, \xi) \rangle^2} - \overline{\langle f(E, \xi) \rangle}^2 \rightarrow 0 \quad (3.6.1)$$

which give

$$\langle f(E, \xi) \rangle \rightarrow \bar{f}(E, \xi) .$$

It is easy to show that the first requirement holds in the limit that $\Delta \rightarrow 0$, which will happen if we take the limits $\mathcal{N} \rightarrow \infty, p \rightarrow \infty$ in the correct order. Proving the second requirement is more difficult, and depends on f . Pandey proved local ergodicity for all k-point correlation functions for both the GOE and Poisson Ensembles [Pa79], thereby implying ergodicity for all fluctuations measures that are derived from them. This includes $n(L)$, all moments of $n(L)$, and the Δ_3 statistic. He also showed the stationarity of fluctuation properties over the ensemble. Local ergodicity has also been proved for functions of the strength [Br81]. We should note that the picket fence “ensemble” is trivially ergodic and stationary simply because all members of the ensemble are the same, and the spectrum is the same at all energies.

Local ergodicity holds in the limit that $p \rightarrow \infty$, which is a practical impossibility. However, the ergodic theory allows us to predict the ensemble average of variations for spectral averages when a finite p is used.

3.7 Comparison with Experiment

The Poisson, GOE, and picket fence ensembles are all ergodic and have calculable ensemble averages for several spectral measures. But to what ensemble do real physical systems belong? According to the discussion in §3.2 there is no *a priori*

reason to suspect that they belong to the GOE, however, we will proceed to show that this is apparently the case.

It is not easy to obtain experimental data to compare with ensemble averages because the requirements are quite stringent. What we need are long, pure, complete sequences of eigenvalues and eigenvectors. Long, because we need many data points for reasonable statistical analysis. Pure, because combining eigenvalues from two different spectra will give Poisson statistics, no matter what the statistics of the two individual spectra are. And complete, because missing even a few levels will certainly affect the level fluctuations.

The best experimental results have come from neutron resonances in heavy nuclei. The resonances just above neutron threshold are well separated since their widths are much smaller than their separation. For example, in heavy nuclei the width is about 1eV, while the separation is 10eV [BG83]. If low energy neutrons are collided with even-even nuclei, the resulting resonance will have J^π of $1/2^+$, i.e., the spin and parity of the neutron, assuming that the energy is low enough that only s -waves are present. This method can give up to 200 levels, but typically only 50 or less. The limitations arise from the intrusion of p waves and the increasing resonance widths at higher energies. This is not enough for convincing statistical analysis.

However, in 1982 Haq, Pandey and Bohigas [HPB82] created the nuclear data ensemble (NDE) by combining the results from 27 nuclei, to give 1726 levels, enough to give good statistics. They calculated spectral averages of $P(s)$ and $\Delta_3(L)$ for each sequence of levels, and then combined the results. The results shown in Figure 3.3 are in excellent agreement with GOE predictions. A few years later [BHP85] they complimented their early work by calculating higher order statistics (the variance, skew and excess of the $n(L)$) for the same NDE, again obtaining excellent agreement with GOE.

More limited data is also available from atomic and molecular spectra [BG84]. Reasonable agreement is seen, but nothing as convincing as in the nuclear case. Unexpected support for GOE fluctuations also come from low lying nuclear levels [FM73,Br76]. If the spacings of the two lowest eigenvalues of the same spin and

parity for different nuclei are plotted as a function of A , a smooth variation is seen, analogous to the smooth variations in $\rho(E)$. If these spacings are unfolded (in A), and the results histogrammed, we see the level repulsion characteristic of GOE. Numerical work also shows that the fluctuations of TBRE are similar to those of GOE [WF79,BG75].

Reduced widths of neutron and proton resonances provide a check on GOE strength fluctuations [Br81]. These are experimentally accessible in the resonance regime, again because these states are well separated in energy. A reduced width, γ_i , (the width divided by the barrier penetration factor) is essentially the square of the matrix element between the incoming channel and the resonance. If we histogram $\gamma_i/\langle\gamma(E_i)\rangle$, where $\langle\gamma(E_i)\rangle$ is the average reduced width at that energy, we do see the Porter-Thomas distribution (Figure 3.4).

Finally, large scale nuclear shell model calculations yield eigenvalues and eigenvectors, and strengths may be calculated using these results. Looking at $E2$ (electric quadrupole) transitions, we do see the GOE result, but only if the secular variation of the strength is taken into account as advised in §3.5.

This large and varied body of evidence seems to indicate that Hamiltonians describing complicated systems do belong to the GOE ensemble. And because the GOE is ergodic, we may substitute ensemble averages for spectral averages when the spectral averages are unknown.

However, the ensemble is still not physically motivated. We may either take the viewpoint that the successes of the GOE are puzzling, or we may assert that the successes tell us something important about the nature of complicated systems, viz., the fluctuation properties of complicated systems are devoid of information [Wi84].

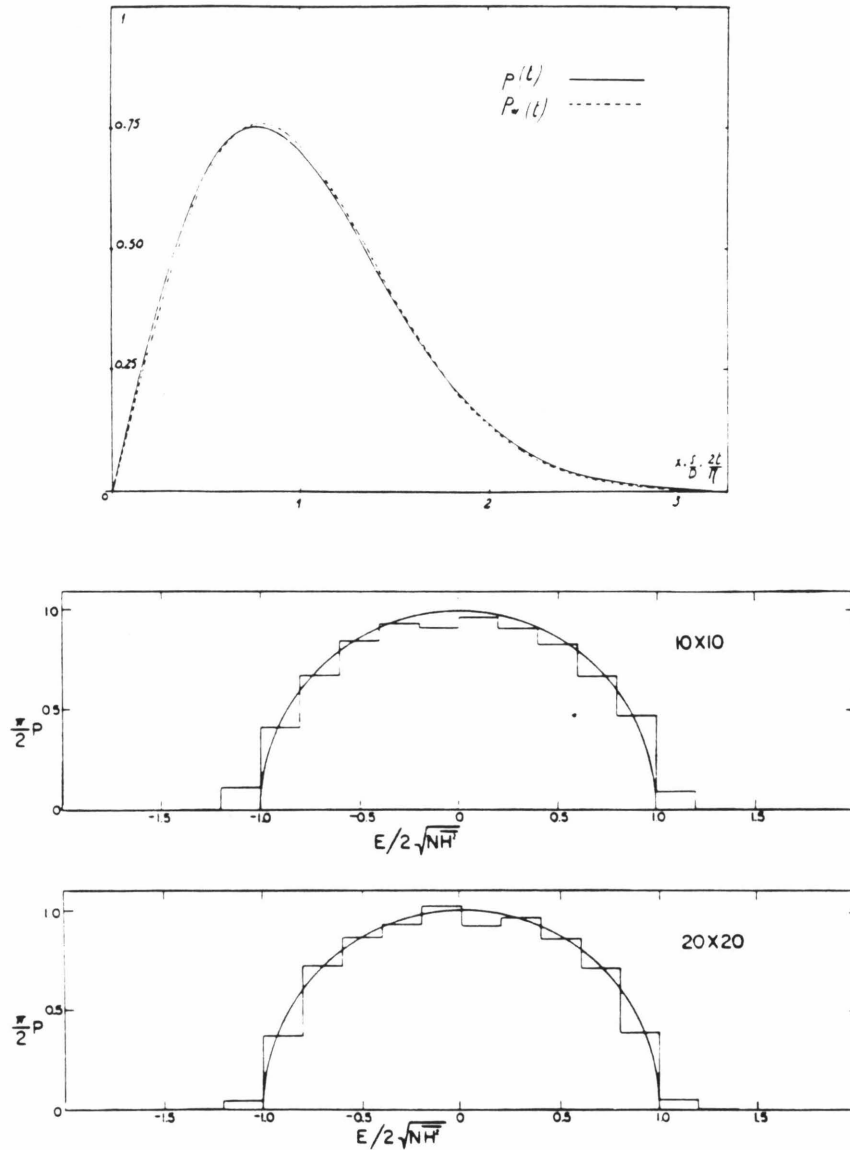


Figure 3.1 (a) GOE ensemble average of $P(s)$. The solid line is the result for $\mathcal{N} = \infty$, the dashed line is for $\mathcal{N} = 2$, and is known as Wigner's surmise. The agreement is almost exact [Ga61]. (b) GOE ensemble average of the density of states $\rho(E)$ for $\mathcal{N} = \infty$ (solid line) and $\mathcal{N} = 10$ and 20 (the histograms). Again, the agreement is quite good, indicating a rapid approach to the asymptotic \mathcal{N} results [PR60].

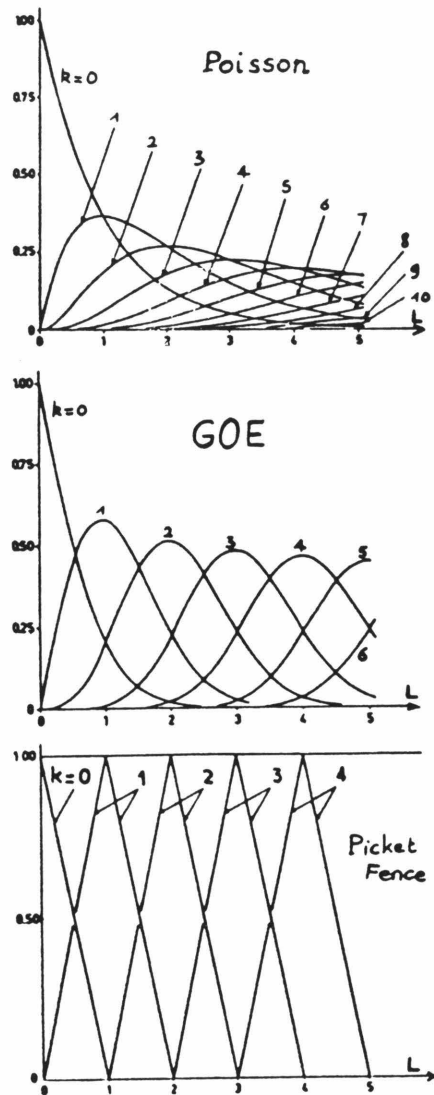


Figure 3.2 Ensemble averages of $E(k, L)$, the probability that an interval of length L contains exactly k levels, for the Poisson, GOE, and picket fence ensembles. These graphically show the stiffness of the picket fence ensemble and the softness of the Poisson [MdC72].

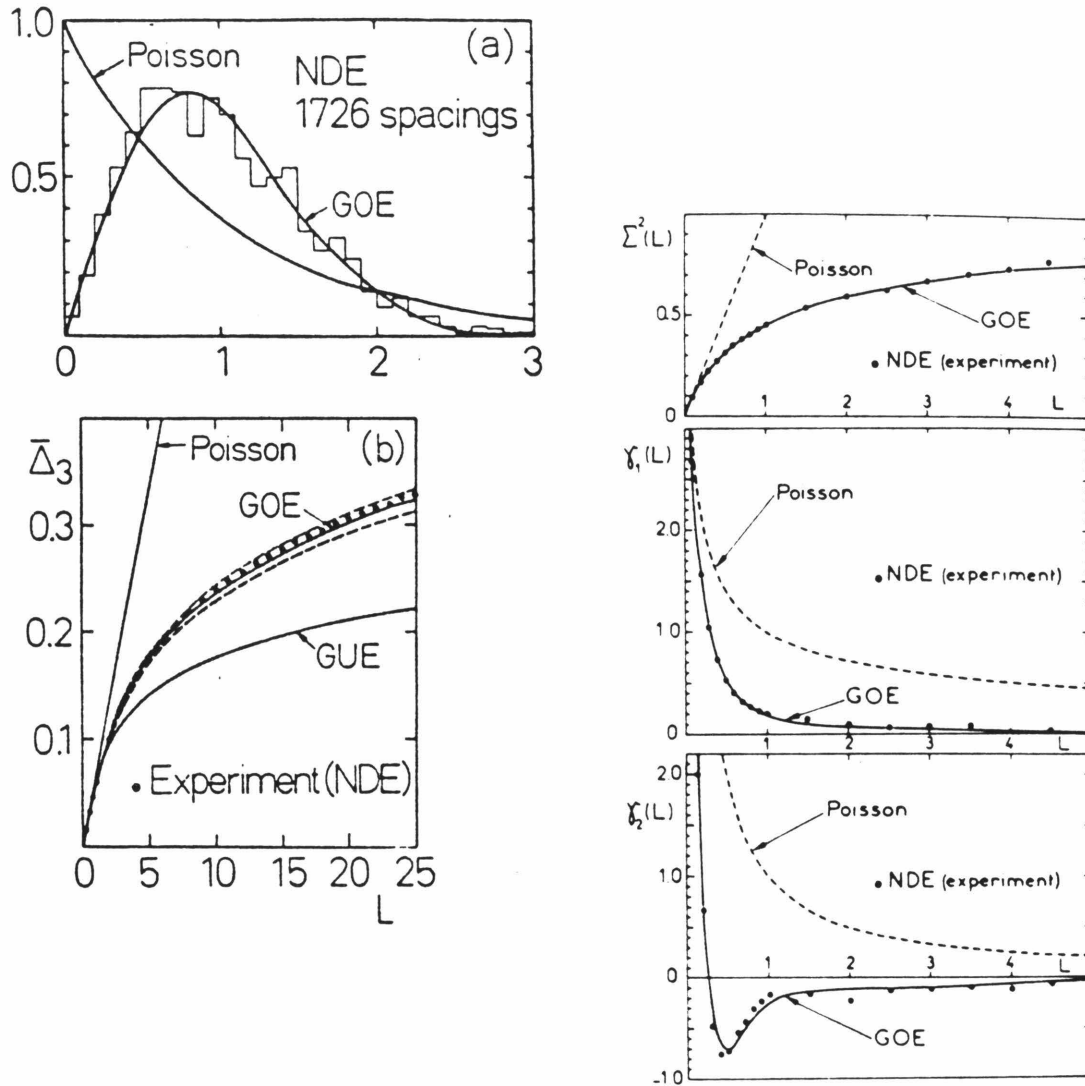


Figure 3.3 Spectral fluctuations of the Nuclear Data Ensemble (NDE) [HPB82, BHP85] consisting of 1726 neutron and proton resonance levels from 27 nuclei even-even nuclei. Nuclei included in the ensemble are Cd, Sm, Gd, Dy, Er, Yb, W, Th, U, Ca, Ti, and Hf. The agreement of the NDE averages with GOE averages is excellent. GUE stands for Gaussian Unitary Ensemble, and is appropriate for systems without time-reversal invariance. The Uncorrelated Wigner (UW) ensemble has the Wigner distribution for $P(s)$, but no other correlations.

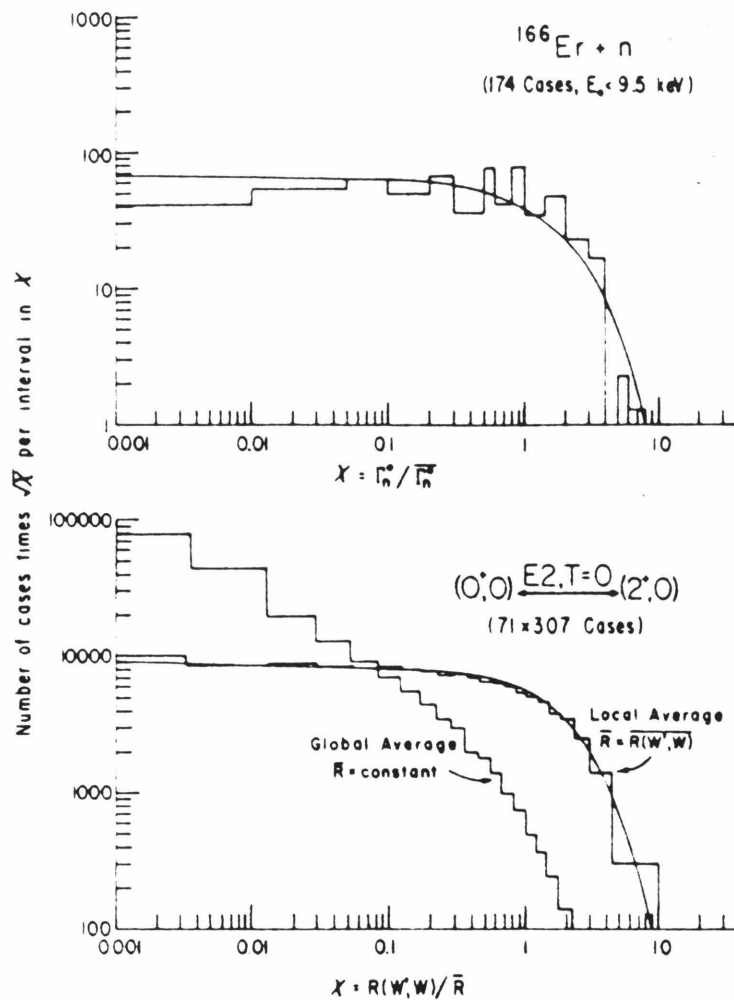


Figure 3.4 Strength fluctuations. (a) Reduced neutron widths fluctuations for $^{166}\text{Er} + n$ show good agreement with Porter Thomas distribution [Li72]. (b) Dipole transitions calculated between two shell model spaces (sd shells with $T=1$ and $J=0,2$) show good agreement with Porter-Thomas when the secular variation of the strength is taken into account, but display quite a different behavior when it is ignored [DFW77].

Chapter Four

Quantum Chaos

In this chapter we will bring together the previously unrelated fields of nonlinear dynamics and Random Matrix Theories, as well as semiclassical arguments, in order to describe chaotic quantum systems - systems whose classical analog is chaotic. The contents of this chapter is not a complete history of this new field, but a description of the work that has most influenced ours. For broader and more in depth discussions the interested reader may refer to CF79, SN86, Ca85, BG83, and Za81.

4.1 Billiards

Billiards, i.e., one particle in a two-dimensional box, have been a favorite subject for quantum chaologists. They are appealing for many reasons: depending on the boundary conditions, the system can either be regular or completely chaotic; the dynamics are independent of energy so that stationarity of the fluctuations of the eigenvalues is expected; they are relatively simple systems; and efficient numerical methods exist for calculating their eigenvalues [Be81].

The first numerical work was done by McDonald and Kaufman [MK79] on the stadium billiard (Figure 4.1). The boundary conditions are just like those of a stadium or racetrack: two half circles joined by two straight line segments of length l . For $l = 0$ the stadium is a circle; L_z (angular momentum in the z direction) and energy are conserved, so the system is integrable. However, for any finite l the motion is chaotic. To see this, imagine an ensemble of billiard balls with the same velocity and nearly the same position hitting the circular boundary. The boundary will defocus the beam (Figure 4.2), and so there is instability with respect to initial

conditions, i.e., chaos. McDonald and Kaufman found level repulsion for finite l , and level clustering for $l = 0$ in accordance with the predictions of Berry and Tabor [BT77]. They also calculated the eigenstates and found that they appeared isotropic in k (momentum) space, i.e., $\langle \Psi | k \rangle$ is a Gaussian random variable (Figure 4.3). This is the GOE prediction (3.5.1), but was motivated at that time by Berry's work [Be77].

Similar work on the stadium was also done by Casati, Valz-Gris, and Guarneri [CVG80] and on Sinai's billiards (Figure 4.2) by Berry [Be81] showing agreement with GOE predictions. However, in these early works, the number of levels used was quite small, and the only spectral measure calculated was $P(s)$.

The strong connection between quantum chaos and GOE was made by Bohigas, Giannoni, and Schmidt [BGS84], and was inspired by the then recent success of GOE in describing the nuclear level fluctuations [HPB82]. In their work they examined the fluctuations of the eigenvalues of Sinai's billiards, i.e., billiards in a square box with a circular bumper in the center of radius R (Figure 4.2). They were able to obtain better statistics than previous works by combining the spectra for four different values of R to make one long run of levels. To avoid combining eigenvalues from different symmetry classes, which would give Poisson statistics, they actually solved the problem of the triangular Sinai's billiard, i.e., one eighth of the original billiard (Figure 4.1) which has no discrete parity-like symmetry. The levels were easily unfolded using the Weyl formula [BH76]:

$$\overline{N}(E) = \frac{\pi}{4} \left(SE - L\sqrt{E} + K \right) ,$$

where S is the area and L is the perimeter of the billiards and K is a constant. Because they had 740 levels, they were able to look at correlations between spacings by calculating the spectral average of Δ_3 - correlations cannot be judged by the nearest neighbor spacing $P(s)$. They also analyzed the fluctuations of the first 810 levels of the desymmetrized stadium. Figure 4.4 shows the results for both billiards which are in excellent agreement with GOE predictions.

In addition, they looked at these two statistics for the circular billiard, and for the stadium when the symmetries were mixed. (Figure 4.5) In both cases they found results closer to Poisson. Since the circular billiard is integrable, Poisson statistics were expected. They conjectured that the results were not exactly Poisson in this case because they had not yet reached the asymptotic (high) energy regime, i.e., in terms of the discussion at the end of §3.2, the number of superimposed spectra was not large enough for the theorem to apply.

This success, together with the agreement of the Nuclear Data Ensemble with GOE, prompted them to conjecture that “Spectra of time-reversal-invariant systems whose classical analogs are K systems show the same fluctuation properties as predicted by GOE”, which, if proven true, would constitute “the universality of the laws of level fluctuations.” This is the challenge: to either prove or disprove this far-reaching proposition which has ramifications in every area of quantum physics.

4.2 Transitions from Regular to Irregular Spectra

As broad as the universality theory is, it still does not cover all possible Hamiltonian systems; just as there is a gap between classical integrable and K systems, there must also be a gap between Poisson and GOE fluctuation properties of the spectra for the corresponding quantum systems.

An investigation of this transition has been made by Seligman, Verbaarschot, and Zirnbauer [SVZ84,SVZ85]. They looked at a set of Hamiltonians of the form

$$H = \frac{1}{2}(p_1^2 + p_2^2) + \mathcal{V}_1(x_1) + \mathcal{V}_2(x_2) + \mathcal{V}_{12}(x_1 - x_2), \quad (4.2.1)$$

where

$$\mathcal{V}_i(x) \equiv V_i(\alpha_i x^2 + \beta_i x^4 + \gamma_i x^6),$$

thus describing two particles in a one-dimensional potential interacting via a local potential. If $V_{12} = 0$ the Hamiltonian is separable and, therefore, integrable. By varying the parameters, the Hamiltonian varies from integrable to chaotic. The

degree of chaos was measured by the chaotic volume (5.3.1), i.e., the fraction of points in phase space with a positive lyapunov exponent.

To parametrize the level fluctuations, they constructed new “banded” ensembles with joint probability density (recall 3.2.1)

$$P_\sigma(\{H_{ij}\}) = P_{\mathcal{N}}^{\text{GOE}}(\{H_{ij}\}) \times e^{-(i-j)^2/\sigma^2} . \quad (4.2.2)$$

The bandwidth depends on σ and allows for variation from Poisson statistics ($\sigma = 0$, bandwidth = 0) to GOE ($\sigma = \infty$, bandwidth = size of matrix). Fluctuations for these new ensembles were calculated using Monte Carlo methods, i.e., by constructing 250 160×160 matrices chosen from $P_\sigma(H)$ and calculating the ensemble averages $\overline{\Delta}_3(L, \sigma)$ and $P(s, \sigma)$.

These two statistics were then calculated for several values of the potential parameters corresponding to different classical dynamics. The $\Delta_3(L)$ results for each set of parameters were fit to the ensemble averages, thus determining a value of σ . Figure 4.6 shows the outcome. Both the $\Delta_3(L)$ and $P(S)$ results are fit quite well by the same value of σ , and the progression from chaotic to regular is smooth and monotonic.

Analytical results for $P(s)$ with arbitrary classical dynamics were calculated by Berry and Robnik [BR84]. They superimposed Poisson $P(s)$ for the regular regions with Wigner $P(s)$ for the chaotic regions, and weighted each by their Liouville measure, i.e., the fraction of phase space that they cover. The general results are given by

$$P(s) = \frac{1}{\rho} \frac{d^2}{ds^2} \left[e^{-\rho_1 s} \prod_{i=2}^n \operatorname{erfc} \left(\frac{\sqrt{\pi}}{2} \rho_i s \right) \right] , \quad (4.2.3)$$

where ρ_1 is the total measure of the regular regions in classical phase space (5.4.1), ρ_i is the measure of each of the $n - 1$ chaotic regions, and ρ is the total measure. This result holds only in the semiclassical limit, when the number of levels in any energy interval diverges. Figure 4.7 displays the results for different values of n and

ρ_1 . These results were extended to $\Delta_3(L)$ and $\Sigma^2(L)$ by Seligman and Verbaarschot [SV85].

In both of these studies, the important classical parameter was the volume of phase space occupied by regular and irregular trajectories. It was hoped that this was a universal parameter, corresponding to some parameter describing the quantum fluctuations (e.g., σ) such that there would be a one-to-one, universal (i.e., for all Hamiltonians) mapping between the two. This does not appear to be the case. One explanation of this failure is that the phase space is too complicated. Because KAM tori partition phase space when there are only two degrees of freedom, systems with the same chaotic volume may look very different, e.g., one may have one large chaotic region while the other has many smaller chaotic regions; given such a picture, it is hard to imagine that the correspondence between classical dynamics and quantum fluctuations is universal. There is still some hope that universality exists for systems with three or more degrees of freedom; in this case KAM tori don't partition phase space, and there is always just one chaotic region; there may be many regular regions, but two or more Poisson spectra superimposed give back a Poisson spectrum.

4.3 Semiclassical Results

Percival's conjecture [Pe73] concerning the difference between regular and irregular spectra was based on semiclassical considerations. Since that time there has been considerable work concerning spectral fluctuations using semiclassical methods; these have supported the universality theory and sometimes gone beyond what RMT can offer. For example, Pechukas was able to confirm level repulsion [Pe83] for irregular spectra from very general considerations. Another example, one that we will be looking at in this section, is a recent result of Berry concerning the Δ_3 statistic and the deviation of results from RMT predictions. [Be85].

This work of Berry's, and many others, is built on a result of Gutzwiller [Gu69] that expresses the eigenvalues in terms of the action of classical periodic trajectories. The derivation spanned many papers, we will only motivate the results. The

quantum Green's function $G(q'', q', t)$ - the amplitude to get from q' to q'' in time t - may be written as a path integral

$$G(q'', q', t) = \langle q'' | e^{-iHt} | q' \rangle = \int \mathcal{D}[q] \mathcal{D}[p] e^{iS(p,q)/\hbar}, \quad (4.3.1)$$

where

$$S(p, q) \equiv \int_0^T [p\dot{q} - H(p, q)] dt,$$

and $q(0) = q'$ and $q(T) = q''$. The Fourier transform of the Green's function is written

$$G(q'', q', E) = \sum_j \frac{\phi_j(q'') \phi_j^*(q')}{E - E_j},$$

where ϕ_j and E_j are the eigenvalues and eigenvectors of the Hamiltonian. Taking the trace of the Green's function, we obtain

$$\int d^3q G(q, q, E) = \sum_j (E - E_j)^{-1}.$$

Using results from complex analysis, we write the discontinuity of $G \equiv DG$ across the real energy axis

$$\int d^3q DG(q, q, E) = -2\pi i \sum_j \delta(E - E_j).$$

Therefore the trace of the discontinuity of the Green's function is related to the density of states.

To evaluate this trace, we make use of semiclassical approximation and the stationary phase approximation (SPA) to rewrite the the right hand side of 4.3.1. Taking the Fourier transform and the trace, we obtain

$$\int d^3q G(q, q, E) = -\frac{1}{\hbar} \sum_{\text{periodic trajectories}} \oint d\bar{q} F(S) \exp i \left(\frac{S(E)}{\hbar} - \text{phases} \right),$$

where \bar{q} is the variable along the trajectory, $F(S)$ is a function of derivatives of the action, and the phases come from details of the SPA which will not concern

us. Only periodic paths contribute because we set $q(0) = q(T)$, and because SPA restrains $p(0) = p(T)$.

Berry builds on this result to write the density of states

$$\rho(E) = \rho_{\text{ave}}(E) + \rho_{\text{osc}}(E) , \quad (4.3.2)$$

where

$$\rho_{\text{osc}}(E) = \sum_j A_j(E) \exp [iS_j(E)/\hbar] , \quad (4.3.3)$$

and j labels the periodic trajectories. All the uninteresting (for our discussion) energy dependence is hidden in the amplitudes A_j . The action is now

$$S_j(E) = m \left[\oint \vec{p} \cdot d\vec{q} + \text{phases} \right] ,$$

where the phases are the same as in the preceding paragraph, and m indicates multiple traversals of the same path. The contribution of no traversals gives $\rho_{\text{ave}}(E)$, and is equivalent to the Weyl semiclassical density (5.4.1).

Using these ideas, Berry determines $\Delta_3(L)$ for both regular and irregular spectra. By this method, he can explain the “kink” seen in the result of Seligman *et al.* (Figure 4.6), i.e., the bending over of $\Delta_3(L)$ at large L . This phenomenon is not particular to their Hamiltonian, but could not be explained by RMT.

He begins with 4.3.2-3 for the density of states. In the semiclassical limit, the energy range L is classically small, and he writes S_j in a Taylor expansion:

$$S_j(E + \eta) \approx S_j(E) + \eta T_j(E)$$

where T_j is the period of the j th periodic orbit. Assuming that $A_j(E)$ and $\rho_{\text{ave}}(E)$ are constant over L , the density of states (4.3.2) may be integrated to yield $N(E + \eta) =$ the number of states with energy less than $E + \eta$. This in turn may be plugged into the equation for Δ_3 (3.4.5). The integration variable is now η , and the η dependence is simple and explicit, so the integral is easily done. The result is

$$\Delta_3(L) = \int_0^\infty dT \phi(T) G \left(\frac{LT}{2\hbar\rho_{\text{ave}}} \right)$$

where all the A_j and S_j dependence is hidden in $\phi(T)$. $G(y)$ is called the “orbit selection function”: $G(y = 0) = 0$ and slowly rises to $G(y \geq \pi) \approx 1$, therefore, orbits with $T_j < \hbar\rho_{\text{ave}}/L$ don’t contribute to Δ_3 . Intuitively, this is because the action of these orbits doesn’t vary much over L , and therefore this path contributes to the smooth background, and not to the oscillations about the background. However, if $T_j > \hbar\rho_{\text{ave}}/L$, S_j changes significantly in the interval L , this gives deviations from the smooth behavior, and therefore that orbit contributes to Δ_3 .

Let T_{min} be the period of the shortest orbit. If

$$L \geq L_{\text{max}} \equiv \frac{\hbar\rho_{\text{ave}}}{T_{\text{min}}}, \quad (4.3.4)$$

all periodic orbits contribute to $\Delta_3(L)$ by the above argument. If L is increased further, $\Delta_3(L)$ remains same since the number of contributing orbits is the same. The kink is this saturation of the Δ_3 statistic.

For $L \ll L_{\text{max}}$, Berry proves the Poisson result for regular spectra, and the GOE result for irregular spectra. The difference in statistics for different dynamics arises because periodic orbits in regular systems are stable and occur in families, while for irregular systems they are isolated and unstable (in general). This distinction is manifested in different functional forms for $\phi(T)$. The saturation value of $\Delta_3(L)$ depends on the amplitudes and actions, and can be calculated only in the simplest cases. Figure 4.8 shows Berry’s analytical prediction for (regular) square billiards, compared with numerical results of Casati *et al.* The agreement is excellent.

The semiclassical methods have yielded impressive results in agreement with numerical experiments, and in agreement with RMT. However, it should be noted that most of the proofs are not rigorous, and not completely general. For example, canonical momentum dependence is assumed. This is important consideration for our work because the momentum dependence of the classical LMG model is quartic (5.2.5).

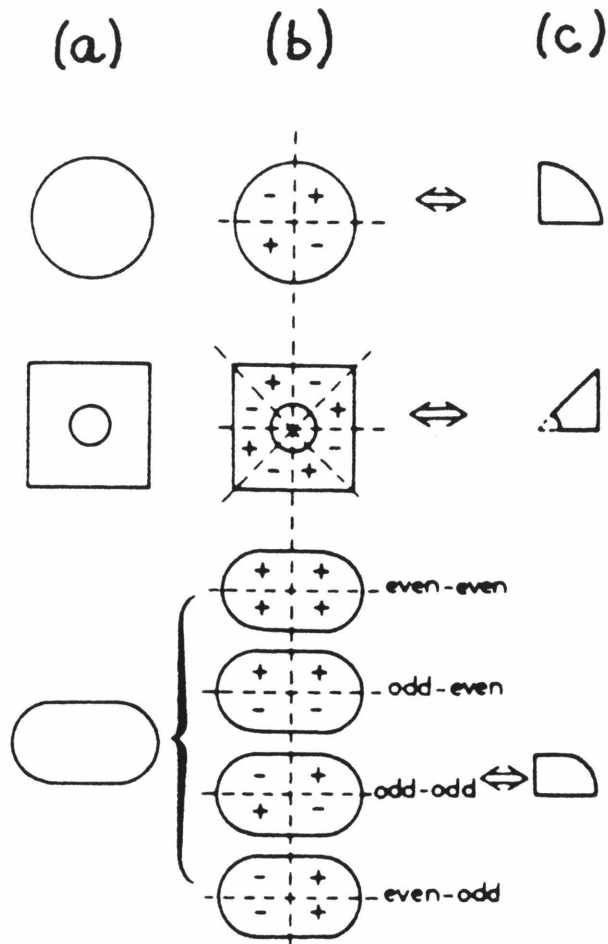


Figure 4.1 Three kinds of billiards: circular, Sinai's, and stadium. Column *a* shows the hard walls of each billiard table; column *b*, the different discrete symmetries of each system which must be treated separately; column *c*, the desymmetrized versions of each billiard, i.e., those for which we no longer need to worry about symmetries. [BG84]

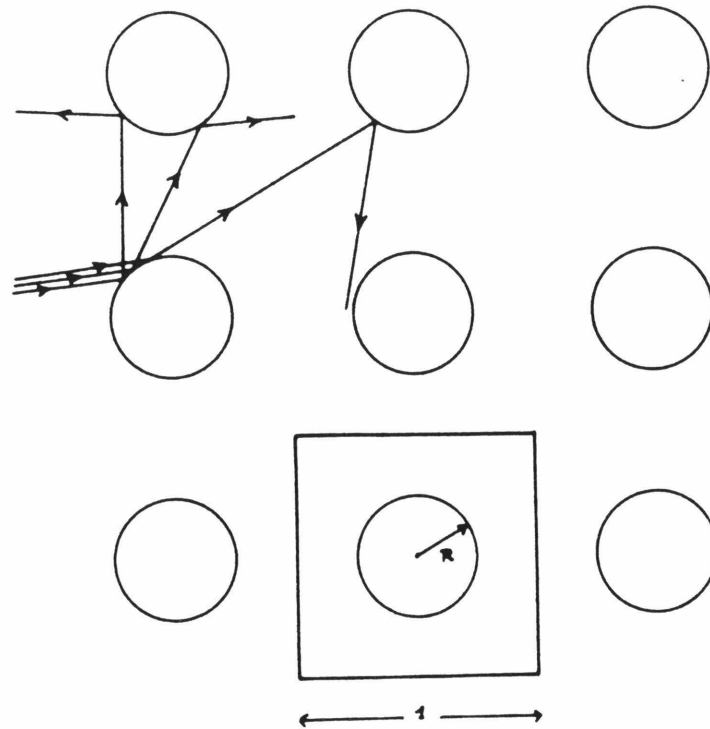


Figure 4.2 Sinai's billiards is an infinite table with infinitely many equally spaced circular bumpers. From symmetry arguments, this reduces to one bumper in a square box. This system is classically chaotic; the "beam" of particles is quickly defocused, indicating sensitive dependence on initial conditions. [BG84] This same defocusing often occurs when the boundaries are curved, as in stadium billiards.

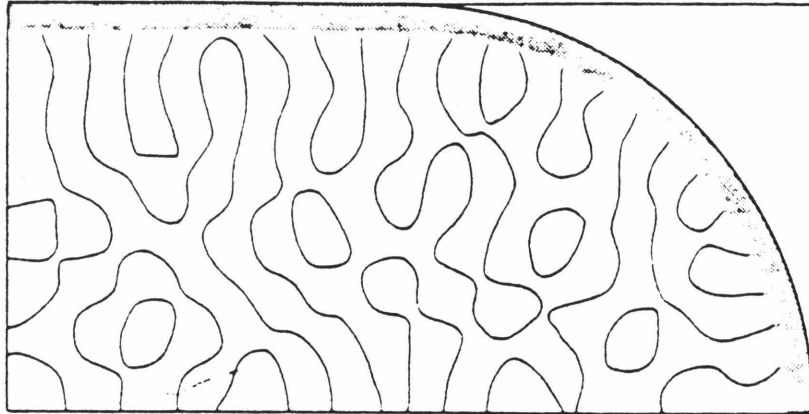


Figure 4.3 Nodes ($\Psi(x, y) = 0$) of the stadium billiards. The orientation of the nodes is quite random, giving evidence that $\langle \Psi | k \rangle$ is a Gaussian random variable. [MK79] Note that $|k|^2 = \text{energy}$ is constant, as indicated by the constant internode spacing.

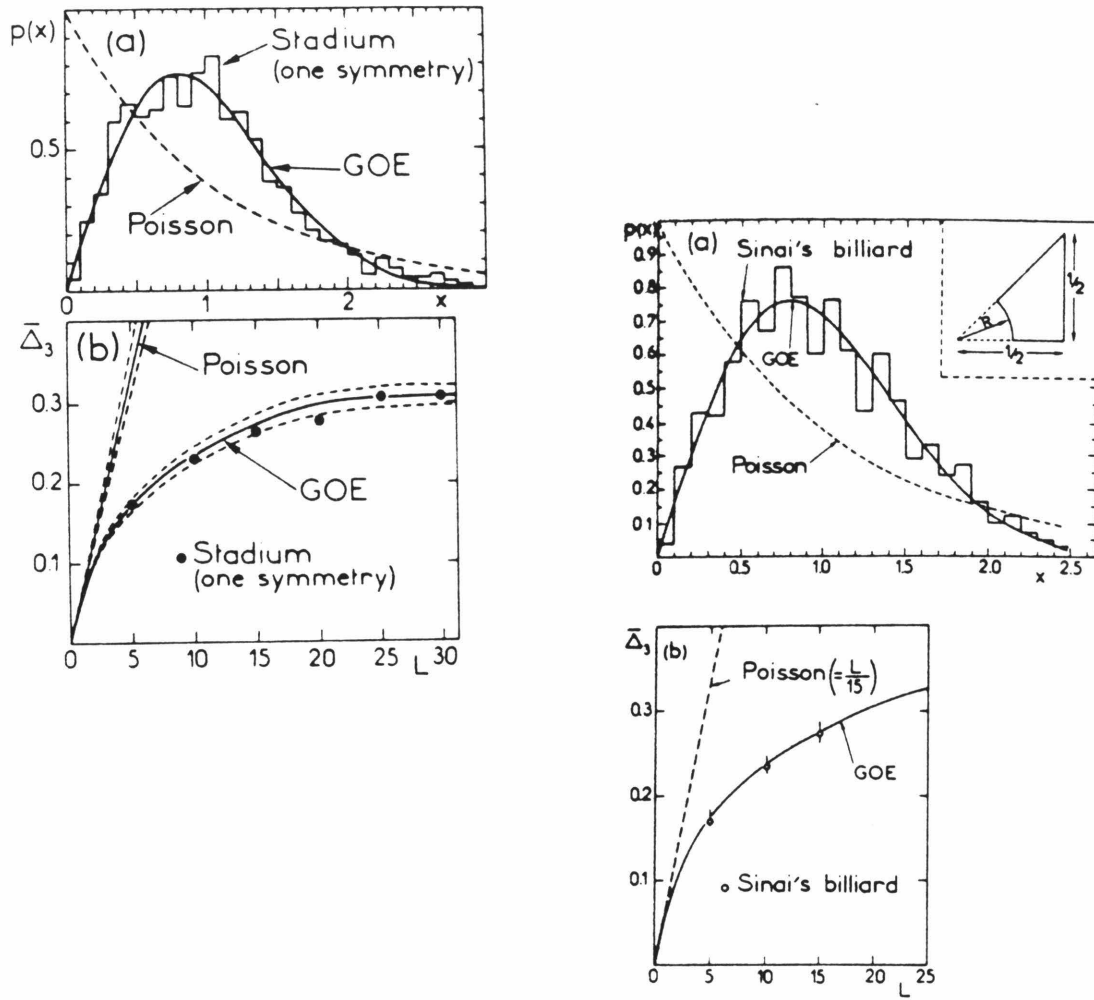


Figure 4.4 Spectral fluctuations for the desymmetrized (Figure 4.2) stadium and Sinai's billiards with 810 and 740 levels each. The results are in excellent agreement with GOE predictions, and quite far from Poisson. [BG84]

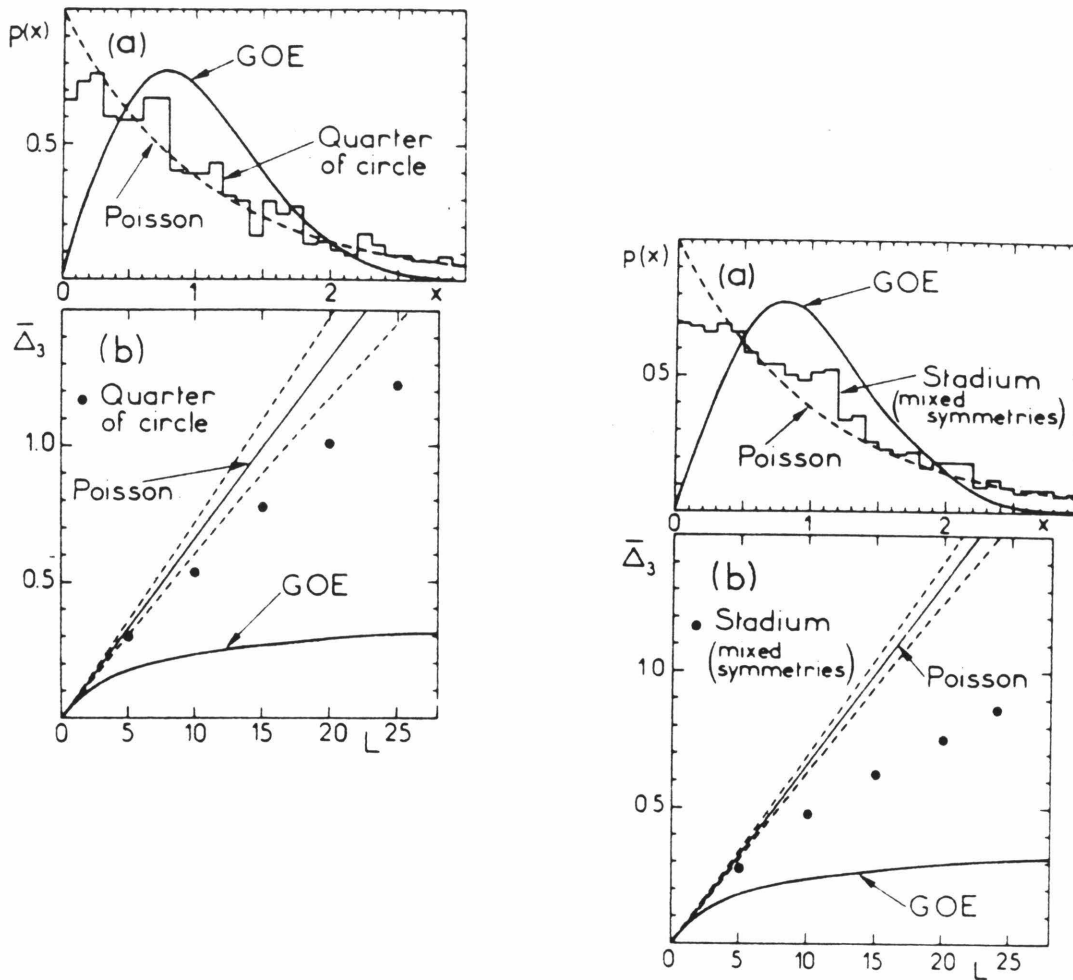


Figure 4.5 Spectral fluctuations for the integrable circular billiards and for the stadium billiard with mixed symmetries. Both are expected to give Poisson statistics in accordance with the superposition theorem (§3.2), but do not. In both cases, this is probably because the number of superimposed spectra is not large enough: for the stadium there are only four spectra; for the integrable circular billiards, the higher the energy the more superimposed spectra coexist, so increasing the energy should increase the agreement with Poisson. [BG84]

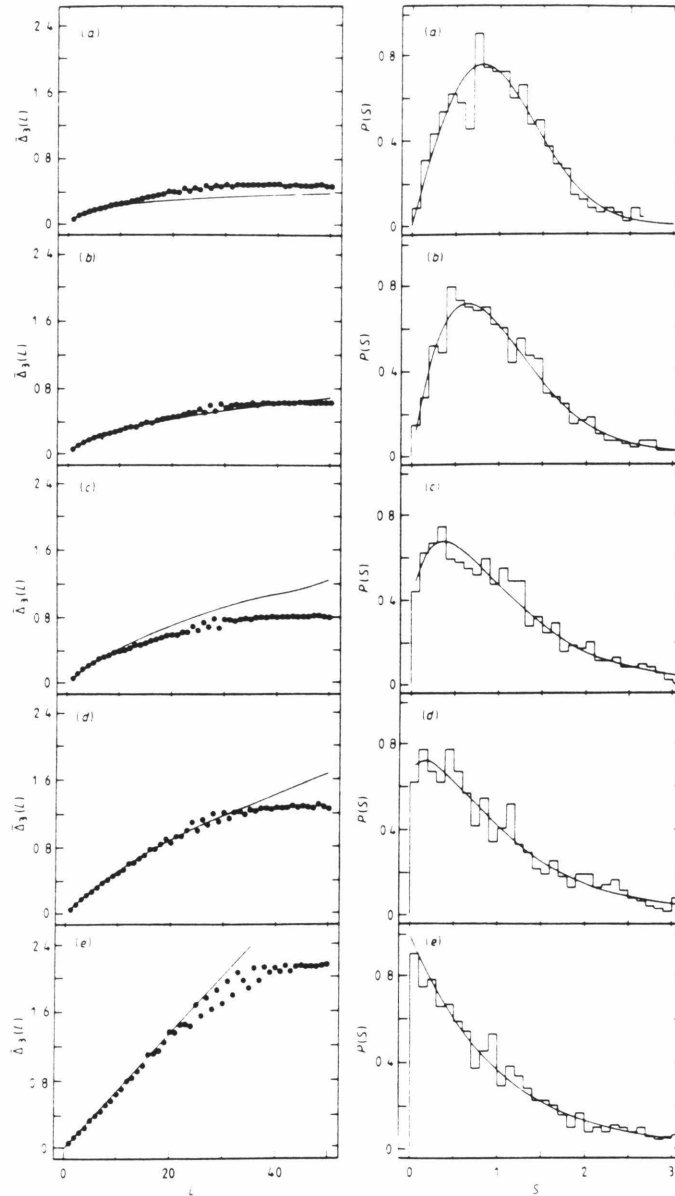


Figure 4.6 Smooth transition of spectral statistics from GOE to Poisson as the classical analog of the Hamiltonian 4.2.1 varies from irregular to regular. The chaotic volume is (from top to bottom) ≈ 1.0 , ≈ 1.0 , ≈ 0.99 , ≈ 0.79 , and 0.0 . The smooth curves are from ensemble averages of “banded” GOE matrices (4.2.2). [SVZ84] The kink, i.e., the deviation from prediction at large L , is explained in §4.3.

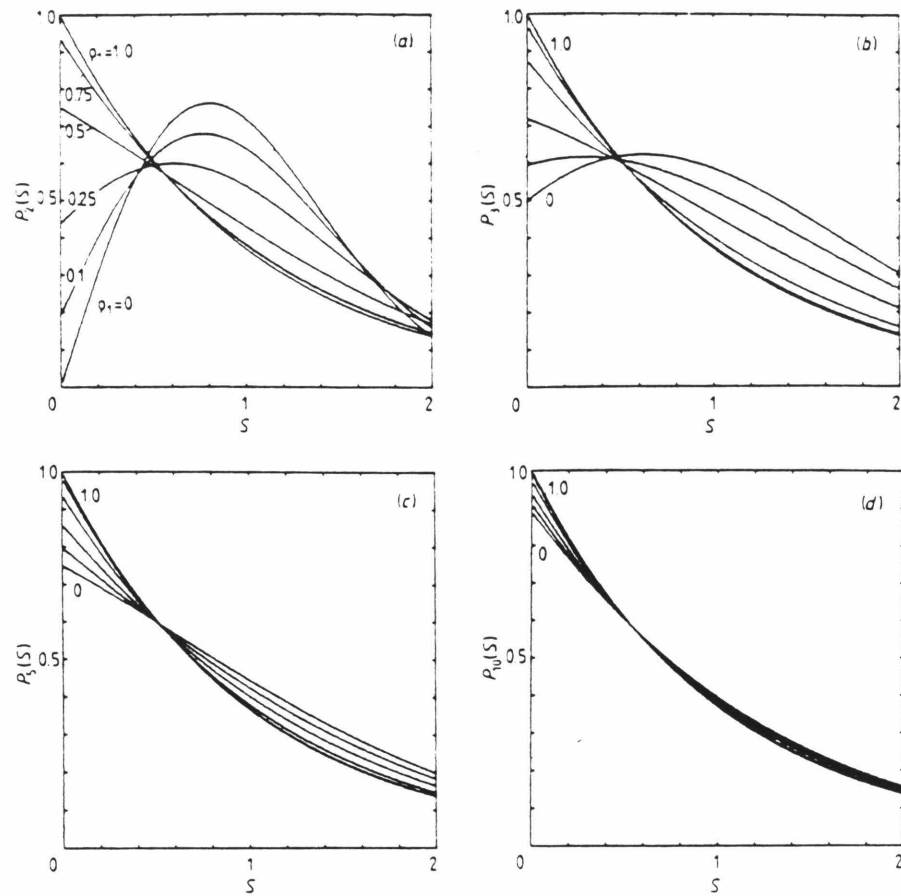


Figure 4.7 Analytical results for the next nearest neighbor spacing when the phase space has both regular and irregular regions [BR84]. $P_n(s)$ is the result when there are $n - 1$ chaotic regions of equal size; the four graphs are for $n = 2, 3, 5, 10$. The size of the regular region is ρ_1 , and results are shown for $\rho_1 = 1.0, 0.75, 0.5, 0.25, 0.1$ and 0.0 .

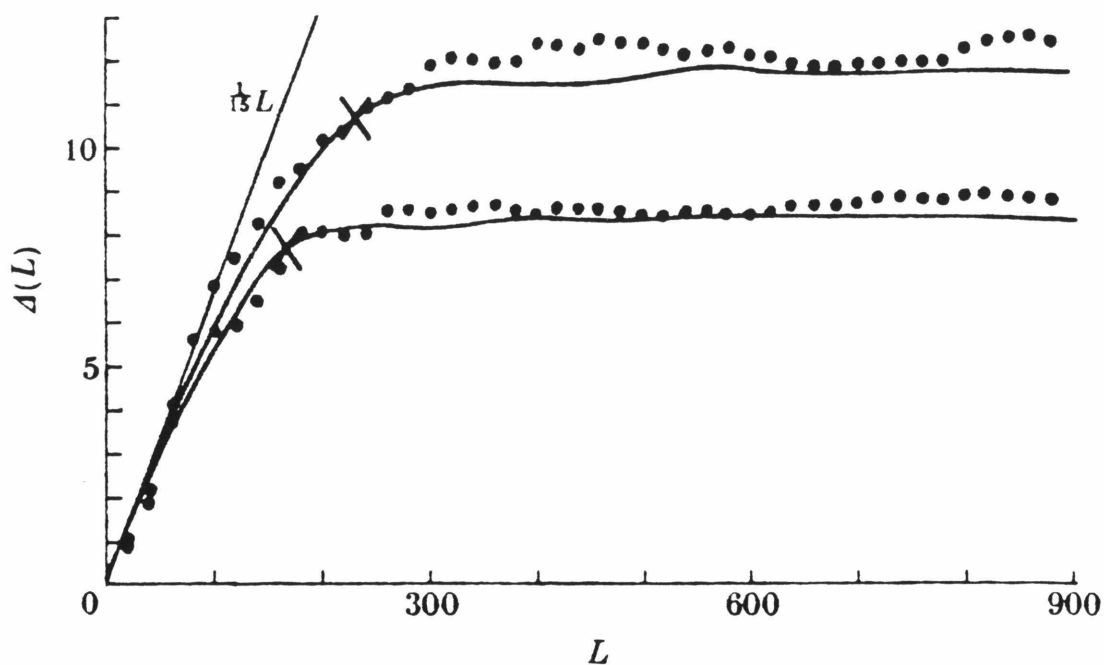


Figure 4.8 Analytical and numerical results for $\Delta_3(L)$ of the square billiard showing the kink. The dots are numerical work from Casati, Chirikov and Guarneri [CCG85], the solid lines are the prediction of Berry [Be85]. The crosses indicate L_{\max} , and the two curves are for two different energy ranges. Note that there is an L region (about $L = [100, 200]$) where Δ_3 has neither reached its saturation value, nor does it agree with the Poisson result. Rectangular billiards are integrable because $|v_x|^2$ and $|v_y|^2$ are both conserved.

Chapter Five

Three Level Lipkin-Meshkov-Glick Model

We have the foundation for our investigation: predictions about eigenvalue and eigenvector fluctuations, and the quantitative tools to test those predictions. Now we add the essential ingredient: a quantum Hamiltonian system. In this chapter, we will introduce the Lipkin model in the context of nuclear physics, derive the classical limit, examine the degree of chaos in this limit, diagonalize the Hamiltonian, and examine spectral and strength fluctuations with reference to the corresponding classical dynamics.

5.1 Motivations

Nuclear physics is a complicated business. Calculations of a nuclear ground state, for example, involve a many-body Hamiltonian and an interaction that is known only approximately. A first attempt at describing the ground state involves the mean field approximation, which asserts that the individual nucleons move in a fixed potential due to all the other nucleons. This allows the substitution of a simpler one-body problem for the original many-body problem. Solving the Hamiltonian with a one-body phenomenological mean field potential, we obtain a set of single particle energy levels. We make the nuclear ground state by placing the desired number of nucleons in the lowest energy levels, filling up each according to its spin and isospin degeneracy.

The single particle levels obtained above are grouped into shells, where the intershell energy separation is significantly larger than the intrashell separations. This structure was put in “by hand” to obtain the experimentally observed properties (e.g., unusually large single particle binding energies) of nuclei with magic numbers

(2, 8, 28, 50, 82) of neutrons and/or protons. Those nucleons outside the last closed shell are valence nucleons.

Improvements may be made on this extreme single particle model; the first is configuration mixing. This allows the particles to be in single particle states other than the lowest unoccupied energy states, or selects a ground state when there are several lowest configurations, i.e., when there is degeneracy. In this procedure the filled shells are treated as an inert core, and only the valence nucleons are involved in the mixing. The perturbation which causes the mixing is the residual interaction, viz., the difference between a realistic nuclear two-body interaction and the one-body mean field.

But the core is not really inert. Hartree-Fock calculations take the next step in sophistication by allowing all the single particle wavefunctions to vary. These calculations assume that the wavefunction is a Slater determinant of single particle wavefunctions, the best wavefunction is calculated by demanding that it minimize the energy. Here the potential is not phenomenological, but is determined in a self-consistent manner and is built upon a realistic nuclear interaction. Excitations from the Hartree-Fock ground state are made by the Random Phase Approximation (RPA) which describes low lying collective vibrations.

The Lipkin-Meshkov-Glick model [LMG65] was introduced in an effort to check the validity of approximate techniques of nuclear physics, including the above mentioned RPA. To provide a somewhat realistic check, they chose a nontrivial model which is analytically soluble in a few simple cases, and which mimics the shell model picture of the nucleus.

The model has M distinguishable fermions which are distributed among three energy levels, each of which is M -fold degenerate. (The original model had only two levels, it will become clear later why this model was inappropriate for our purposes.) The single particle states are labeled by two numbers: $k = 0, 1, 2$ for the ground, first, and second excited states; and $m = 1, 2, 3, \dots, M$ for the degenerate

states within each level. (Figure 5.1) We may consider these as three single particle levels, at energy ϵ_k , with the same angular momentum j and, therefore, the same degeneracy. In this picture, m labels the $2j + 1$ different values for the z component of angular momentum. The interaction moves a pair of particles from one level to another, without changing either m quantum number. This may be interpreted as a monopole-monopole interaction between two levels, conserving j and m .

The Hamiltonian is written in the language of second quantization using fermionic creation and annihilation operators which obey the usual anticommutation relations:

$$\begin{aligned} \{a_{kn}, a_{im}\} &= 0 & \{a_{kn}^\dagger, a_{im}^\dagger\} &= 0 \\ \{a_{kn}, a_{im}^\dagger\} &= \delta_{ki}\delta_{nm} . \end{aligned}$$

In this notation the Hamiltonian is written:

$$H = \sum_{k=0}^2 \epsilon_k \left(\sum_{m=1}^M a_{km}^\dagger a_{km} \right) - \frac{1}{2} \sum_{k,l=0}^2 V_{kl} \left(\sum_{m=1}^M a_{km}^\dagger a_{lm} \right)^2 . \quad (5.1.1)$$

In all of our calculations we take a symmetric distribution of the levels about zero: $\epsilon_2 = -\epsilon_0 \equiv \epsilon$, $\epsilon_1 = 0$. We also chose $V_{kl} \equiv V(1 - \delta_{kl})$. Energies will be quoted in units of $M\epsilon$, and we define the dimensionless coupling constant $\chi \equiv MV/\epsilon$.

Because each particle may occupy one of three states, regardless of the location of any other particle, there are a total of 3^M states. Therefore, the Hamiltonian may be written in a compact basis. This makes the quantum calculations straightforward since we don't have to worry about errors introduced by truncating the basis, but it also makes the LMG model qualitatively different from previously studied systems.

Yet for any reasonable M , this makes for quite a large basis, and the problem does not seem at all tractable. For M as small as eight, the size of the basis $\equiv \mathcal{N} = 6561$. However, by design of the authors, there are symmetries which may be exploited to ease the calculations. The nine bifermion operators

$$G_{kl} \equiv \sum_{m=1}^M a_{km}^\dagger a_{lm} \quad (5.1.2)$$

are generators of the $U(3)$ group. With number conservation $M = \sum_{k=0}^2 G_{kk} =$ constant, the group becomes $SU(3)$. The Hamiltonian may be written in terms of these operators

$$H = \sum_{k=0}^2 \epsilon_k G_{kk} - \frac{1}{2} \sum_{k,l=0}^2 V(1 - \delta_{kl}) G_{kl}^2,$$

so the Casimir invariants of the group commute with the Hamiltonian. We may sidestep the group theory, and appeal to intuition to see the consequences of this. Consider the collective states: those states which treat all M particles the same, i.e., are symmetric under the interchange of any two particles. The Hamiltonian clearly connects only these collective states with other such states since the generators are collective operators. These are the states which we will use in the quantum calculations.

This has reduced the size of the problem considerably. Now $\mathcal{N} = (M+2)(M+1)/2$; this equals the number of ways there are to put M particles in three levels when order doesn't matter. This reduces the $M=8$ basis to 45. But, there is yet one more symmetry. The interaction moves only *pairs* of particles, so the oddness or evenness of the population in each level (which we shall refer to as the signature) is conserved by H . Therefore there are four different matrices for each value of M . These will be identified by $s_0 s_1 s_2$, the signature of each level. For M even these matrices will be referred to as eee , eoo , ooe , and oeo ; for M odd, the possibilities are ooo , oeo , eeo , and oeo .

We calculate the sizes of these matrices again by permutation arguments. These are

$$\begin{aligned} \mathcal{N}_{ooo} &= \frac{(M+1)(M-1)}{8} \\ \mathcal{N}_{eoo} = \mathcal{N}_{oeo} = \mathcal{N}_{ooe} &= \frac{M(M+2)}{8} \\ \mathcal{N}_{oeo} = \mathcal{N}_{eeo} = \mathcal{N}_{eoo} &= \frac{(M+1)(M+3)}{8} \\ \mathcal{N}_{eee} &= \frac{(M+2)(M+4)}{8}. \end{aligned}$$

\mathcal{N}_{ooo} equals the number of ways $(M - 3)/2$ things may be put in three levels, order not mattering. The “things” in this case are pairs of particles. Three particles are taken out because each level must always have at least one occupant. Similar arguments provide the size of the other signature classes. For the $M = 8$ basis, $\mathcal{N}_{eee} = 15$ and $\mathcal{N}_{eoo} = \mathcal{N}_{ooe} = \mathcal{N}_{oeo} = 10$.

Returning for a minute to nuclear physics considerations, we may appreciate the richness of the LMG model. In our collective basis, we have one state with single particle excitation to the first level and one with single particle excitation to the second level; these are not coupled by the interaction since they are from different signature classes. Thus the basis states satisfy the Hartree-Fock equations which require that the single particle Hamiltonian be diagonal in single particle excitations [RS80]. However, the interaction does mix different configurations (states with different numbers of particles in the excited levels) and thus allows for ground state correlations. The collective states which we have chosen to examine are just those states which we expect to generate the interesting behavior in nuclei. It is these states that are strong enough to significantly perturb the ground state energy which is obtained from the simple shell model. In these ways the LMG mimics what we really believe is happening in nuclei.

5.2 Classical Limit

To apply the hypothesis of universality of level fluctuations requires knowledge of the classical dynamics; we need to determine if there are values of the coupling strength that give rise to chaotic behavior. To answer this question we must first find the classical Hamiltonian and canonical variables.

Finding a classical limit means finding a limit in which the quantum equations of motion become the classical equations of motion, e.g., when the commutator becomes the Poisson bracket:

$$\frac{\partial A}{\partial t} = \frac{i}{\hbar} \langle A, H \rangle \rightarrow \{A, H\}.$$

In textbooks this is usually the $\hbar \rightarrow 0$ limit, or the limit of large quantum numbers. More precisely this is when the Compton wavelength $= 2\pi\hbar/p$ (the quantum length scale) is much smaller than the length scales in the problem (e.g. typical length over which the potential is nearly constant). In this case the quantum fluctuations are small and may be ignored. However, in the LMG model there are no length or mass scales which can vary.

Instead, we take the thermodynamic limit: M (the number of particles in the system) $\rightarrow \infty$, while $\chi = MV/\epsilon$ (the normalized strength of the residual interaction) remains fixed. In what sense is this a classical limit? When the number of particles is large, the collective behavior with all the particles doing the same thing is the behavior of a macroscopic body, and for macroscopic bodies classical mechanics gives the correct dynamics. For example, the collective motion of nucleons in a nucleus has been successfully modeled by the classical motion of a liquid drop.

To obtain the classical limit, we will define an overcomplete set of coherent states, look at the quantum propagator sandwiched between two such states, change this to a path integral, take the stationary path approximation which is valid in the large M limit, and thereby obtain classical equations of motion. What we show is the application of much more general techniques [Ka79, Sh80, WK82, Ya82, vR82] to our particular model.

We begin with the coherent states; these are the natural choice for describing collective, classical behavior [Ya82]. In the large M limit matrix elements of operators between different states are zero, therefore, quantum interference effects disappear. Also, expectation values of operators factorize

$$\langle AB \rangle \rightarrow \langle A \rangle \langle B \rangle ,$$

giving (for $A = B$)

$$\langle \Delta A \rangle = \langle A^2 - \langle A \rangle^2 \rangle \rightarrow 0 \tag{5.2.1}$$

zero uncertainty in the value for any operator. With this choice of states we will describe only collective behavior, but this is exactly the behavior that dominates

in the classical limit. Note that this choice is consistent with our choice for the quantum basis; there we also chose the basis which described collective behavior.

To define the coherent states we continue using the second quantized notation of §5.1. The non-interacting ground state with all M particles in the ground level is denoted by $|0\rangle$. The states are parametrized by two complex numbers z_1 and z_2

$$|\Phi(z)\rangle \equiv \exp(z_1 G_{10} + z_2 G_{20})|0\rangle, \quad (5.2.2)$$

where the collective operators are defined in equation 5.1.2. G_{10} collectively raises particles from the ground to the first level, G_{20} raises them from the ground to the second. Here z represents the two complex numbers z_1 and z_2 , each of which depends on time.

The normalization of these states is given by A.1

$$\langle\Phi(z)|\Phi(z)\rangle = (1 + |z_1|^2 + |z_2|^2)^M.$$

(The Appendix gives details of this and other coherent state calculations.) These states obey the completeness relation (A.4):

$$\int (M+1)(M+2) \frac{|\Phi(z)\rangle\langle\Phi(z)|}{(2\pi)^2} \frac{dz_1 dz_1^* dz_2 dz_2^*}{(1 + |z_1|^2 + |z_2|^2)^{M+3}} = 1.$$

Because the wavefunctions are not normalized and the measure is not unity, this is not the most convenient parametrization of the the states. Instead, we will work with the normalized states

$$|\Psi(z)\rangle \equiv \frac{|\Phi(z)\rangle}{\sqrt{\langle\Phi(z)|\Phi(z)\rangle}},$$

and will change to the variables

$$\beta_j \equiv \frac{z_j}{(1 + |z_1|^2 + |z_2|^2)^{1/2}} \quad j = 1, 2.$$

Now the completeness relation reads

$$\int (M+1)(M+2) \frac{|\Psi(\beta)\rangle\langle\Psi(\beta)|}{(2\pi)^2} d\beta_1 d\beta_1^* d\beta_2 d\beta_2^* = 1. \quad (5.2.3)$$

At this point we introduce quantum time evolution with the propagator and the time evolved coherent state $\Psi(t)$

$$|\Psi(t)\rangle = e^{-iH(t_f-t_i)}|\Psi(\beta_0)\rangle .$$

The overlap between an arbitrary final coherent state and our time evolved initial state is given by

$$\langle\Psi(\beta_L)|e^{-iH(t_f-t_i)}|\Psi(\beta_0)\rangle .$$

where β_0 and β_L denote two different sets of β values. To evaluate this integral, we will follow the standard path integral approach [BO80,vR82] by rewriting the exponential

$$\exp[-iH(t_f - t_i)] = \exp\left[-i\sum_{l=1}^L H\eta\right] = \prod_{l=1}^L \exp[-i\eta H] ,$$

where

$$\eta \equiv \frac{(t_f - t_i)}{L}, \quad L \rightarrow \infty .$$

Between each term in this product of exponentials, we insert unity in the form of the completeness relation of coherent states (5.2.3). We now have L terms of the form

$$\langle\Psi(\beta_{l+1})|e^{-i\eta H}|\Psi(\beta_l)\rangle .$$

To first order in η each of these terms may be rewritten

$$\exp\left[i\eta\langle\Psi(\beta_l)|i\frac{\partial}{\partial t} - H|\Psi(\beta_l)\rangle\right] ,$$

where we have assumed the continuity of $\Psi(\beta_l(t))$ in time. The final expression for the overlap is given by

$$\int_{\beta_0}^{\beta_L} \mathcal{D}(\beta) e^{iMS(\beta)} .$$

where $\mathcal{D}(\beta)$ indicates an integration over all paths, and the action S is defined by

$$S(\beta) \equiv \frac{1}{M} \int_{t_i}^{t_f} \langle\Psi(\beta(t))|i\frac{\partial}{\partial t} - H|\Psi(\beta(t))\rangle .$$

The action is independent of M . (See the Appendix.)

Because the phase in the path integral is proportional to M , we are justified in using the stationary phase approximation to evaluate the integral in the thermodynamic limit. In this limit the only paths which will contribute are the ones for which the action integral is stationary; the contributions from all other paths will vanish because of the rapid oscillations of the exponential as S varies. To determine the functional dependence of the β 's on time, we perform a variational calculation by demanding that

$$\partial S = 0$$

which gives

$$\frac{\partial \langle H/M \rangle}{\partial \beta} = \frac{i}{M} \sum_{\alpha} \dot{\alpha} \left[\frac{\partial}{\partial \alpha} \langle \Psi | \Psi_{\beta} \rangle - \frac{\partial}{\partial \beta} \langle \Psi | \Psi_{\alpha} \rangle \right], \quad (5.2.4)$$

where

$$|\Psi_{\alpha}\rangle \equiv \frac{\partial}{\partial \alpha} |\Psi\rangle,$$

α runs over all four values $\beta_1, \beta_1^*, \beta_2, \beta_2^*$, and the β dependence in Ψ has been suppressed. These are beginning to look like classical equations of motion. Kan [Ka81] gives a general method for finding new variables to make these equations of motion for the parameters of the canonical form. However, we have already chosen the correct variables. To see this, note that

$$\langle \Psi | \Psi_{\beta_j} \rangle = \frac{M}{2} \beta_j^* \quad \langle \Psi | \Psi_{\beta_j^*} \rangle = -\frac{M}{2} \beta_j.$$

Plugging these values into equation 5.2.4 we obtain

$$\frac{\partial \langle H/M \rangle}{\partial \beta_j} = i \dot{\beta}_j^* \quad \frac{\partial \langle H/M \rangle}{\partial \beta_j^*} = -i \dot{\beta}_j.$$

We may get rid of the noncanonical i dependence by one last change of variables:

$$\beta_j = \frac{q_j + ip_j}{\sqrt{2}} \quad \beta_j^* = \frac{q_j - ip_j}{\sqrt{2}}.$$

We may now identify p and q as canonical momentum and position variables for $H_{\text{class}} \equiv \langle \Psi(\beta) | H/M | \Psi(\beta) \rangle$.

The exact form of the classical Hamiltonian is easily derived from the expectation values of the coherent operators (A.2,A.3). In terms of the canonical variables

$$\begin{aligned} \frac{H_{\text{class}}(\vec{q}, \vec{p})}{\epsilon} = & -1 + \frac{1}{2}q_1^2(1 - \chi) + \frac{1}{2}q_2^2(2 - \chi) + \frac{1}{2}p_1^2(1 + \chi) + \frac{1}{2}p_2^2(2 + \chi) \\ & + \frac{1}{4}\chi[(q_1^2 + q_2^2)^2 - (p_1^2 + p_2^2)^2 - (q_1^2 - p_1^2)(q_2^2 - p_2^2) - 4q_1q_2p_1p_2]. \end{aligned} \quad (5.2.5)$$

Because of the unusual quartic momentum dependence, this is not a particle in a potential well.

The one free parameter is $\chi \equiv MV/\epsilon$, the normalized strength of the interaction. As χ varies, the topology of the “potential” surface varies; i.e., the surface given by $H(\vec{q}, \vec{p} = 0)$. Because of the quartic momentum dependence this surface does not have the standard meaning, but it is still informative. (Figure 5.2) The number and location of the minima vary with χ :

$$\begin{array}{llll} q_{10} = 0 & q_{20} = 0 & E_{\min} = -1 & \chi \leq 1 \\ q_{10}^2 = 1 - \frac{1}{\chi} & q_{20} = 0 & E_{\min} = -1 - \frac{(\chi - 1)^2}{4\chi} & 1 \leq \chi \leq 3 \\ q_{10}^2 = \frac{2}{3} & q_{20}^2 = \frac{2\chi - 6}{3\chi} & E_{\min} = \frac{-\chi}{3} - \frac{1}{\chi} & 3 \leq \chi \end{array} \quad (5.2.6)$$

At low energies, the motion will be small oscillations about the minima, and the system is near integrable.

We should make the connection between the quantum model and our new canonical variables:

$$p_j = -i \frac{\langle G_{0j} \rangle - \langle G_{j0} \rangle}{\sqrt{2M\langle G_{00} \rangle}} \quad q_j = \frac{\langle G_{0j} \rangle + \langle G_{j0} \rangle}{\sqrt{2M\langle G_{00} \rangle}}.$$

The p 's and q 's are related to the expectation values of the “normalized” raising and lowering operators. Twice the fraction of particles in the j th level is given by

$$2 \frac{\langle G_{jj} \rangle}{M} = p_j^2 + q_j^2.$$

Since the number of particles is conserved

$$r^2 \equiv p_1^2 + q_1^2 + p_2^2 + q_2^2 \leq 2 ,$$

the phase space for the classical Hamiltonian is compact. Looking at the equations of motion for r with $\epsilon \equiv 2 - r^2$ small, we find $\dot{r} \propto \epsilon$; a trajectory can never cross the surface at $r^2 = 2$.

Because the phase space is compact, the energy range is also finite. For $\chi = 0$ the maximum energy is 1 (in units of $M\epsilon$) for the state with all particles in level two. For $\chi = \infty$ the highest energy is about 25.5.

There are two degrees of freedom in this system, corresponding to the fraction of particles in levels one and two. If we had chosen the original two level LMG model, we would have had a system with one degree of freedom which is necessarily integrable; there would be no chaos and no opportunity to check the hypothesis of universality of level fluctuations. For this reason we chose the three level extension of the original model.

Finally, we examine the nature of H in two limits: $\chi = 0$ and $\chi = \infty$. In the first limit H is a two-dimensional coupled oscillator which is classically integrable, and the eigenvalues are trivial (5.4.1). In the $\chi = \infty$ limit the system is not integrable, but there is a new discrete symmetry: if we switch the subscripts of the p_j 's and q_j 's (i.e., $1 \leftrightarrow 2$) the Hamiltonian is unchanged. In the quantum system this corresponds to the energy degeneracy of the three single particle levels, and the consequent symmetry of H under interchange of level labels.

5.3 Chaos in the Classical Limit

We have the form of the classical Hamiltonian, but is it chaotic? For $\chi = 0$ the system is integrable. As χ increases, we'd expect the system to vary from integrable to chaotic. For a fixed value of χ , varying the energy will also change the nature of the dynamics, since near E_{\min} the motion is quasi-integrable. Therefore a thorough

search for chaos should be done in the energy- χ plane. Chaos exists if the system is ergodic and has a positive Lyapunov exponent (equation 2.4.2 and discussion at the end of §2.5). Real life restrictions demand that we look only at a few values of χ , and be satisfied with numerical evidence for ergodicity and chaos.

We chose four values of χ for the initial search: 0.75, 2, 10, 100 corresponding to one, two, four, and again four minima. We did not calculate Lyapunov exponents at first, but instead looked at surfaces of section. Ten to fifteen energies from the allowed energy range were examined for each χ . The equations of motion were integrated numerically using a fourth order Runge-Kutta algorithm. The step size was chosen to conserve energy to at least one part in a thousand. To obtain the points on the surfaces of section, we used a method due to Henon. Making a $p_2 - q_2$ surface of section, we trigger on $q_1 = q_{10}$, the equilibrium value of q_1 (5.2.4), and also require that $\dot{q}_1 \geq 0$. Because the momentum dependence of the energy is quartic, there may be two values of $-\sqrt{2} \leq p_1 \leq \sqrt{2}$ which satisfy the trigger conditions and conserve energy. Therefore, to uniquely specify p_1 , the trigger for the surface of section also requires that p_1 be the larger of the two values which conserve energy. When the trigger goes off, we integrate the equations of motion exactly back to the surface by changing the independent variable to q_1 and the step to $q_{10} - q_1$.

For $\chi = 0.75$ nothing but KAM tori appear at all energies; the system is close to integrable. For $\chi = 2$ and 10 there are KAM tori at all energies as well as chaotic regions in the middle of the spectrum. For $\chi = 100$ there is a large energy range (about -25 to 0) for which the motion is apparently totally chaotic. (Figure 5.28) We need a long energy range with completely chaotic dynamics (no KAM tori) so that we will have enough eigenvalues in the quantum system to do meaningful statistical analysis. For this reason, further investigations were limited to $\chi = 100$.

Although the surfaces of section give a good qualitative picture of the topology of phase space, we need a more quantitative test for chaos. We would like to prove ergodicity, which is necessary, but not sufficient for chaos. Then the calculation of

the Lyapunov exponent would tell all: a positive Lyapunov exponent would prove the system chaotic, while a zero exponent would prove that the system was not. But it is difficult to prove ergodicity analytically, and impossible to do so numerically. Simply watching a trajectory evolve in time may be misleading. It may stay confined to one small submanifold for the entire run of the program, but in truth it may only be trapped there for a long, but finite time. On the other hand, a trajectory may appear to wander over all phase space, while it may actually avoid small but finite areas.

In place of calculations of ergodicity, we calculate the chaotic volume [BGS76, SVZ84], i.e., the fraction of phase space for which the Lyapunov exponent is positive

$$\mu_c(E, \chi) \equiv \frac{\int dp_1 dq_1 dp_2 dq_2 \delta(E - H(\vec{q}, \vec{p}, \chi)) \Theta(\lambda(\vec{q}, \vec{p}))}{\int dp_1 dq_1 dp_2 dq_2 \delta(E - H(\vec{q}, \vec{p}, \chi))}, \quad (5.3.1)$$

where

$$\Theta(x) \equiv \begin{cases} 1 & x > 0 \\ 0 & x \leq 0. \end{cases}$$

In practice the delta function in energy is replaced by a product of two step functions

$$\delta(E - H(\vec{q}, \vec{p}, \chi)) \rightarrow \Theta((E + \Delta E) - H(\vec{q}, \vec{p}, \chi)) \Theta(-(E - \Delta E) + H(\vec{q}, \vec{p}, \chi)). \quad (5.3.2)$$

We chose ΔE such that the energy range was divided into twenty-five energy bins. We also did five times finer binning around energy=-25.5 and 0, i.e., at the onset and disappearance of chaos.

In evaluating the integral we exploited symmetries of $\lambda(\vec{q}, \vec{p})$. The equations of motion have definite parity under the operations

$$q_1, p_1 \rightarrow -q_1, -p_1$$

$$q_2, p_2 \rightarrow -q_2, -p_2$$

$$q_1, q_2, p_1, p_2 \rightarrow -q_1, -q_2, -p_1, -p_2$$

$$p_1, p_2, t \rightarrow -p_1, -p_2, -t$$

$$q_1, q_2, t \rightarrow -q_1, -q_2, -t$$

$$q_1, p_2, t \rightarrow -q_1, -p_2, -t$$

$$q_2, p_1, t \rightarrow -q_2, -p_1, -t.$$

Denoting the original variables by \vec{x} and the transformed variables by \vec{x}' , we have $\dot{\vec{x}}' = \vec{F}'(\vec{x}') = \pm \vec{F}(\vec{x})$. The plus sign occurs if $x_i = x'_i$, the minus if $x_i = -x'_i$. This means that the trajectories are symmetric about the origin in the subspace of the transformed variables. The Lyapunov exponent is invariant under these symmetry operations since it is a function of the trajectories. For those operations which also change time, we must be a little more careful. Integrating backward in time will give minus the smallest exponent since the shrinking direction in forward time is the growing direction in backward time [ER85]. However, since the Lyapunov spectrum for a Hamiltonian with two degrees of freedom = $(\lambda, 0, 0, -\lambda)$, minus the smallest exponent equals the largest exponent. Therefore we need to evaluate the integral in only two of the sixteen sectors of phase space, i.e., only for points in the intervals $0 < q_1, q_2, p_1 < \sqrt{2}$ and $-\sqrt{2} < p_2 < \sqrt{2}$.

The integral was done by Monte Carlo methods. One hundred points were chosen at random in each energy range, the Lyapunov exponent was calculated for those initial conditions, was judged to be positive or zero, and the integral was evaluated as

$$\mu_c = \frac{1}{\mathcal{M}} \sum_{m=1}^{\mathcal{M}} I_m ,$$

where I_m is the integrand for the m th point and \mathcal{M} is the number of Monte Carlo points. These calculations were done on the San Diego Supercomputing Center CRAY XM-P, using single precision variables (14 significant digits). The run time was approximately 5 minutes for 100 initial conditions.

Error bars from the integration are the standard Monte Carlo errors

$$\sigma^2 = \frac{1}{\mathcal{M}} \langle I^2 - \langle I \rangle^2 \rangle ,$$

where the average is taken over the Monte Carlo points. Since the integrand in this case is either 0 or 1, $I = I^2$ and

$$\sigma = \sqrt{\frac{\mu_c(1 - \mu_c)}{\mathcal{M}}} .$$

But if μ_c is either 1 or 0 this formula gives zero error, and is clearly incorrect. To get some estimate of the error in these special cases, we return to the fundamental binomial distribution. Let p be the probability of choosing a chaotic (regular) trajectory at the energy of interest; this is the true value of μ_c ($1-\mu_c$). Then the probability of choosing \mathcal{M} of these trajectories and no regular (chaotic) ones is

$$P(\mathcal{M}) = p^{\mathcal{M}}.$$

If we set $P(\mathcal{M}) = 1/3$, with $\mathcal{M} = 100$, this gives $p = .9891$. Therefore, a choice of $\sigma = .01$ gives a reasonable approximation to the error: we would have little chance of obtaining the result $\mu_c = p \pm 3\sigma$, and a good chance of obtaining $\mu_c = p \pm 1\sigma$.

The heart of this integral (5.3.1) is the calculation of the Lyapunov exponents. Here we use a Bulirsch-Stoer extrapolation method [Pr86] to integrate the equations of motion for \vec{p}, \vec{q} and the tangent vector $\vec{\eta}$ (equation 2.4.1). The series in the extrapolation was said to converge when the percent difference in successive values of the integrated variables was less than 1×10^{-5} .

If there is stretching in the phase space, $\vec{\eta}$ can become quite large, so to avoid numerical overflows it is periodically rescaled to unity. Rescaling does not affect the time evolution of $\vec{\eta}$ since the equations of motion are linear. However, it does mean that we must keep track of the rescalings since the total growth/shrinkage of $\vec{\eta}$ is what we wish to calculate. We write the running Lyapunov exponent (the exponent at finite time)

$$\begin{aligned} \lambda(\vec{p}, \vec{q}, t_m) &= \frac{1}{t_m} \log \frac{|\vec{\eta}(t_m)|}{|\vec{\eta}(t_0)|} \\ &= \frac{1}{t_m} \log \frac{|\vec{\eta}(t_m)|}{|\vec{\eta}(t_{m-1})|} \frac{|\vec{\eta}(t_{m-1})|}{|\vec{\eta}(t_{m-2})|} \frac{|\vec{\eta}(t_{m-2})|}{|\vec{\eta}(t_{m-3})|} \cdots \frac{|\vec{\eta}(t_1)|}{|\vec{\eta}(t_0)|} \\ &= \frac{1}{t_m} \log \prod_{i=1}^m \frac{|\vec{\eta}(t_i)|}{|\vec{\eta}(t_{i-1})|} \\ &= \frac{1}{t_m} \sum_{i=1}^m \log \frac{|\vec{\eta}(t_i)|}{|\vec{\eta}(t_{i-1})|}, \end{aligned} \tag{5.3.3}$$

where m denotes the number of rescalings of $\vec{\eta}$. Each term in the sum is simply the log of the normalization at the m th rescaling. Thus the rescaling keeps $\vec{\eta}$ a manageable size, and allows calculation of the running Lyapunov exponent.

The length of $\vec{\eta}$ is defined as the Euclidean norm: the choice of metric is irrelevant in the infinite time limit. The appropriate time scale for each energy was defined as the average time between returns to a surface of section. The integration was then carried out for 100 to 250 units of time.

A difficulty arose in deciding which exponents are “zero” and which are positive. For this task, the eye seemed better suited than the computer. The running Lyapunov exponent vs. time was graphed on a log-log scale. (Figure 5.3(a)) The typical zero exponent decreases as $1/t$, while a positive exponent remains constant. Looking at the graphs it was usually easy to separate out by eye the two different classes.

There are, however, some ambiguous cases. Figure 5.3(c) shows an exponent which appears to decrease, and then rises. This behavior is independent of the direction of $\hat{\delta}$. It is reasonable to assume that this is a finite time effect: although the trajectory is unstable overall, for a finite time it is stable. No exponents were ever seen to begin a continual decrease after a long period of constancy. Another possible error is shown in Figure 5.3(b) where the exponent is small, but doesn't display the typical linear decrease. It is possible for there to be two or more regions of ergodicity which don't mix (e.g., the regions between KAM tori). Although both regions may be chaotic, their Lyapunov exponents may be very different. There is always the possibility that we judge a positive exponent as zero simply because the exponent is quite small. Because these errors only decrease μ_c from its true value, they are not important when $\mu_c \approx 1$. These are the cases in which we are most interested.

Figure 5.4 shows the final outcome of the calculation. There is a long energy range from -25.5 to -0.18 that is 95% chaotic or greater. These energies will be

referred to as the chaotic energies. The energies between -0.18 and 15 are $70 - 80\%$ chaotic, and will be referred to as quasi-chaotic energies. The remaining energies at both end of the spectrum (-33.34 to -25.5 and 15 to 25.5) are quasi-integrable.

These three dynamics classes were chosen by considering both the classical dynamics and the need for good statistics. We would like for the classical dynamics to be the same (e.g. $\mu_c = \text{constant}$) within each class. Others achieved this goal by choosing systems which scaled in energy [SVZ85,BGS84], i.e., the dynamics are the same at all energies. With our model we have no such scaling. In fact, we are fortunate to find a long range of energy for which we find chaotic behavior. However, requiring that μ_c be nearly constant over the energy range of each class would give too small an energy range, i.e., the number of eigenvalues in this range would not be large enough to calculate meaningful statistics. The final choice of dynamics classes is therefore a compromise between these two competing requirements.

The compromise is least for the chaotic levels, since the change in μ_c is smallest in that energy range. However, for the quasi-chaotic and quasi-integrable levels, the classical dynamics are not stationary, therefore we will expect qualitative, but not quantitative, agreement with the predictions of §4.2.

There is some suggestion that the system at the chaotic energies may be ergodic: the Lyapunov exponents for all the Monte Carlo points look as though they could be converging to the same value (Figure 21), and the points on the surface of section for one trajectory evenly cover the available phase space (Figure 5.28). These facts are necessary but not sufficient to prove ergodicity.

5.4 Quantum Calculations

As described in §5.1, the three level LMG model may be expressed in a finite, collective basis. In this section we will describe this basis in more detail, as well as the quantum calculations of eigenvalues and eigenvectors.

The basis states are labeled by b, c , where b is the number of particles in the first excited level, and c the number in the second. By conservation of particle number,

the population of the ground state $\equiv a = M - b - c$. The ground state has all M particles in the ground level, and is represented by $|00\rangle$. The other basis states are written using the generators

$$|bc\rangle = c(b, c)G_{10}^b G_{20}^c |00\rangle$$

where $c(b, c)$ is the normalizing coefficient. Using the commutation relation for the generators

$$[G_{kl}, G_{k'l'}] = G_{k'l'}\delta_{k'l} - G_{k'l}\delta_{kl'}$$

we may calculate the matrix elements [F180]

$$\begin{aligned} \frac{H_{b'c',bc}}{M\epsilon} &= \langle b'c' | \frac{H}{M\epsilon} | bc \rangle \\ &= \frac{1}{M}(-M + b + 2c)\delta_{bb'}\delta_{cc'} - \frac{\chi}{2M^2}A_{b'c',bc} \end{aligned} \quad (5.4.1)$$

where

$$\begin{aligned} A_{b'c',bc} &= \sqrt{b(b-1)(M-b-c+1)(M-b-c+2)}\delta_{b-2,b'}\delta_{cc'} \\ &+ \sqrt{(b+1)(b+2)(M-b-c)(M-b-c-1)}\delta_{b+2,b'}\delta_{cc'} \\ &+ \sqrt{c(c-1)(M-b-c+1)(M-b-c+2)}\delta_{bb'}\delta_{c-2,c'} \\ &+ \sqrt{(c+1)(c+2)(M-b-c)(M-b-c-1)}\delta_{bb'}\delta_{c+2,c'} \\ &+ \sqrt{(b+1)(b+2)c(c-1)}\delta_{b+2,b'}\delta_{c-2,c'} \\ &+ \sqrt{(c+1)(c+2)b(b-1)}\delta_{b-2,b'}\delta_{c+2,c'} . \end{aligned}$$

The delta functions show explicitly preservation of signature, i.e., the evenness or oddness of each population.

Each of the four matrices is sparse, with no more than seven non-zero elements in each row. Although the diagonal element may be accidentally zero, the off-diagonal elements are never so. Unfortunately sparseness cannot be taken advantage of in diagonalization algorithms, even though it is useful for solving systems of linear equations. However, the matrix is banded since H doesn't connect states for which

$|\Delta b|$ or $|\Delta c|$ is greater than two. The exact band width depends on the ordering of the states. We may exploit the banded form of the matrix to save both computations and storage space.

We chose a basis ordering for which c varies more rapidly than b , and then examined two possibilities for the ordering of c . One choice allows c to vary from 0 (or 1) to $M - b$ (or $M - b - 1$), depending on the signature of each level. The band width for this “increasing- c ” basis is $M/2$. In such a scheme the elements just off the diagonal (i.e., $H_{i,i\pm 1}$) are usually zero; there are indications [Pr86] that this may not be advantageous numerically. Another basis alternates the changes in c : for one value of b , c increases; for $b - 2$, c decreases. This has the advantage of keeping the elements just off the diagonal non-zero; however, the band width is now M . This last “alternating- c ” basis was chosen for calculations, since in numerical tests it gave slightly better results than the increasing- c basis, judging by conservation of the trace.

We used the IMSL diagonalization routine EIGBS, tailored for banded, real, symmetric matrices. This uses the Householder algorithm to reduce the matrix to tridiagonal form, and then calls a QR iterative routine to find the eigenvalues and eigenvectors. These calculations were also done on the San Diego CRAY. As a check on the packaged routine, the trace of H and H^2 were calculated before and after diagonalization. These were conserved to at least one part in 10^8 . The routine uses a nonstandard format for the matrix to take advantage of the banded structure and decrease memory requirements. To ensure that the matrices were constructed correctly, the traces were calculated analytically, and checked with those calculated from H itself.

There were several checks on the correctness of the Hamiltonian. The excellent agreement with classical density of states (Figure 5.6) gives confidence, since the calculations are completely independent. First order perturbation theory gave eigenvalues in agreement with the numerical values to computer precision. Finally,

a similar code written by Brad Flanders [F180], uncovered at a later date, gave agreement to computer precision.

Eigenvalue calculations were done for several different values of M . For $M = 85$ ($\mathcal{N}_{ooo} = 946$ and $\mathcal{N}_{eeo} = 903$) the diagonalization took less than one CRAY minute. The largest matrix was done with $M = 120$, giving $\mathcal{N} = 1830$ or 1891. These last calculations took about 5 minutes.

Eigenvectors took much longer to calculate, and were done only for $M = 85$. Each matrix took about 2 CRAY hours. The difference in timing was due mainly to the banded nature of the matrix; eigenvalue calculations can take advantage of the bandedness, but eigenvector calculations cannot. The measure of quality for the eigenvectors is given by

$$\text{quality} = \max_{1 \leq j \leq \mathcal{N}} \frac{|H\Psi_j - E_j\Psi_j|}{\sqrt{\text{Tr}(H^2)}},$$

where the numerical eigenvalues and eigenvectors are denoted by E_j and Ψ_j . The largest value for the quality was 3×10^{-8} . A total of 13 eigenvectors were not calculated acceptably by the routine, due to near degeneracy of the eigenvalues. This will not affect our calculations.

5.5 Density of States

Before we may calculate level statistics, we must unfold the spectrum, and to do that we must calculate the smoothed density of states. Our choice for this density is Weyl's semiclassical density of states:

$$\rho_{\text{semiclassical}}(E, \chi) = \frac{1}{\hbar^N} \int d^N q d^N p \delta(E - H(\vec{q}, \vec{p}, \chi)). \quad (5.4.1)$$

This is the number of $2N$ -dimensional boxes of volume \hbar^N in phase space. Semiclassical theory states that there is one quantum state per box. This formula may be derived using the coherent states of the previous chapter and the eigenstates $|i\rangle$

of the Hamiltonian

$$\begin{aligned}
\rho(E, \chi) &\equiv \text{tr } \delta(E - \hat{H}(\chi)) \\
&= \text{tr } \delta(E - \hat{H}(\chi)) \int d\mu(\beta) |\Psi(\beta)\rangle \langle \Psi(\beta)| \\
&= \int d\mu(\beta) \langle \Psi(\beta) | \delta(E - \hat{H}) | \Psi(\beta) \rangle .
\end{aligned}$$

So far the derivation is exact: we have only used the completeness of the coherent states (5.2.3). Now we introduce the semiclassical approximation

$$\rho(E, \chi) \approx \int d\mu(\beta) \delta \left(E - \langle \Psi(\beta) | \hat{H}(\chi) | \Psi(\beta) \rangle \right) .$$

The expectation value of a function of H is equal to the function of the expectation value of H in the semiclassical large M limit (5.2.1).

Because we know the eigenvectors for $\chi = 0$, we know the analytic form for $\rho(E, \chi = 0)$. In this integrable limit the eigenvectors in the collective representation are denoted by the average number of particles in each level. Then $\rho(E, 0)$ is the number of eigenstates that give energy E . The lowest energy is $-M\epsilon$, obtained when all particles are in the lower level; the highest energy is $M\epsilon$. There is only one way to make each of these states. In general, in the large M limit

$$\rho(E) = \begin{cases} \frac{M\epsilon - E}{2\epsilon} + 1 & E > 0 \\ \frac{M\epsilon + E}{2\epsilon} + 1 & E < 0 , \end{cases}$$

so that $\rho(E, 0)$ is linear in E , with a discontinuous derivative at $E = 0$. The symmetry about zero is a reflection of the symmetry in the integrable Hamiltonian: the energy is antisymmetric under interchange of populations in levels 0 and 2. The interaction destroys this symmetry because that term is *symmetric* under interchange of the population of any two levels. Therefore, as χ increases from zero the symmetry in $\rho(E, \chi)$ is destroyed.

To calculate the level density, we perform a Monte Carlo integration of 5.4.1, where the delta function is again replaced by a product of two step functions (5.3.2).

Because the energy is invariant if the sign of any two variables flip, we need only choose points from two of the sixteen phase space sectors. Calculations were done using 90 million Monte Carlo points and 200 bins and took about 36 CPU hours on the Kellogg Lab VAX 11-750. The result for $\chi = .75$ and 100 are shown in Figure 5.5. For $\chi = .75$ we have an almost integrable system, and we see the symmetry about $E = 0$. For the larger value of χ this symmetry has disappeared as expected.

The unfolded eigenvalues are

$$x_i = N_{\text{ave}}(E_i) ,$$

where we calculated N_{ave} from ρ_{ave} using cubic spline quadrature. In the next section, all calculations are performed on the unfolded spectrum.

We obtained an alternative ρ_{ave} by histogramming the 7380 eigenvalues for $M = 120$ using 50 bins (Figure 5.6) and then smoothing with cubic splines. This second method allows a check of the dependence of spectral fluctuations on the unfolding. These two different density of states will be denoted by $\rho_{\text{ave}}^{\text{class}}$ and $\rho_{\text{ave}}^{\text{quant}}$.

5.6 Spectral Fluctuations

In this section we show the eigenvalue fluctuations as measured by the statistics $P(s)$, $\Delta_3(L)$, and the three moments of $\bar{n}(L)$. The calculations shown were done for the $M = 120$, $\chi = 100$ LMG model. The number of levels in each signature and classical dynamics class are

	\mathcal{N}_{eee}	\mathcal{N}_{eoo}	\mathcal{N}_{oeo}	\mathcal{N}_{ooo}
chaotic	835	807	806	805
quasi-chaotic	718	696	697	696
quasi-integrable	283	273	273	275.

The quasi-integrable levels at low energies (i.e., $E \approx -33$) were not used (except for $P(s)$) since in all classes this interval contains only 50 levels - too few to give meaningful statistics.

The nearest neighbor spacing is the simplest statistic. In terms of the unfolded spectrum

$$S_i \equiv x_{i+1} - x_i .$$

We actually calculated

$$s_i = (E_i - E_{i-1}) \rho_{\text{ave}}[(E_i + E_{i-1})/2] ,$$

where we used cubic spline interpolation to find ρ_{ave} at the desired values. The spacings from this calculation were then histogrammed to give $P(s)$. The qualitative behavior of the results is the same, whether we use $\rho_{\text{ave}}^{\text{class}}$ or $\rho_{\text{ave}}^{\text{quant}}$ (Figure 5.7d). We checked the stationarity of $P(s)$ by dividing the chaotic levels into three parts, each with about 280 levels. The statistics for each subinterval was in agreement with the Wigner distribution (Figures 5.7a-c). The results were also independent of the signature class (Figures 5.8, 5.9 and 5.10)

The final results were obtained by combining $P(s)$ of all four signature classes after the spacings were calculated for each class separately (Figure 5.11). The chaotic levels were in good agreement with the GOE prediction, while the quasi-integrable levels fit the Poisson distribution, and the quasi-chaotic levels fell in between. This progression is in qualitative agreement with SVZ84,85 and BR84. Specifically, we see that even for $\mu_c \approx .75$, $P(s)$ shows level clustering.

To calculate the Δ_3 statistic, we modify the definition (3.4.4) to give a more efficient algorithm [BG84]

$$\Delta_3(\alpha, L) = \frac{n^2}{16} - \frac{1}{L^2} \left[\sum_{i=1}^n \tilde{x}_i \right]^2 + \frac{3n}{2L^2} \left[\sum_{i=1}^n \tilde{x}_i^2 \right] - \frac{3}{L^4} \left[\sum_{i=1}^n \tilde{x}_i^2 \right]^2 + \frac{1}{L} \left[\sum_{i=1}^n (n-2i+1) \tilde{x}_i \right] ,$$

where \tilde{x}_i are the unfolded eigenvalues when the interval of interest is centered about zero

$$\tilde{x}_i \equiv x_i - \left(\alpha + \frac{L}{2} \right) ,$$

and n is the number of levels in the the interval $[\alpha, \alpha + L]$. This is obtained from 3.4.5 and the replacement of the integrals with sums over eigenvalues:

$$\begin{aligned}\int_{-L/2}^{L/2} N(\tilde{y})d\tilde{y} &= nL - \sum_{p=m}^{n+m-1} \tilde{x}_p \\ \int_{-L/2}^{L/2} \tilde{y}N(\tilde{y})d\tilde{y} &= nL^2 - \frac{1}{2} \sum_{p=m}^{n+m-1} \tilde{x}_p^2 \\ \int_{-L/2}^{L/2} N^2(\tilde{y})d\tilde{y} &= n^2L + \sum_{p=m}^{n+m-1} (-2p+1)\tilde{x}_p.\end{aligned}$$

The final result is the spectral average of Δ_3

$$\langle \Delta_3(L) \rangle = \frac{1}{N_\alpha} \sum_{\alpha} \Delta_3(\alpha, L).$$

where α 's are chosen such that successive intervals overlap by $L/2$; this choice was made to balance the desire for good statistics and the need to avoid correlations. N_α counts the number of intervals. Using the same averaging procedure, we calculate

$$\begin{aligned}\langle n(L) \rangle &= \frac{1}{N_\alpha} \sum_{\alpha} n(\alpha, L) \\ \Sigma^2(L) &= \frac{1}{N_\alpha} \sum_{\alpha} [n(\alpha, L) - \langle n(L) \rangle]^2 \\ \gamma_1(L) &= \frac{1/N_\alpha \sum_{\alpha} [n(\alpha, L) - \langle n(L) \rangle]^3}{\Sigma^3(L)} \\ \gamma_2(L) &= \frac{1/N_\alpha \sum_{\alpha} [n(\alpha, L) - \langle n(L) \rangle]^4}{\Sigma^4(L)} - 3.\end{aligned}$$

There will be errors in these calculations due to the finite sample size. We may determine the error either from the sample, or from the GOE distribution itself. For Δ_3 we determined the error from the sample

$$\text{Var}(\Delta_3(L)) \equiv \frac{1}{N_\alpha} \sum_{\alpha} [\Delta_3(\alpha, L) - \langle \Delta_3(L) \rangle]^2.$$

This variance is shown in the graphs of the results. For the r th moment, the variance is given by

$$\text{Var}(m_r) \approx \frac{1}{N_\alpha} (m_{2r} - m_r^2),$$

and depends on higher moments. For our small sample sizes, the variance of the the moments aren't well determined; higher order moments require larger samples to be well determined. In this case we turned to ensemble averages for estimates of errors due to finite sample sizes. We quote the results from Bohigas *et al.* [BHP85]. They used Monte Carlo techniques to construct many members of the GOE, and then performed ensemble averaging. Their results for a sample size $M = 1762$ are

L	$\text{Var}(\Sigma^2(L))$	$\text{Var}(\gamma_1(L))$	$\text{Var}(\gamma_2(L))$	
0.25	.001	.02	.08	
≈ 1	.009	.02	.05	
5	.03	.05	.08	(5.6.1)

Since our sample size is smaller, these give a lower bound on the errors. We know that the error must vanish at least as quickly as $1/p$, where p is the sample size [Pa79]; therefore, we may adjust these estimates by multiplying by $\sqrt{1762/p}$. This factor ranges from 2.5 for $p = 280$ to 1.45 for $p = 835$.

The predicted values of these statistics for a Poisson spectrum may be written in analytic form. (eq 3.4.6). The results for GOE are harder to come by. The number variance is given exactly [HPB82]

$$\Sigma^2(L) = \frac{2}{\pi} \left\{ \ln(2\pi L) + \gamma + 1 + \frac{1}{2} \text{Si}(\pi L)^2 - \frac{1}{2} \pi \text{Si}(\pi L) - \cos(2\pi L) - \text{Ci}(2\pi L) + \pi^2 L \left[1 - \frac{2}{\pi} \text{Si}(2\pi L) \right] \right\},$$

where Ci and Si are the sine and cosine integrals, and γ is Euler's constant. The other statistics can be expressed in terms of the variance and spacing distributions [BG84]

$$\begin{aligned} \gamma_1(L) &= \sum_{k=0}^{\infty} \frac{(k-L)^3 E(k, L)}{\Sigma^3(L)} \\ \gamma_2(L) &= \sum_{k=0}^{\infty} \frac{(k-L)^4 E(k, L) - 3\Sigma^2(L)}{\Sigma^4(L)} \\ \Delta_3(L) &= \frac{2}{L^4} \int_0^L (L^3 - 2L^2x + x^3) \Sigma^2(x) dx . \end{aligned}$$

The values of $E(k, L)$, the probability that an interval of length L contains exactly k levels, are tabulated in [MdC72]. The sum over k was actually taken only over 7 values at most, since $E(k, L)$ is strongly peaked at $k = L$. The GOE predictions calculated from these formulas are shown in the figures by the solid curves, Poisson predictions are given by the dashed curves.

Again we checked for independence from unfolding procedure. Using either $\rho_{\text{ave}}^{\text{quant}}$ or $\rho_{\text{ave}}^{\text{class}}$ gave the same Δ_3 results, however, Σ^2 , γ_1 , and γ_2 disagreed for $L > 2.5$ (Figure 5.12). This is a manifestation of the errors due to the small sample size; the fluctuations were of the size predicted by GOE (eq 5.6.1). We also checked stationarity, again by dividing the chaotic levels into three intervals (Figure 5.13). We did see some dependence of Δ_3 , but this was to be expected. We know that the classical dynamics over the chaotic energies are not completely independent of energy: μ_c varies between .95 and 1.00. We do see that the most chaotic levels ($\bar{\mu}_c = 1.0$) gives the stiffest spectrum, while the least chaotic ($\bar{\mu}_c \approx .97$) gives the softest. The higher statistics also show stationary behavior for $L < 1.5$. However, again we see the finite sample effects in the scatter at higher L , and since the sample is smaller the variations are visibly greater.

Looking at the *oeo* class, we examine the behavior for chaotic, quasi-chaotic, and quasi-integrable levels (Figure 5.14). We see the predicted results: good agreement with GOE for the chaotic levels, a less stiff spectrum for the quasi-chaotic levels, and an even less stiff spectrum for the quasi-integrable levels. For the quasi-integrable levels and γ_1 and γ_2 statistics, there is significant systematic deviation from both GOE and Poisson results.

However, we saw completely unexpected results when we checked the dependence on signature class (Figure 5.15). The *eee* matrix was significantly softer than the *ooe* and *eoo* which were softer than the *oeo*. When we looked at an odd M matrix, the pattern was repeated, but with all even and odd labels exchanged (i.e., *oeo* was stiffest, *ooo* least stiff). In the following discussion of this phenomenon we

will keep to M even, but the conclusions also apply to the M odd case. We will also only examine the chaotic levels, since this gives the largest number of levels, and because the classical dynamics is nearly stationary.

The explanation became clear when we examined the $\chi = \infty$ limit. In this case the three LMG levels are degenerate in energy, and H is invariant under interchange of the level labels (5.4.1). Let P_i be one of the three operators which permutes two of the three levels, then

$$HP_i = P_iH .$$

In the classical system, this discrete symmetry means that H is unchanged if $p_1 \leftrightarrow p_2$ and $q_1 \leftrightarrow q_2$. A discrete symmetry does not induce integrability as a continuous symmetry would, so the system may still be chaotic. However, in the quantum system, a discrete symmetry implies that H may be written in block diagonal form. If we look at the spectrum of the *entire* matrix, we should expect to see Poisson statistics (recall §3.2) regardless of the classical dynamics. However, if we look at the spectra of each of the block diagonal matrices separately, we should see GOE results if the system is classically chaotic, or Poisson if it is classically integrable.

For the $\chi = 100$ case, we are quite close to the $\chi = \infty$ limit. Therefore we have a “partially conserved” discrete symmetry. This makes no difference to the classical dynamics, but in the quantum system H may be written in nearly block diagonal form; “nearly” means that the elements which connect these matrices are relatively small.

To see if this “partially conserved” discrete symmetry was the cause of dependence on signature, we calculated the eigenvalues for $\chi = \infty$. (All calculations with $\chi = \infty$ are done for H/χ .) There are only two signature classes (and therefore only two different spectra) in this limit since the oeo , ooe , and ooo matrices are identical. The eigenvalues were calculated twice, once for the entire matrix, and once for the block diagonal matrices separately.

To write H in block diagonal form, we need new basis states. This is easiest for the ooo signature class. Because s_0 is even while s_1 and s_2 are odd, we are only

interested in states that have a definite parity under interchange of labels 1 and 2. Using the states of §5.4, and showing the population of the ground state explicitly, we write the new basis:

$$\begin{aligned}\Psi_{\text{sym}} &\equiv \frac{1}{\sqrt{2}} [|a, b, c\rangle + |a, c, b\rangle] \\ \Psi_{\text{asym}} &\equiv \frac{1}{\sqrt{2}} [|a, b, c\rangle - |a, c, b\rangle] ,\end{aligned}$$

H doesn't couple these two bases

$$\begin{aligned}H &= P^{-1}HP \\ \langle \Psi_{\text{sym}} | H | \Psi_{\text{asym}} \rangle &= \langle \Psi_{\text{sym}} | P^{-1}HP | \Psi_{\text{asym}} \rangle \\ &= \langle P\Psi_{\text{sym}} | H | P\Psi_{\text{asym}} \rangle \\ &= \langle \Psi_{\text{sym}} | H | -\Psi_{\text{asym}} \rangle \\ &= 0 ,\end{aligned}$$

therefore H_{eoo} is made up of two block diagonal matrices. We may obtain the symmetric and antisymmetric eoo eigenvalues by diagonalizing H in each basis separately.

The eee class is more complicated, since the populations of all the levels may be interchanged. The basis states are

$$\begin{aligned}\Psi_{\text{sym}} &\equiv \frac{1}{\sqrt{6}} [|a, b, c\rangle + |b, a, c\rangle + |b, c, a\rangle + |c, b, a\rangle + |c, a, b\rangle + |a, c, b\rangle] \\ \Psi_{\text{asym}} &\equiv \frac{1}{\sqrt{6}} [|a, b, c\rangle - |b, a, c\rangle + |b, c, a\rangle - |c, b, a\rangle + |c, a, b\rangle - |a, c, b\rangle] \\ \Psi_{\text{P}_{01}\text{sym}}^{(1)} &\equiv \frac{1}{\sqrt{12}} [2|a, b, c\rangle + 2|b, a, c\rangle - |b, c, a\rangle - |c, b, a\rangle - |c, a, b\rangle - |a, c, b\rangle] \\ \Psi_{\text{P}_{01}\text{sym}}^{(2)} &\equiv \frac{1}{\sqrt{4}} [|b, c, a\rangle + |c, b, a\rangle - |c, a, b\rangle - |a, c, b\rangle] \\ \Psi_{\text{P}_{01}\text{asym}}^{(1)} &\equiv \frac{1}{\sqrt{12}} [2|a, b, c\rangle - 2|b, a, c\rangle - |b, c, a\rangle + |c, b, a\rangle - |c, a, b\rangle + |a, c, b\rangle] \\ \Psi_{\text{P}_{01}\text{asym}}^{(2)} &\equiv \frac{1}{\sqrt{4}} [|b, c, a\rangle - |c, b, a\rangle - |c, a, b\rangle + |a, c, b\rangle] .\end{aligned}$$

The first two states are totally symmetric or antisymmetric under interchange of any two levels. $\Psi_{\text{P}_{01}\text{sym}}$ states are symmetric only under interchange of levels 0

and 1, while $\Psi_{P_{01}\text{asym}}$ states are antisymmetric under the same operation; all four P_{01} states have mixed parity under any of the other permutation operations. In this basis H couples only P_{01} symmetric states together and the P_{01} antisymmetric states together; therefore, the eee matrix is made up of four block diagonal matrices.

We also needed to calculate $\rho_{\text{ave}}^{\text{class}}$ and $\mu_c(\chi = \infty)$ to find the spectral statistics. This was again done using the scaled Hamiltonian H/χ . The results, except for energy scale, are very similar to the $\chi = 100$ values, confirming that $100 \approx \infty$. The classically chaotic energies lie in the interval $[-.242, .0159]$ (Figure 5.16).

Figures 5.17-5.20 show the results of these two calculations. When we calculate the statistics of the entire ooo or eee class, we see results that are much closer to Poisson than GOE. However, when we look at the spectra of the individual symmetry classes separately, we see good agreement with GOE. The results are independent of permutation symmetry class. We show only the statistics for three spectra in the eee case since the two P_{01} matrices are exactly the same.

For the $\chi = 100$ case, we understand qualitatively the relative stiffness of the spectra, as indicated by the Δ_3 results. The ooo and ooe matrices are nearly the same, and less stiff than the eee class. If we consider the energy separation of the three LMG levels as a perturbation, then $\Delta E_{ooo} = \Delta E_{ooe} \propto \epsilon$ while $\Delta E_{oeo} \propto 2\epsilon$ because the levels with the same signature are either one or two ϵ apart as the perturbation is turned on. Therefore in the ooe and ooo classes the symmetry is “less broken” than in the oeo case. The eee class is the softest of all; we may attribute this to the difference between having two or four block diagonal matrices for $\chi = \infty$. The eee class has four, so the matrix has relatively more zeros, and therefore less coupling, to begin with. When the perturbation is added, although the size of the mixing is the same as for the other classes, its effect is diluted by the sea of zeros.

We note in passing that the classical H cannot be made to reflect the signature of the quantum states, and hence cannot account for the signature dependence. We

may write (5.2.1)

$$\begin{aligned}\Psi_{xee} &\equiv \left(e^{z_1 G_{10}} + e^{-z_1 G_{10}} \right) \left(e^{z_2 G_{20}} + e^{-z_2 G_{20}} \right) |0\rangle \\ &= |z_1, z_2\rangle + | -z_1, z_2\rangle + |z_1, -z_2\rangle + | -z_1, -z_2\rangle ,\end{aligned}$$

where this state has an even number of particles in levels 1 and 2, and the x indicates that the signature of the ground level is arbitrary (but fixed once M is chosen). We may also write

$$\begin{aligned}\Psi_{xoo} &\equiv \left(e^{z_1 G_{10}} - e^{-z_1 G_{10}} \right) \left(e^{z_2 G_{20}} - e^{-z_2 G_{20}} \right) |0\rangle \\ &= |z_1, z_2\rangle - | -z_1, z_2\rangle - |z_1, -z_2\rangle + | -z_1, -z_2\rangle ,\end{aligned}$$

with similar expressions for $\Psi_{x eo}$ and $\Psi_{x oe}$. In the $M \rightarrow \infty$ limit, the expectation value of H between states of different z (e.g., z_1 and $-z_1$) vanishes (see Appendix), hence the cross terms using the signature conserving states disappear, and the classical limit is the same no matter the signature class. This is as we'd expect; in the continuum limit of particles, evenness and oddness have no meaning.

Finally, we examine the kink in the Δ_3 statistic, and compare our results with Berry's analytical predictions (§4.3). Specifically we check for a saturation of $\Delta_3(L)$ at $L_{\max} \equiv \hbar \rho_{\text{ave}}(E)/T_{\min}$ (3.4.3). First we find \hbar in terms of M . By the Weyl rule

$$\mathcal{N} \equiv \text{number of states} \equiv \frac{\text{phase space volume}}{4\pi^2 \hbar^2} ,$$

while for the LMG model $\mathcal{N} \approx M^2/2$. The phase space volume is the volume of a four ball of radius $\sqrt{2}$. Putting this altogether gives $\hbar = \sqrt{2}/M$. From Figure 5.5, $\rho_{\text{ave}}(E)$ for the chaotic energies is about $.02M^2/8$. The extra factor of four comes from the four different symmetry classes. Plugging this into the definition of L_{\max} , we have

$$L_{\max} = \frac{.0035 M}{T_{\min}} .$$

The first thing to note is that L_{\max} scales linearly with M . In Figure 22 we show Δ_3 for $M = 65$ and $M = 120$. For $M = 120$ the statistic saturates at $L \approx 40$.

For $M = 65$, it does not appear as though saturation ever occurs; however, the rate of increase becomes a relatively small constant at $L \approx 20$. If we take this as the saturation value of L , the M scaling holds very well.

Using $L_{\max} = 40$, and $M = 120$, we obtain $T_{\min} = .01$. This is about $1/7$ the characteristic time, i.e., the time between crossings of a fixed plane in phase space. This is smaller than might be expected, but not totally unreasonable.

This rough agreement is all we can hope for, both because we are far from the semiclassical limit where the analytical results apply, and because we know nothing about the periodic orbits of the classical system.

5.7 Overlap Distributions

In the last section we examined the spectral fluctuations, and found them in good agreement with expectations. We proceed to examine the eigenvector fluctuations of the LMG model. The results quoted here are part of work in progress; many questions remain open.

Because the number of basis states for the model is finite, we have been able to calculate the eigenvectors without *ad hoc* truncation of the basis (§5.4). This is one advantage of our model: most systems that have been studied by others do not yield many reliable eigenstates. All of the results in this section are for $M = 85$, for which $\mathcal{N}_{ooo} = 903$ and $\mathcal{N}_{eeo} = \mathcal{N}_{oee} = \mathcal{N}_{eoe} = 946$.

We have tested the GOE prediction (3.5.1) that the overlap $x_{i\lambda} \equiv \langle i|\lambda \rangle$ is a Gaussian random variable, where i is an eigenvector and λ is an arbitrary basis state. The width of the Gaussian distribution is $\sqrt{1/\mathcal{N}}$, where \mathcal{N} is the size of the basis; this is simply the average overlap for normalized states. The simplest choice of basis is the original basis in which the Hamiltonian is written, i.e., the eigenvectors of the number operator. This calculation can be done by fixing either λ or i , and then histogramming the values x_i or x_λ .

We chose i in the chaotic, quasi-chaotic, and quasi-integrable regions. Looking first at the chaotic results, we find excellent agreement with GOE for energies of -4

and -5, fair agreement at -10, and no agreement at -11, -19, -20. In these last cases there were far too many small values of x_λ . For the quasi-chaotic energies of 5 and 10 the results were not Gaussian random, and they were distinctly far from Gaussian at the quasi-integrable energies of -30 and 25. (Figures 5.22 and 5.23) In these cases most of the strength is in a few x_λ 's, resulting in a sharp peak near zero with long tails. This uneven distribution is more pronounced for the quasi-integrable than the quasi-chaotic energies.

We also examined the data by fixing λ to three different values: 500, 451, 823 (Figures 5.24-2.26). These correspond to $a = 6, b = 23, c = 56$; $a = 30, b = 27, c = 28$; and $a = 76, b = 5, c = 4$, where a, b, c are the populations of the ground, first, and second levels. The x_i were examined for i 's in the chaotic, quasi-chaotic, and quasi-integrable regions separately. Again for the quasi-chaotic and quasi-integrable levels we do not see agreement with a Gaussian distributions. For all of the quasi-integrable cases we again see the very sharp spike near zero with long tail. For the quasi-chaotic we also see a peak; it is most pronounced for $\lambda = 823$, less so for 451, and even less for 500. The chaotic x_i appear Gaussian for $\lambda = 500$, but the results are not so clear for 451, and for 823 we see the same large peak at zero as for the quasi-chaotic and quasi-integrable cases.

Quantitative predictions for strength outside of the chaotic region come from Alhassid and Levine [AL86] who use information theory to derive the distribution for $y = x^2$:

$$P(y) = \frac{(\nu/2)^{\nu/2}}{\Gamma(\nu/2)} (y\mathcal{N})^{\nu/2-1} \exp(-\nu y\mathcal{N}/2) .$$

This is a χ^2 distribution for a system with ν degrees of freedom. For the chaotic limit $\nu = 1$, as ν increases the distribution becomes more sharply peaked; this qualitative expectation is in agreement with our results.

It is not clear why the results for E=-20,-19, and -11 are far from Gaussian. These energies are well in the chaotic region, and the classical dynamics are similar to the dynamics at E=-4 and -5 where the results are Gaussian.

The distribution for all levels when $\lambda = 832$ is very peaked, even for the chaotic energies. This may be because this vector is close to the unperturbed ($\chi = 0$) ground state, and therefore is not a typical basis vector.

This is not a closed subject. We would like to understand the deviations from prediction mentioned in the last two paragraphs, and we have not yet tested the prediction about strengths $\equiv y \equiv \langle f|T\rangle$.

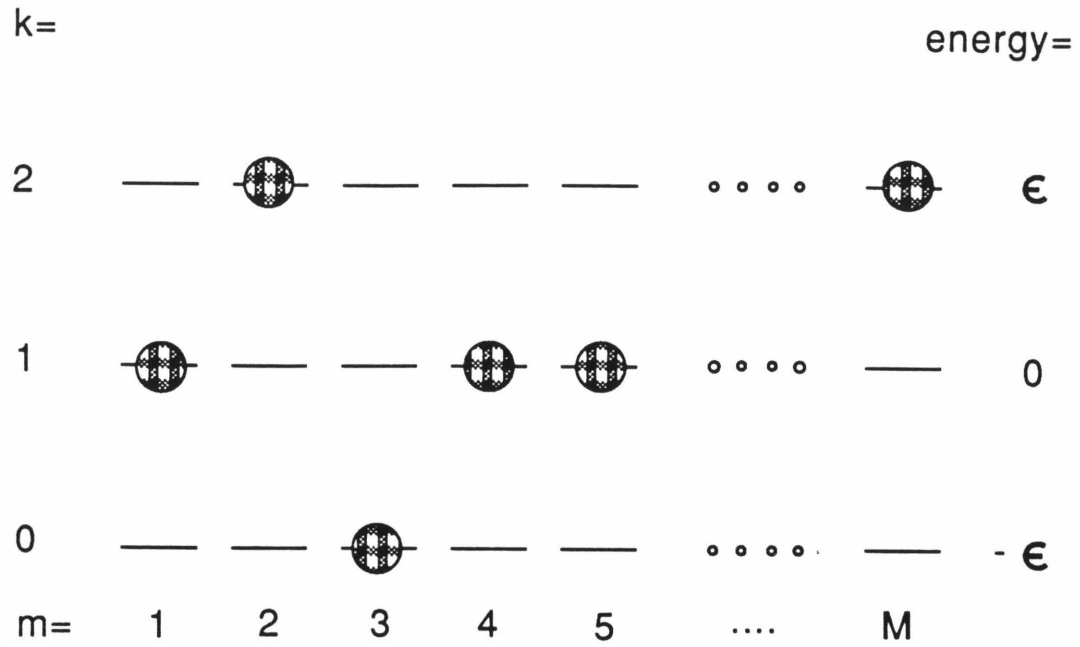


Figure 5.1 Cartoon of the three level LMG model. (5.1.1) Each of the three levels is M -fold degenerate; there is exactly one particle for each m value. We take the levels symmetric about zero energy: $\epsilon_2 = -\epsilon_0 \equiv \epsilon$, $\epsilon_1 = 0$. The interaction moves a pair of particles from one level to another.

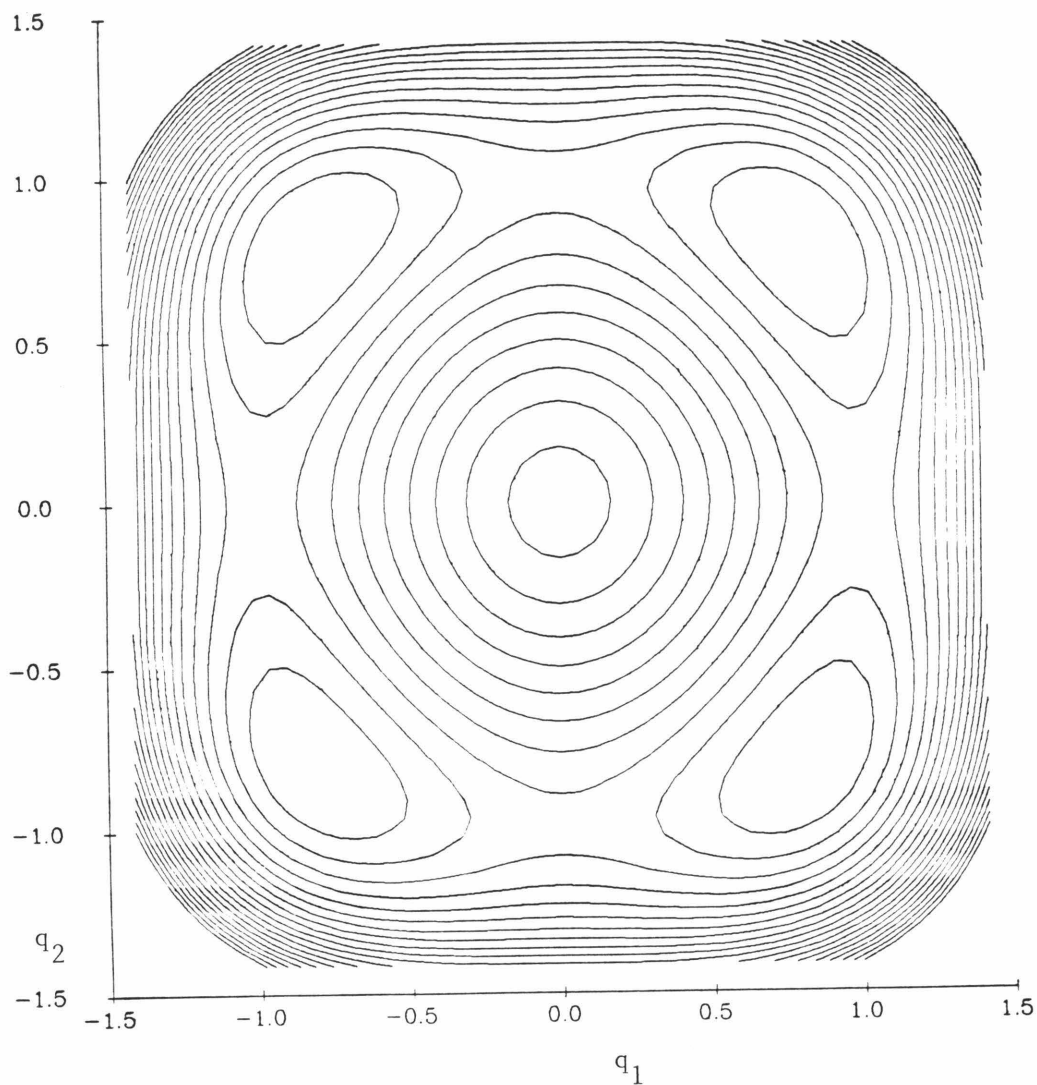


Figure 5.2 Potential energy surface ($H(\vec{q}, \vec{p} = 0)$) for the classical LMG model (5.2.5) with $\chi = 100$. There are four minima at $q_1^2 = \pm 2/3$ and $q_2^2 = \pm 0.65$ with $E_{\min} = -33.34$, a local maximum at $q_1 = q_2 = 0$ with $E = -1$, and saddle points at $q_1^2 = .99$ and $q_2^2 = 0.0$ with $E = -25.5$ and at $q_1^2 = 0.0$ and $q_2^2 = .98$ with $E = -25.01$. At energies just above E_{\min} the classical motion is a quasi-integrable oscillation about one of the minima.

Figure 5.3 Typical results for the running Lyapunov exponent (5.3.1). (a) The running Lyapunov exponent for two chaotic trajectories and for two regular trajectories – the first two are nearly constant, while the last two decrease steadily with time. In (b) and (c) a typical positive and zero exponent are shown for reference. (b) A puzzling exponent, which is probably positive but small. (c) Another puzzling exponent that decreases and then sharply increases – a finite time effect. All exponents are for the LMG model with $\chi = 100$ and $E \approx 0$.

Figure 5.4 Chaotic volume for LMG model with $\chi = 100$ (5.3.1). The boxes indicate energies that were judged chaotic, the diamonds indicate quasi-chaotic energies, and the crosses show quasi-integrable energies.

Figure 5.5 Classical density of states. Results of integrating eq 5.4.1 for $\chi = .75$ and 100 using 200 energy bins and 90 million Monte Carlo points. Note the different energy scales for the two cases, the normalization is chosen so that the integral of the density equals one.

Figure 5.6 Comparison of the density of states from classical and quantum calculations. The histogram gives the number of eigenvalues in each energy interval for $M = 120$ LMG model. The smooth curve is the classical result shown in Figure 5.5.

Figure 5.7 Checks on $P(s)$. (a),(b), and (c) The nearest neighbor statistic for three subintervals in the chaotic region, and (d) for the entire chaotic interval but using $\rho_{\text{ave}}^{\text{quant}}$ to do the unfolding. The results all show the level repulsion typical of GOE.

Figure 5.8 The results of $P(s)$ for the chaotic energies are shown for each signature class separately. There are about 800 counts for each matrix. The results are similar for each class.

Figure 5.9 $P(s)$ for the quasi-chaotic energies for each signature class separately. There are about 700 counts for each class.

Figure 5.10 $P(s)$ for the quasi-integrable energies for each signature class separately. There are about 320 counts for each class.

Figure 5.11 The results of $P(s)$ calculations, the spacings for all four signature classes have been combined. The top graph shows the 3249 spacings from chaotic levels, the middle graph shows the 2803 spacings from quasi-chaotic levels, and the bottom graph shows the 1100 spacings from quasi-integrable levels. The solid line is the GOE prediction, the dashed line is the Poisson prediction. As theorized, the chaotic levels agree with GOE, the quasi-integrable levels agree with Poisson, and the quasi-chaotic levels lie in between.

Figure 5.12 Check on the effects of unfolding procedure on statistics. Using either $\rho_{\text{ave}}^{\text{class}}$ or $\rho_{\text{ave}}^{\text{quant}}$. The statistics display independence from unfolding procedure. Results are for the *oeo* matrix, chaotic energies only.

Figure 5.13 Check on the stationarity of statistics. Results are shown for three subintervals in the chaotic interval for the *oeo* matrix. They are fairly stationary, with deviations that can be understood in terms of non-stationarity of the classical dynamics. The sample size is about 280 levels for each interval.

Figure 5.14 Effect of classical dynamics on the level fluctuations. Statistics are shown for the *oeo* matrix for the three different classical dynamics classes. The chaotic levels (numbering 835) are in agreement with GOE while the quasi-chaotic (numbering 718) and quasi-integrable (numbering 283) levels are approaching Poisson.

Figure 5.15 Dependence on signature class. The statistics for the chaotic energies are shown for three different signature classes; the *ooe* class is omitted for clarity, since it is quite close to the *ooo* results.

Figure 5.16 Chaotic volume for $\chi = \infty$. The results are quite close to the $\chi = 100$ calculation, but give a somewhat smaller chaotic energy interval from $E = -.242$ to $-.0159$. Boxes indicate the chaotic energies.

Figure 5.17 Effects of ignoring symmetries. $P(s)$ for the $eo0/oe0$ matrix for the full basis, i.e., when the permutation symmetries are ignored, and when they are respected. Calculations for the symmetric/antisymmetric basis were done for $M = 160$ giving about 400 chaotic levels for each matrix. Calculations for the full matrix were done for $M = 85$ giving 356 chaotic levels.

Figure 5.18 Same as Figure 5.17, but for the eee/ooo matrix. The high degree of level clustering occurs because two of the four block diagonal matrices are identical. These calculations were done for $M = 125$ giving about 200, 200 and 400 chaotic levels for the symmetric, antisymmetric and P_{01} symmetric bases. The full matrix was diagonalized for $M = 85$ giving 371 chaotic levels.

Figure 5.19 Effects of ignoring symmetries on the higher order statistics. The Δ_3 and Σ^2 statistics become much stiffer when the symmetry classes are treated separately. These results are for the $eo0/oe0$ matrix.

Figure 5.20 Same as Figure 5.19, but showing the results for the eee/ooo matrix. Again we see better agreement with GOE when the symmetries are respected.

Figure 5.21 Running Lyapunov exponent (5.3.1) for $\chi = 100$, $-21.6 \leq \text{Energy} \leq -19.3$, and one hundred initial conditions. It appears as though $\lambda(\vec{x}_0, t)$ for all \vec{x}_0 may be converging to the same value since the spread in values is decreasing with time. This result is not inconsistent with ergodicity.

Figure 5.22 Saturation of the Δ_3 statistic occurs at $L \approx 20$ for $M = 65$, and at $L \approx 40$ for $M = 120$. This scaling of L with M agrees with the predictions of Berry (4.3.3).

Figure 5.23 Distribution of the overlap of a chaotic energy eigenvector with the basis generated by the eigenvectors of the number operator. The results are not always Gaussian (the GOE prediction). The solid lines are Gaussians fit to the data.

Figure 5.24 Same as Figure 5.23, except for quasi-integrable eigenvectors (top) and quasi-chaotic eigenvectors (bottom). The width of these distributions is much narrower than Gaussian.

Figure 5.25-5.27 Distribution of the overlap of a fixed number eigenvector with a range of energy eigenvectors. The number eigenvectors are $a = 6, b = 23, c = 56$ (5.25); $a = 30, b = 27, c = 28$ (5.26); and $a = 76, b = 5, c = 4$ (5.27); where a, b, c are the populations of the ground, first, and second levels of the LMG model. The distributions for the chaotic eigenvectors are wider than the distributions for the other two dynamics classes.

Figure 5.28 Trajectories (left column) and surfaces of section (right column) at three different energies for the LMG model. The top graphs are for $E = -30$, when the system is quasi-integrable. Five sets of initial conditions were used for the surface of section, each giving a closed curve typical of near-integrable systems. The middle graphs are for $E = -2$, when the system is chaotic. The small triangles in the surface of section are centered on points which are energetically inaccessible. Only one set of initial conditions was used for the surface of section. Since this one trajectory appears to evenly cover the available phase space, it is reasonable to believe that the system is ergodic at this energy. The bottom graphs are for $E = 10$, when the system is quasi-chaotic. Again, the small triangles on the surface of section indicate unavailable phase space. Three sets of initial conditions were used for the surface of section. One gave the sea of chaotic dots, and the two closed curves in the lower right hand corner were from two different sets of initial conditions. The $q_1 - q_2$ trajectory corresponds to the larger of the two closed curves.

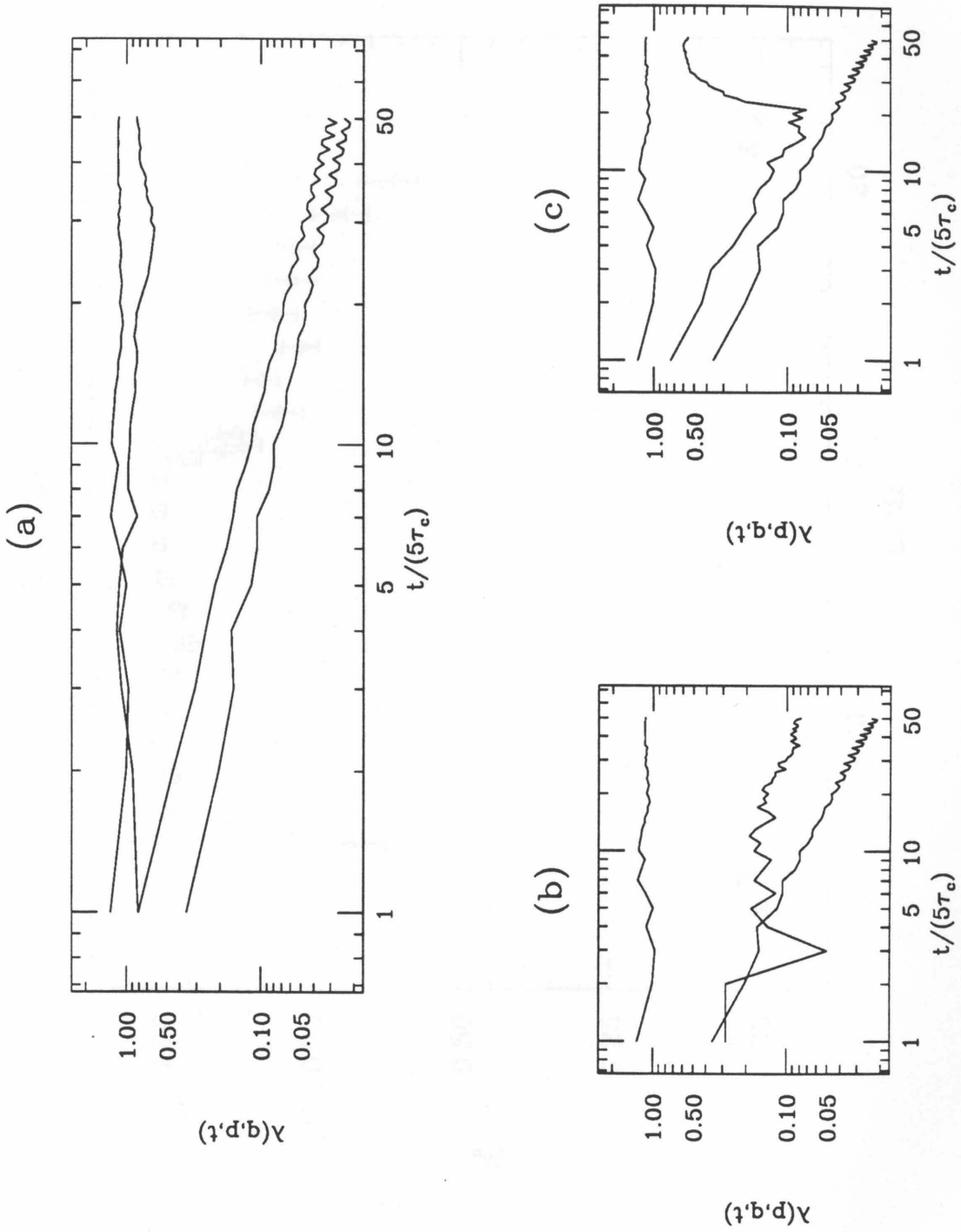


Figure 5.3

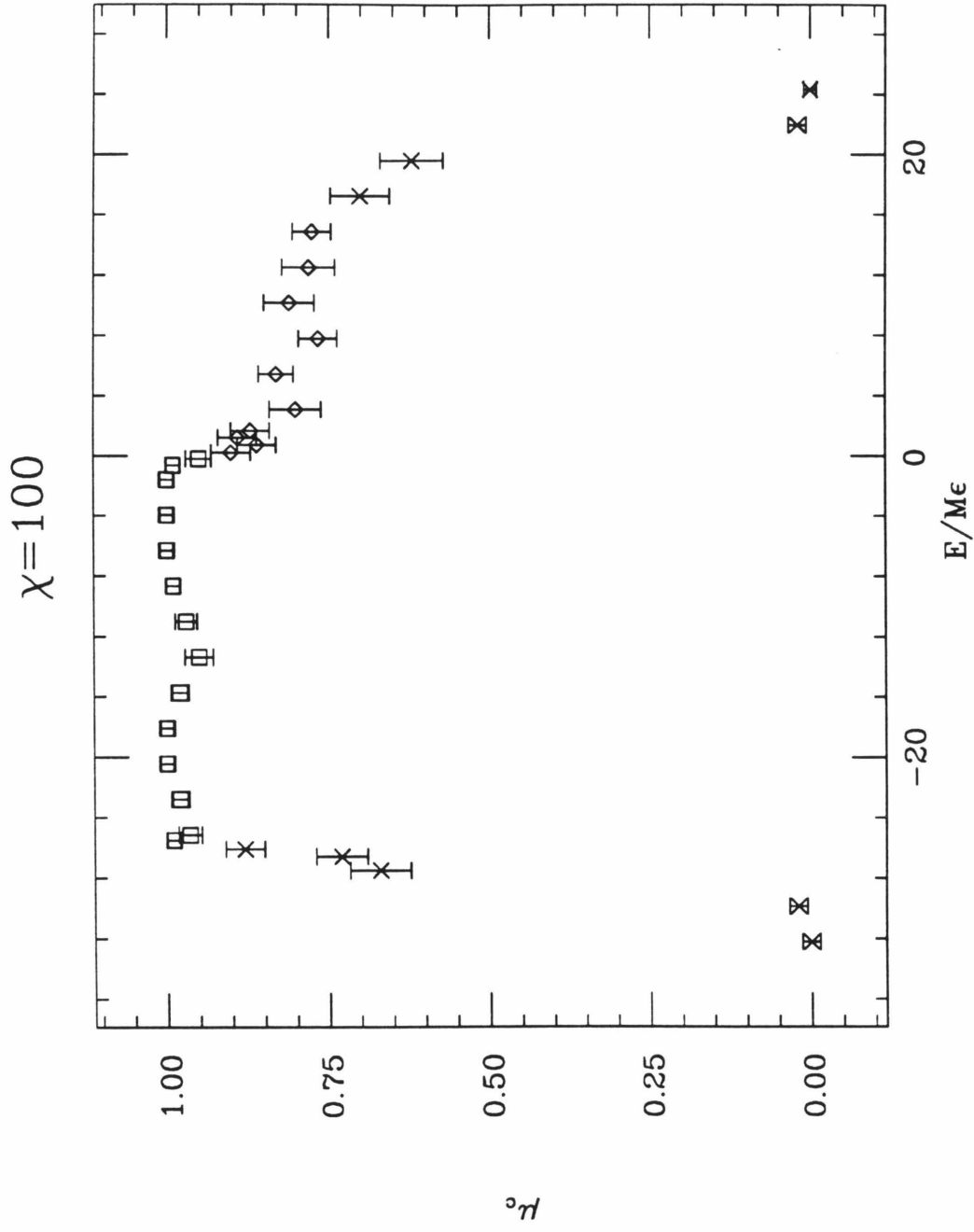


Figure 5.4

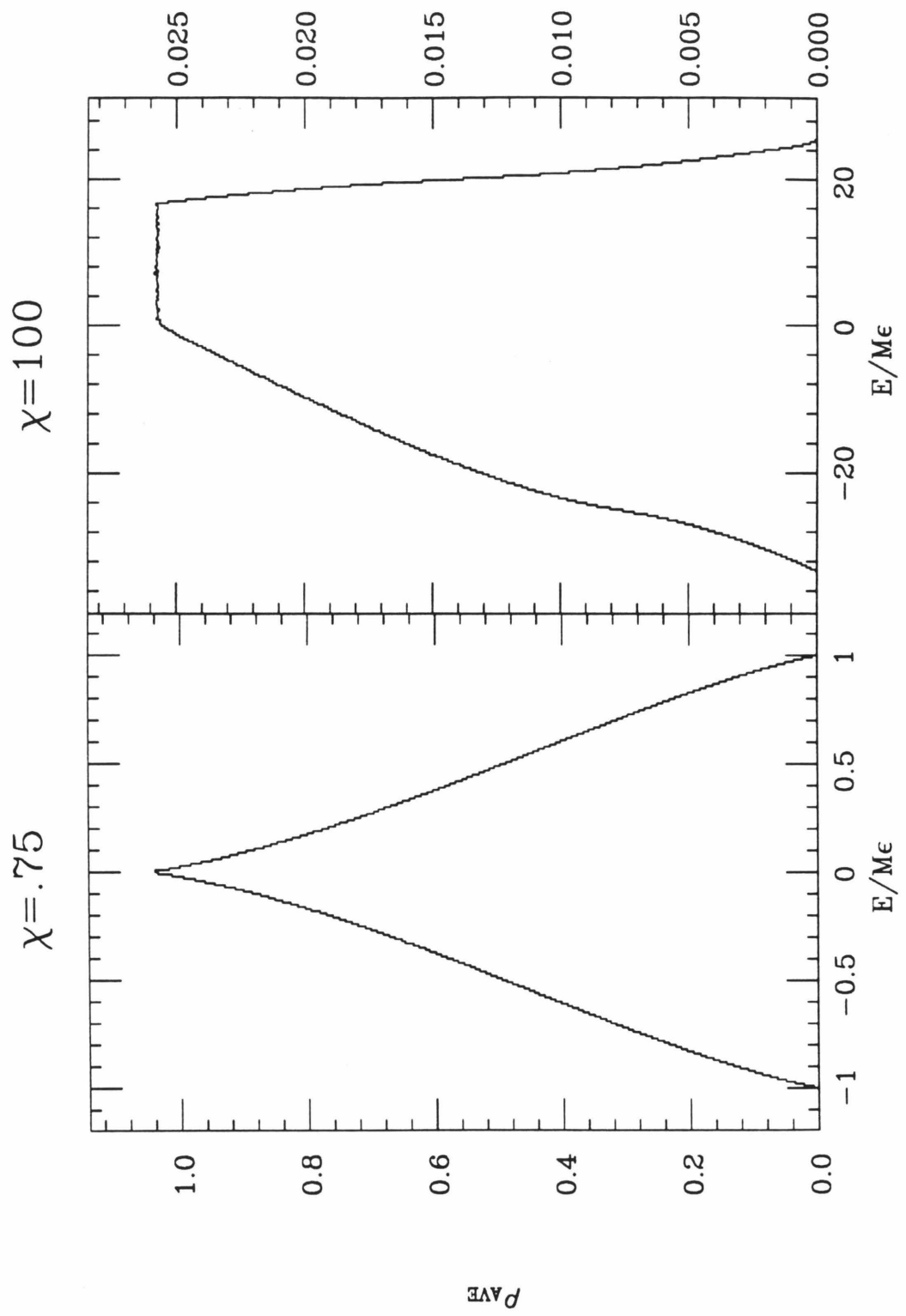


Figure 5.5

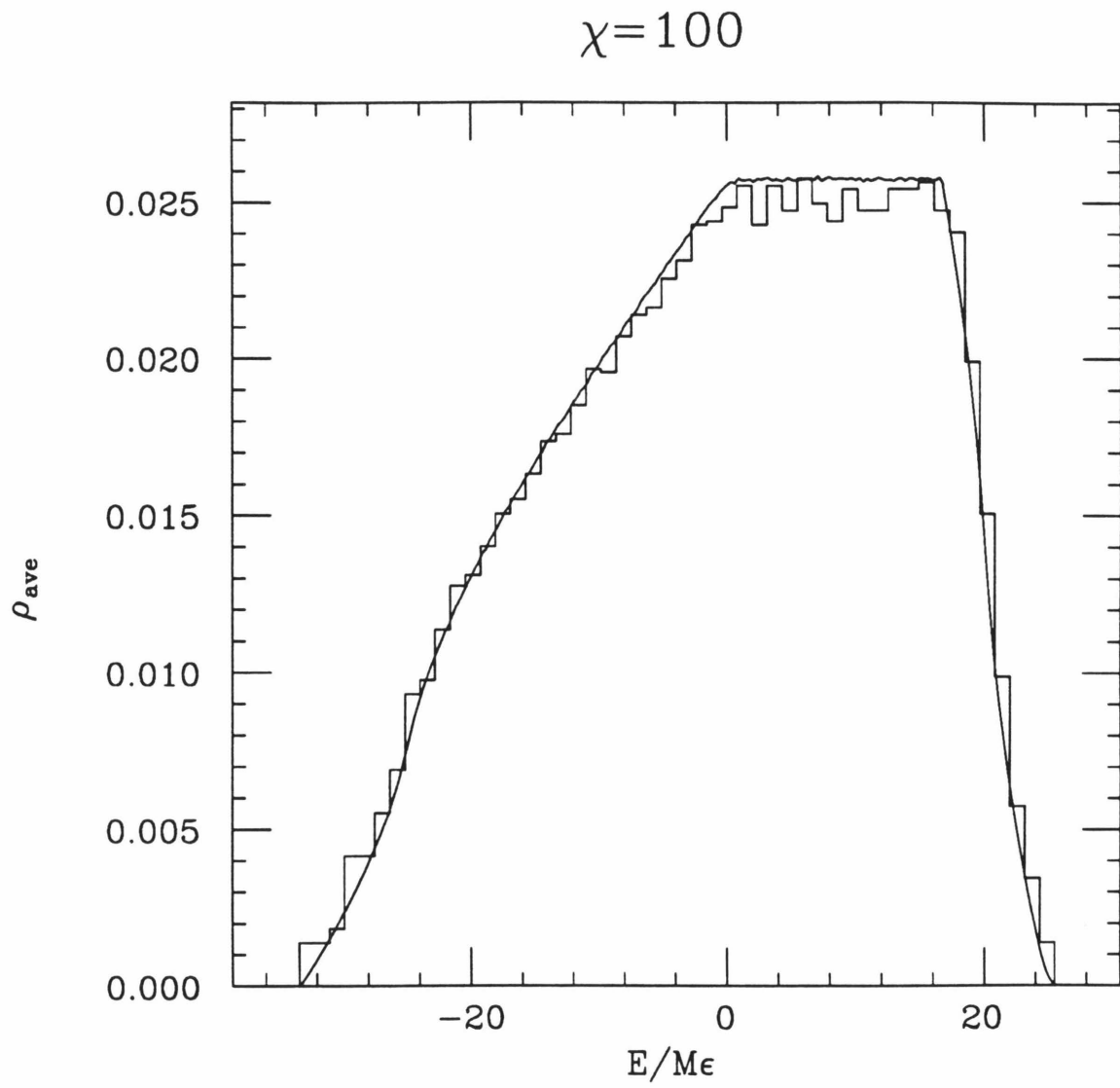


Figure 5.6

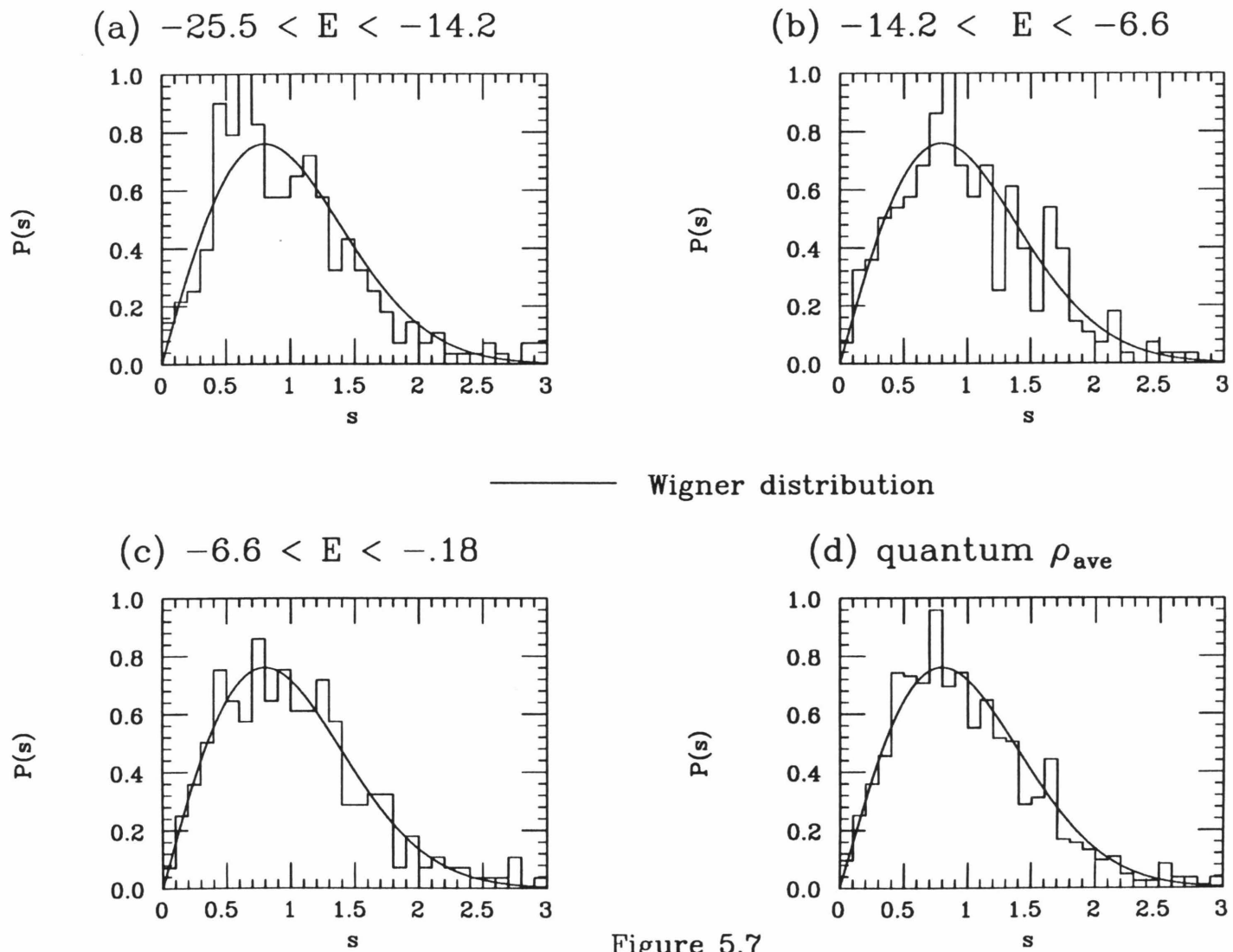
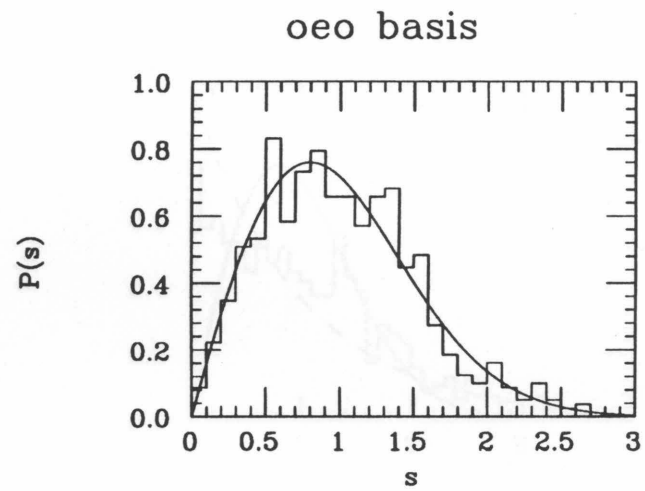
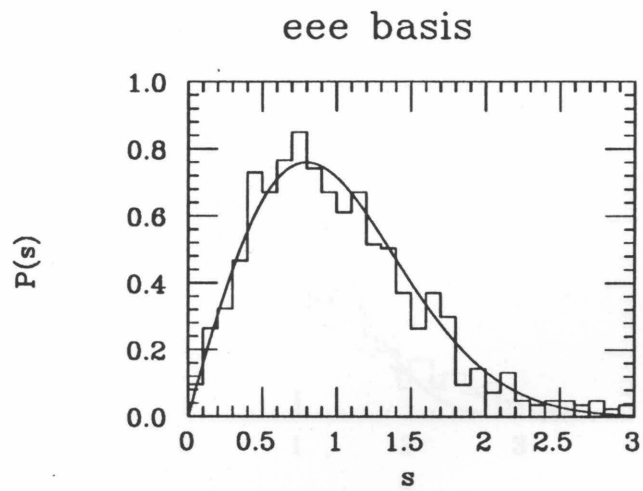


Figure 5.7



————— Wigner distribution

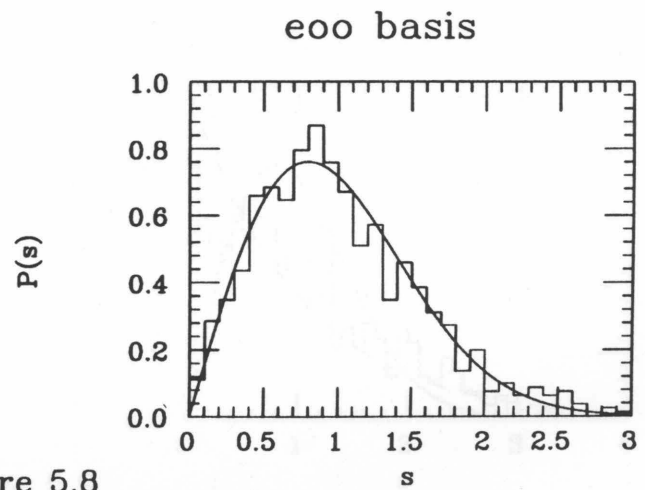
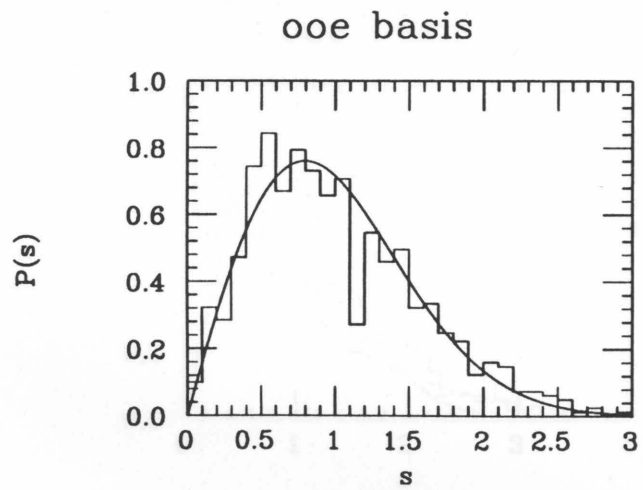


Figure 5.8

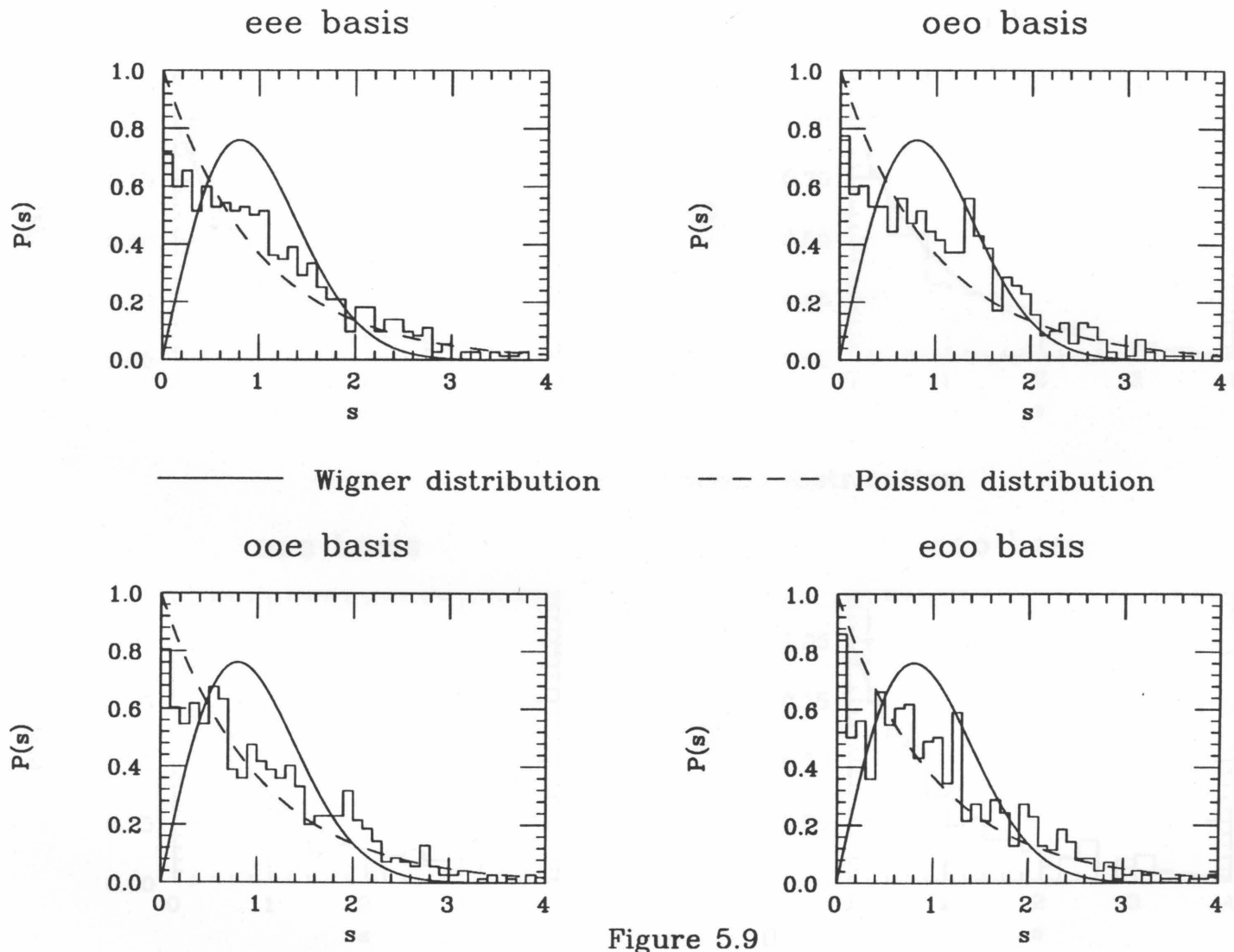
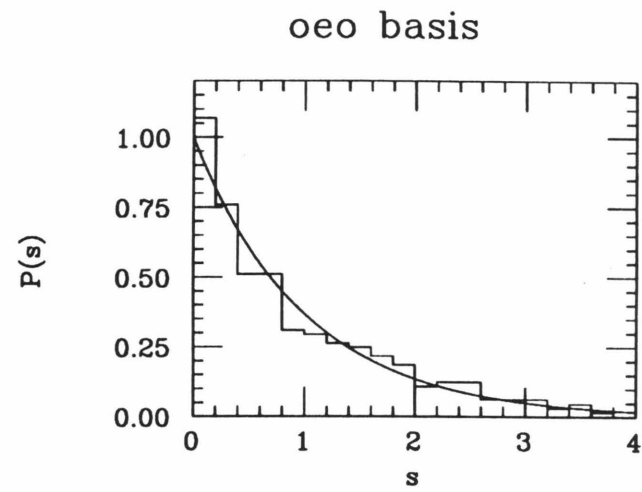
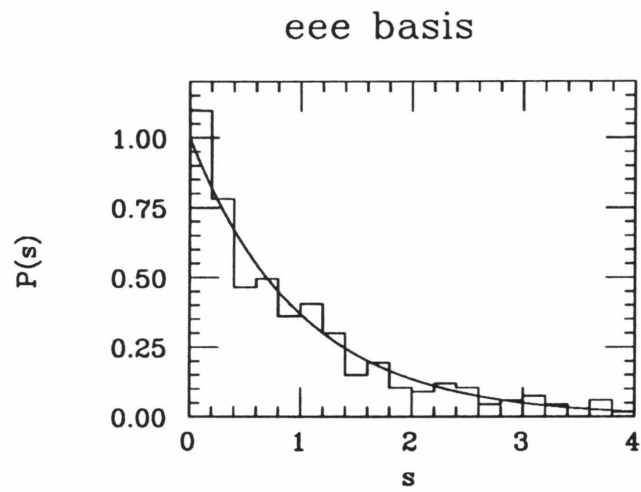


Figure 5.9



————— Poisson distribution

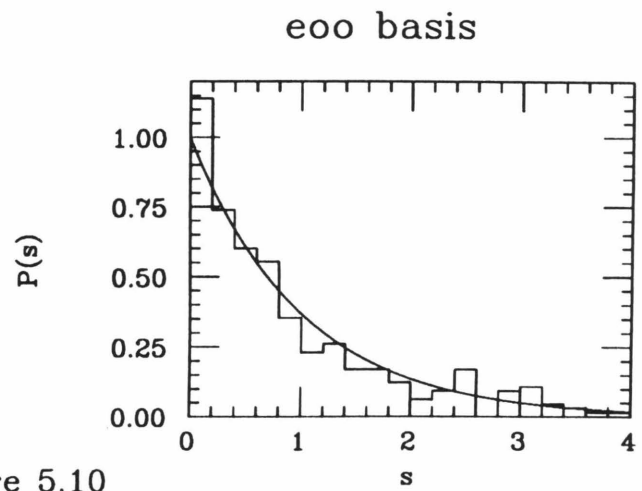
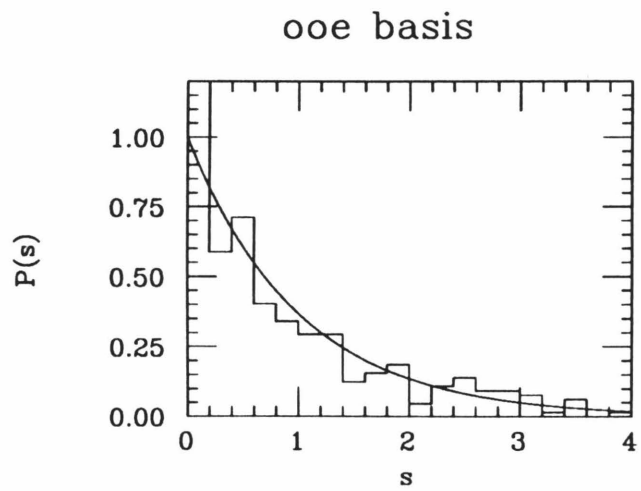


Figure 5.10

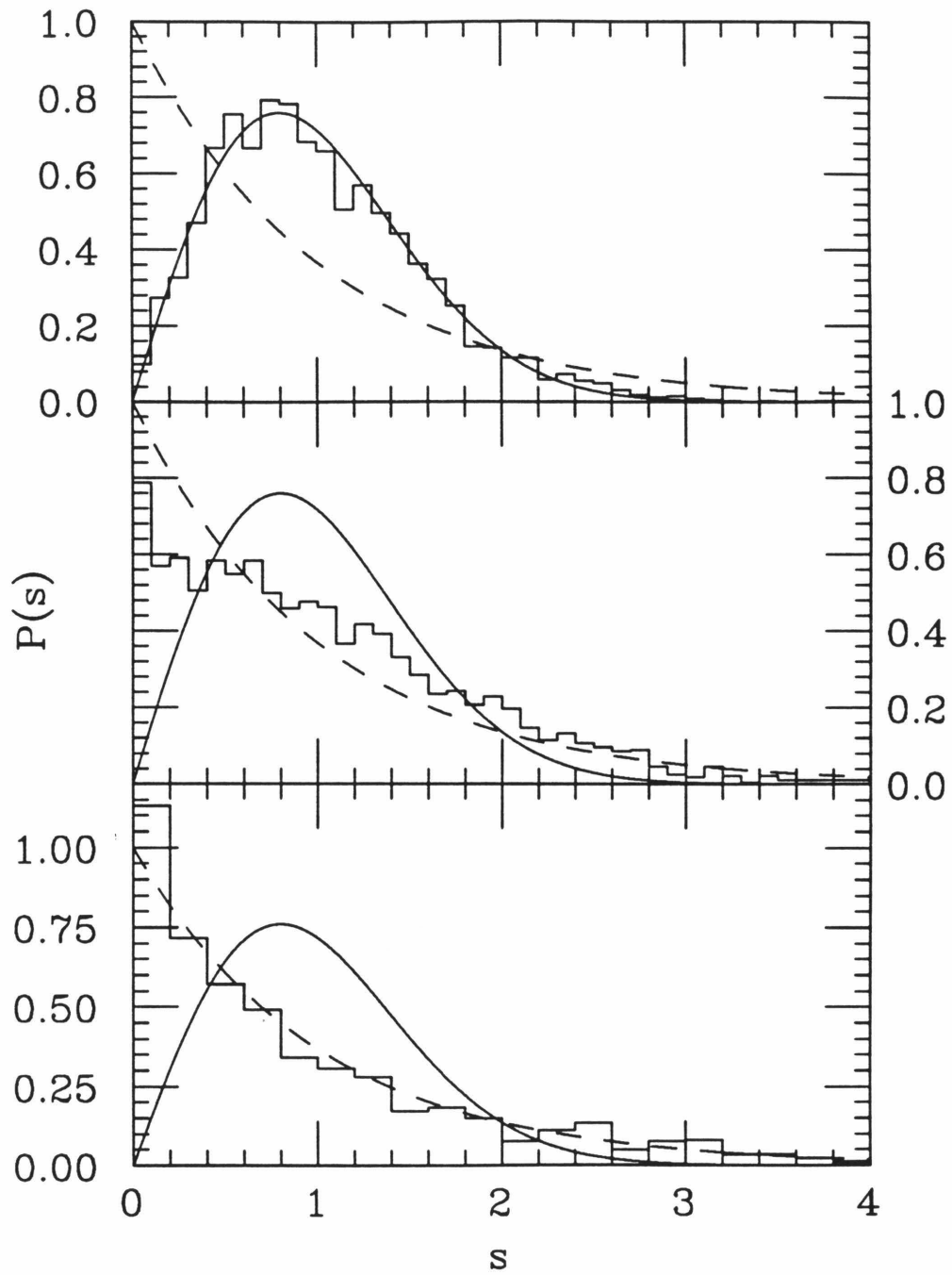


Figure 5.11

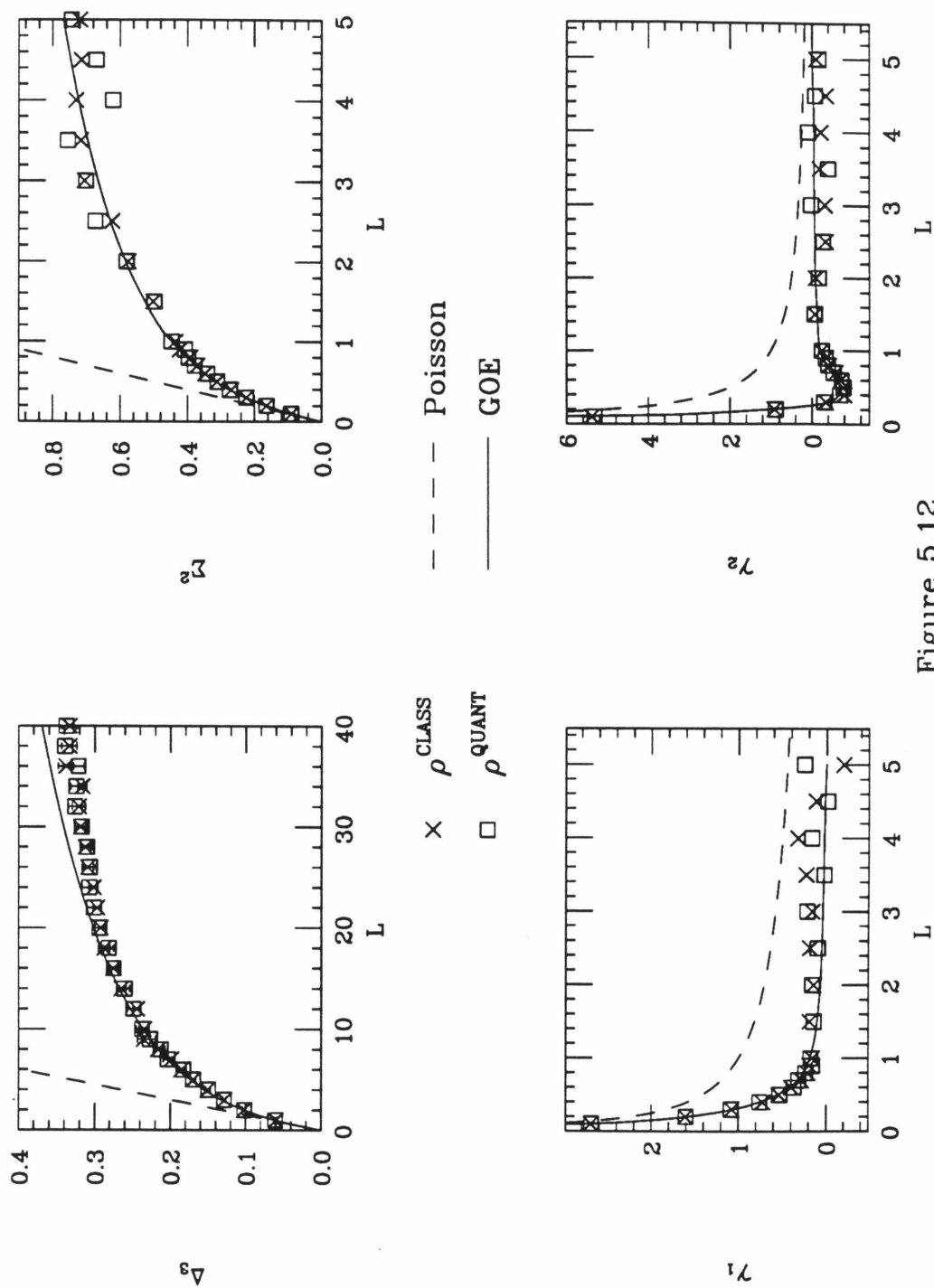
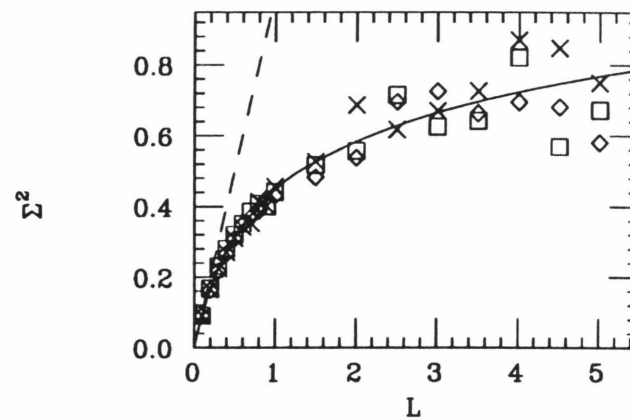
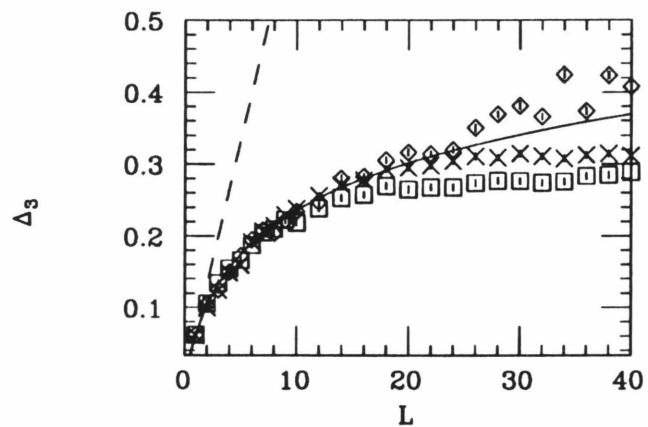


Figure 5.12



× $-25.2 < E < -14.2$
 ◇ $-14.2 < E < -6.6$

□ $-6.6 < E < -1.8$

- - - - - Poisson
 ——— GOE

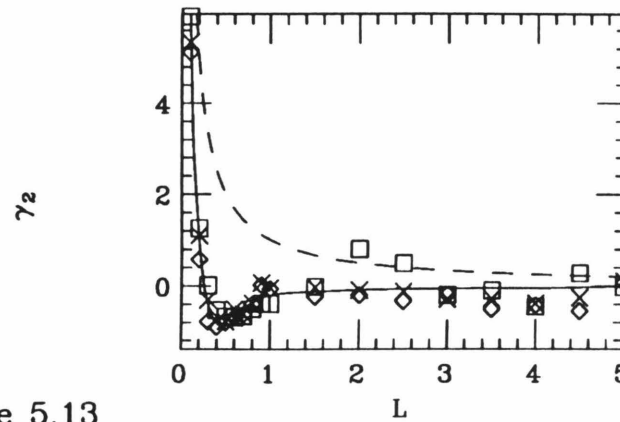
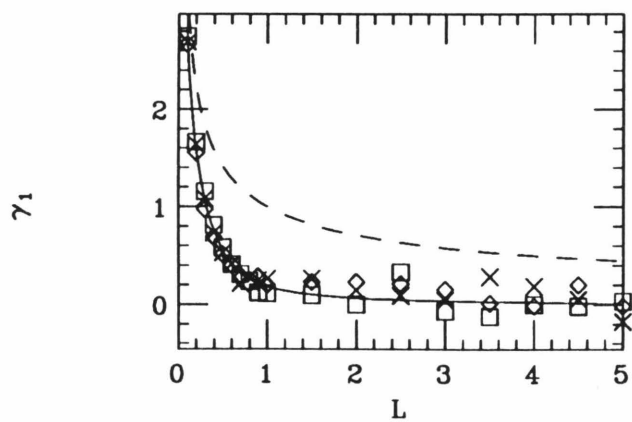
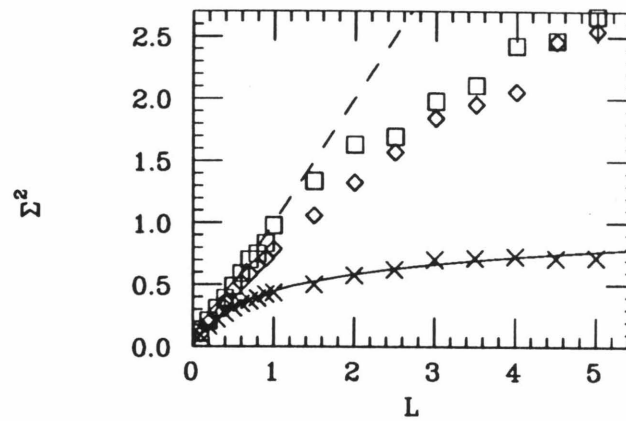
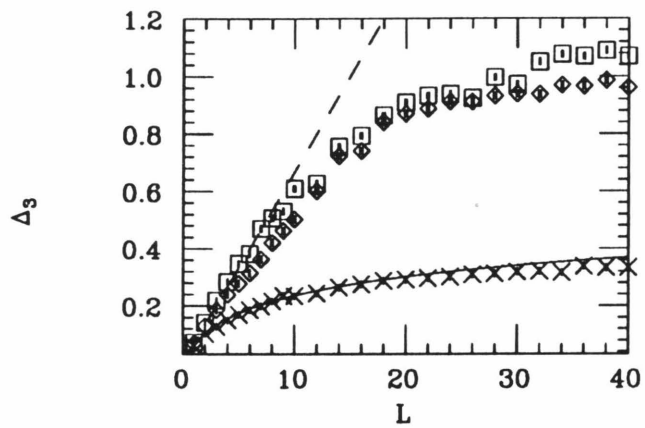


Figure 5.13



× chaotic
◇ quasi-chaotic

□ quasi-integrable

--- Poisson
— GOE

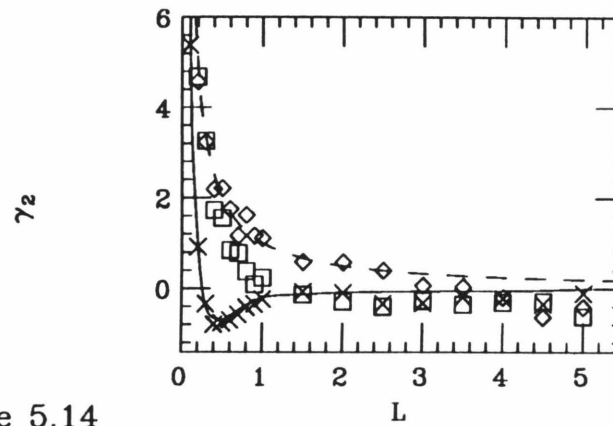
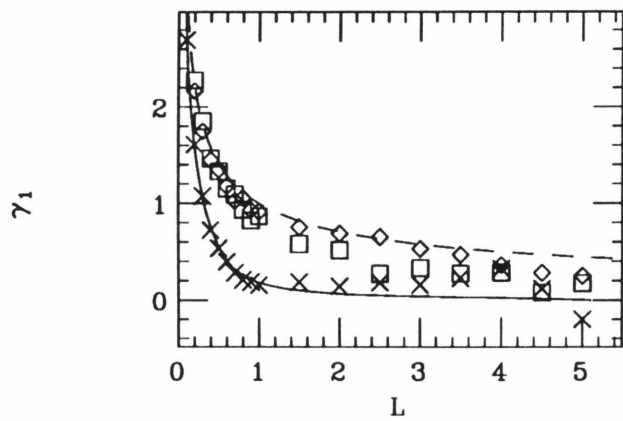
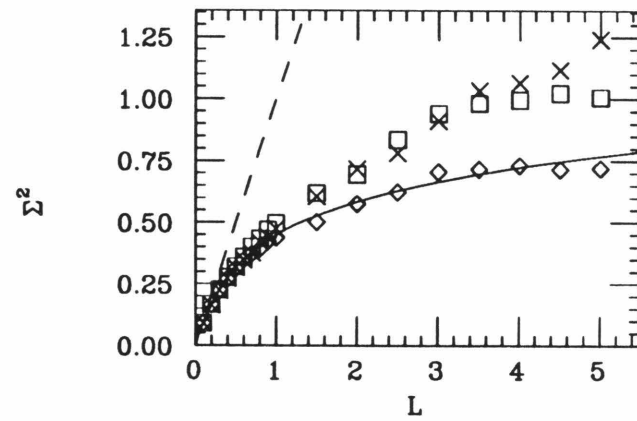
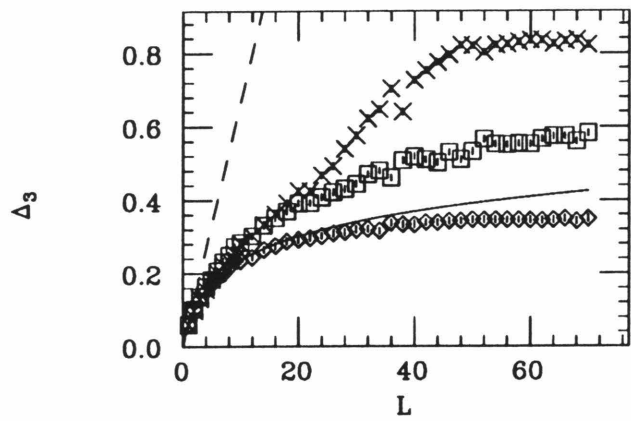


Figure 5.14



◇ oeo matrix
 × eee matrix

□ eeo matrix

--- Poisson
 — GOE

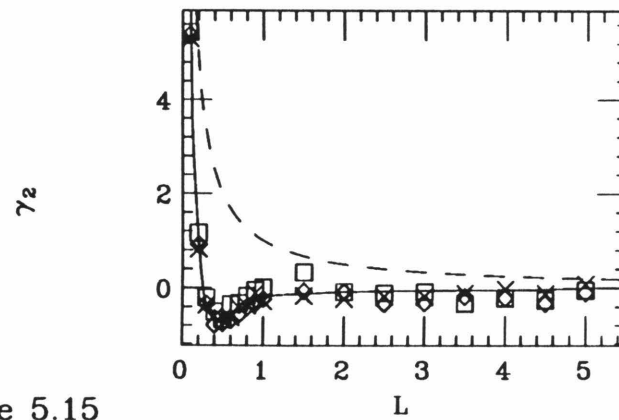
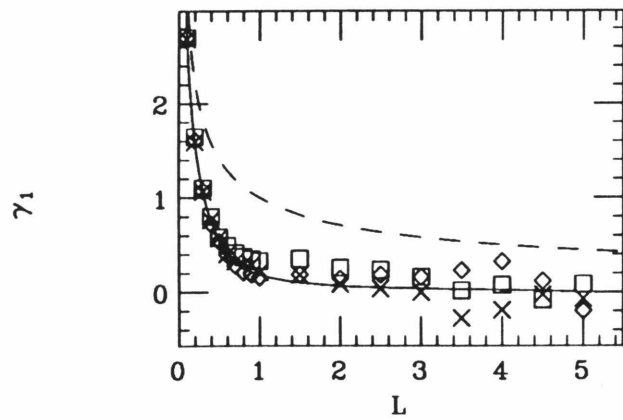


Figure 5.15

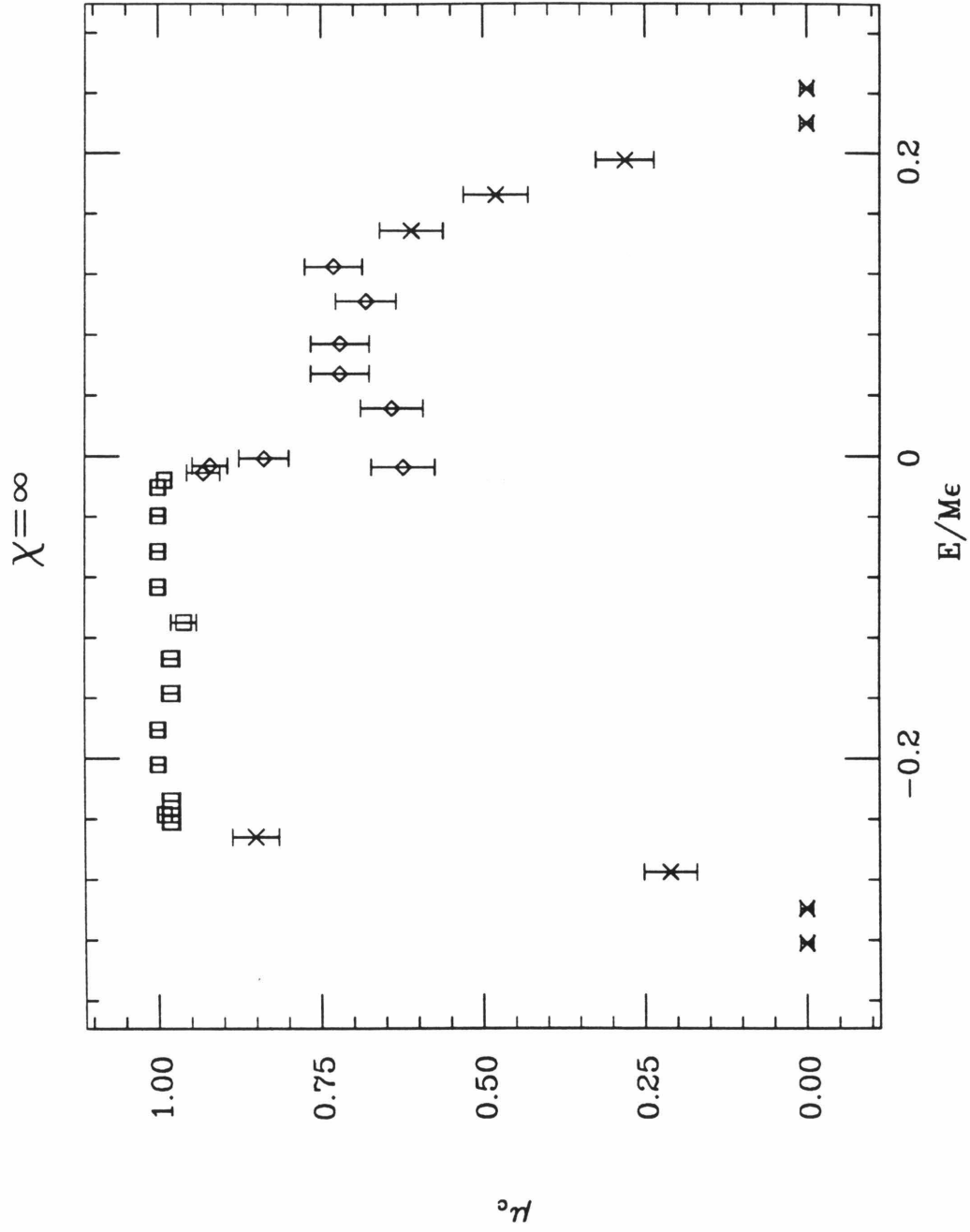
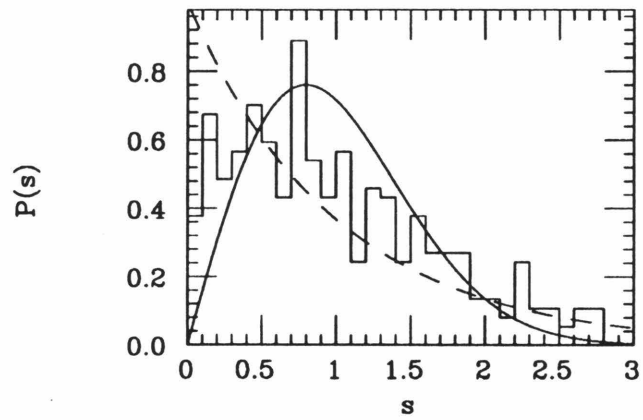
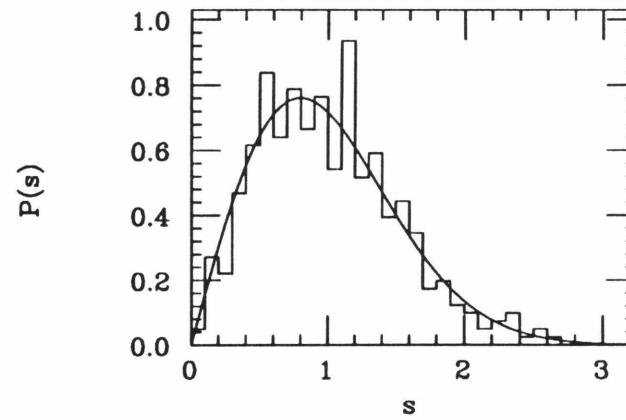


Figure 5.16

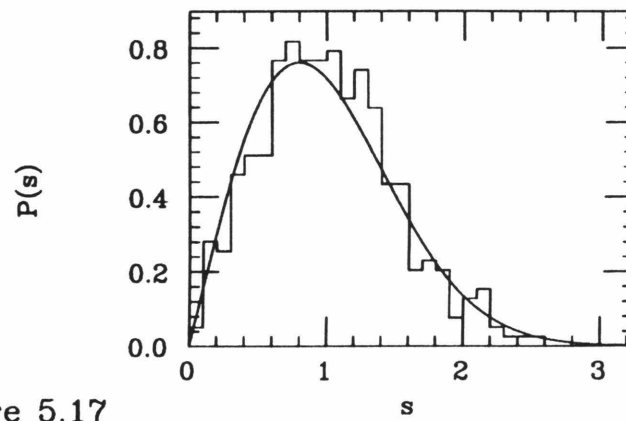
full basis, eoo matrix



symmetric basis



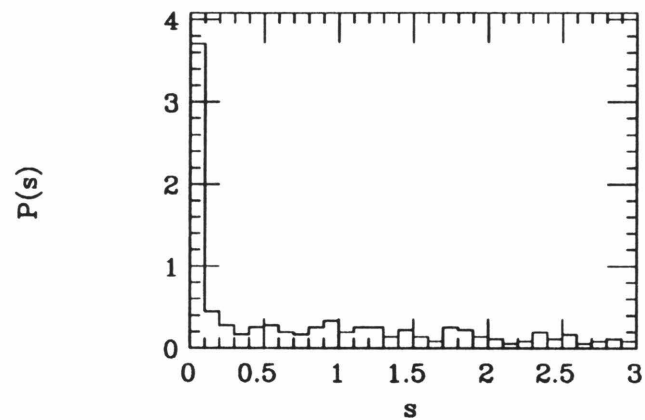
antisymmetric basis



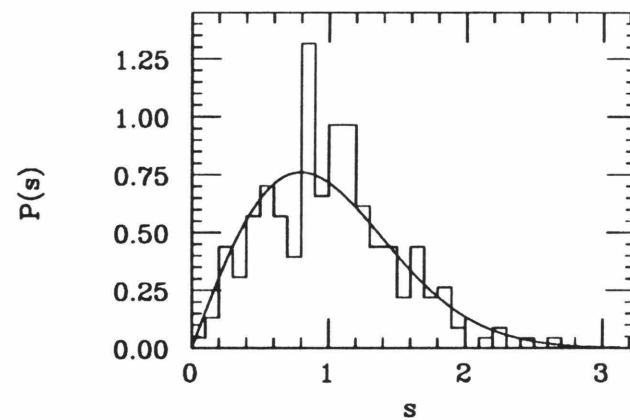
— Wigner Distribution
- - - Poisson Distribution

Figure 5.17

full basis, eee matrix

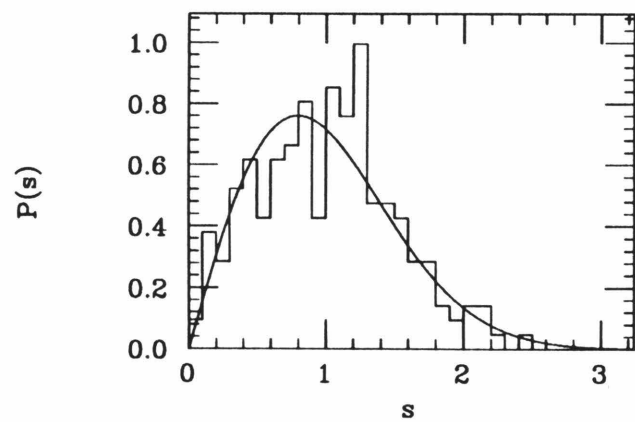


symmetric basis



————— Wigner distribution

antisymmetric basis



P_{01} symmetric basis

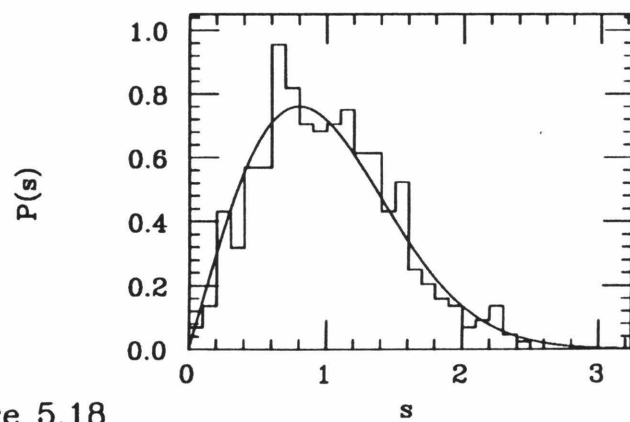
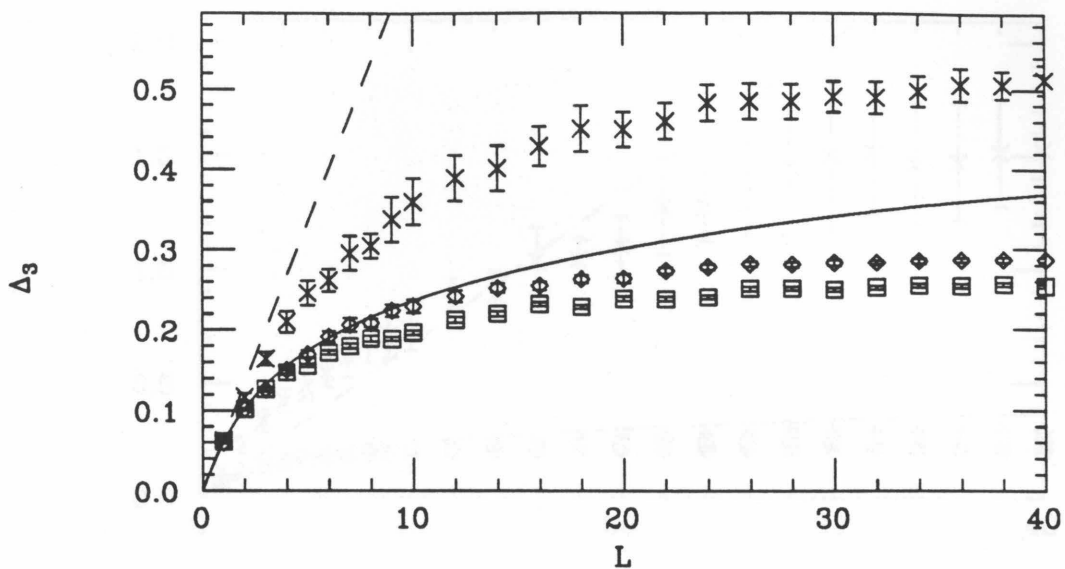


Figure 5.18

eoo basis



× full basis □ antisymmetric - - - Poisson
 ◇ symmetric — GOE

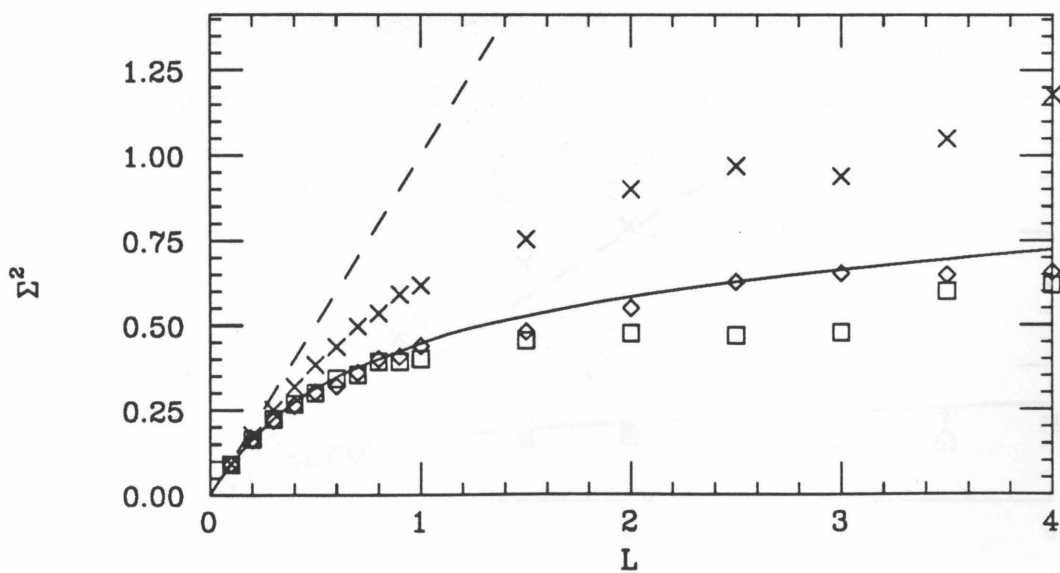


Figure 5.19

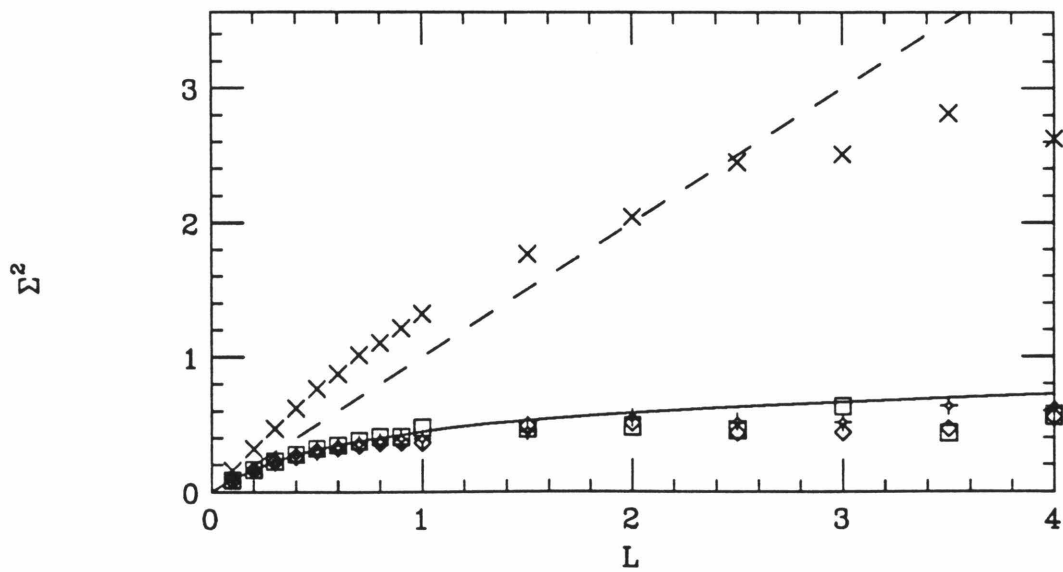
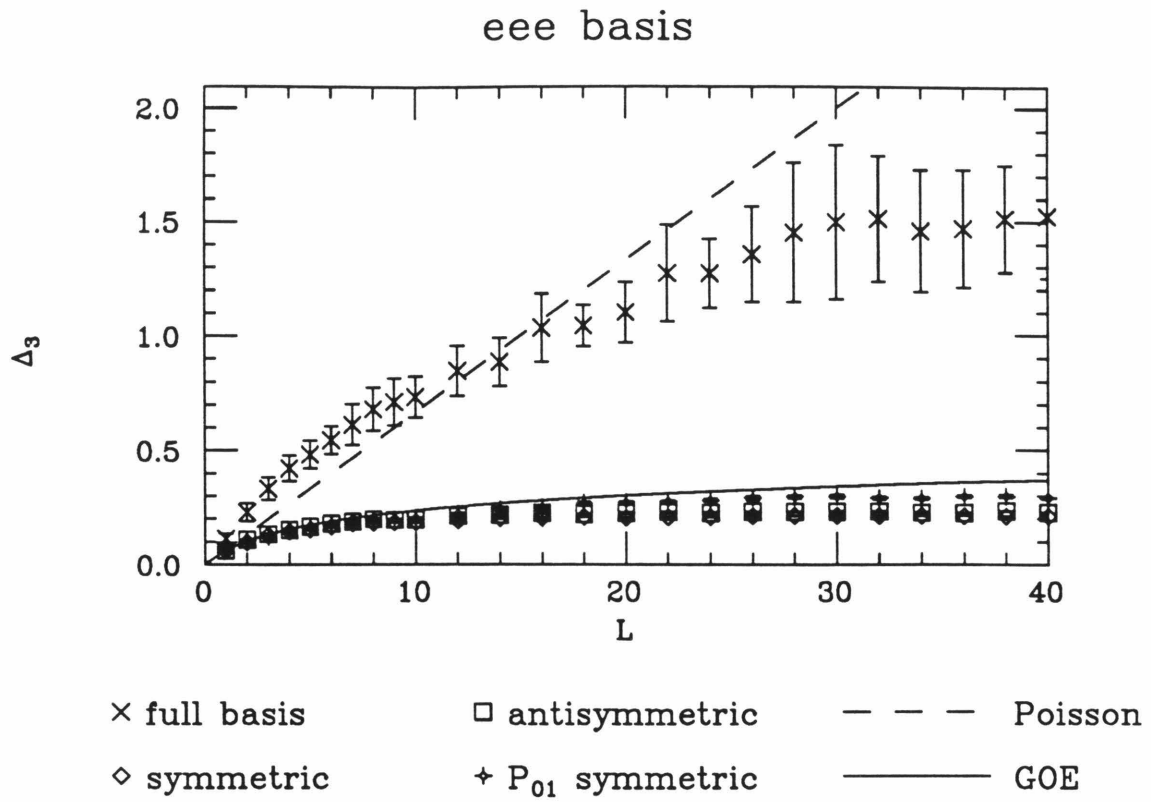


Figure 5.20

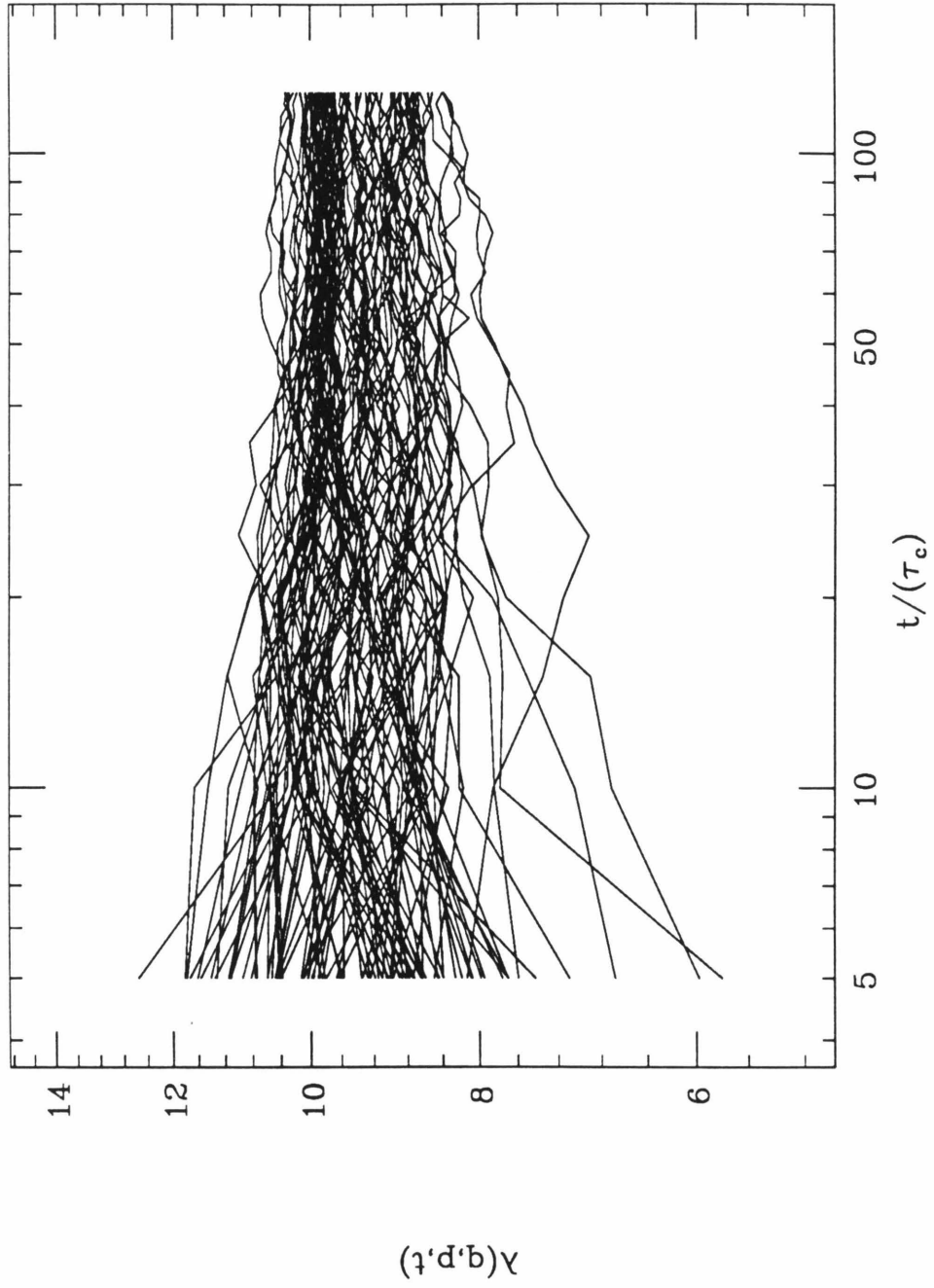


Figure 5.21

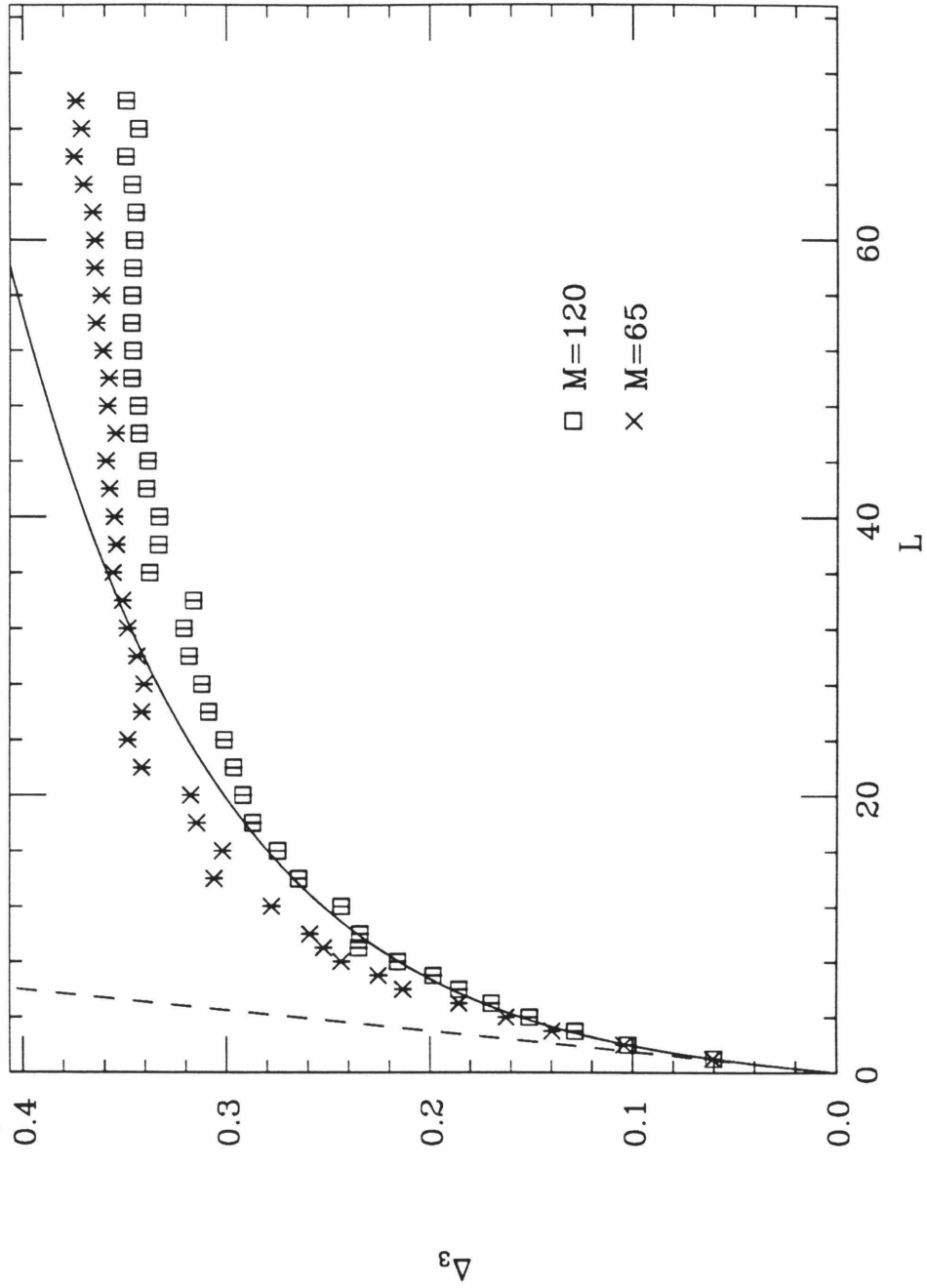


Figure 5.22

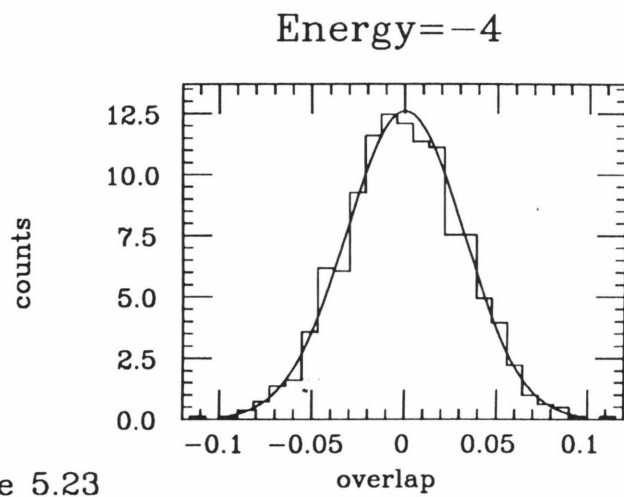
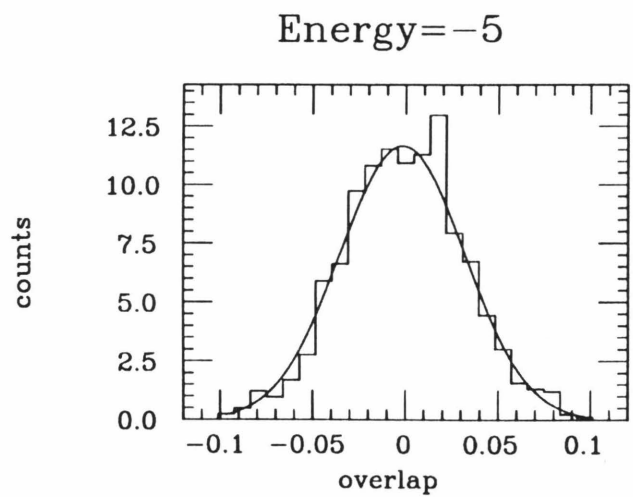
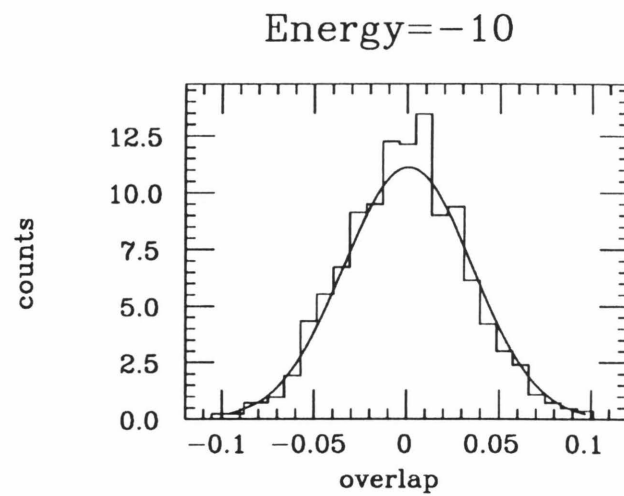
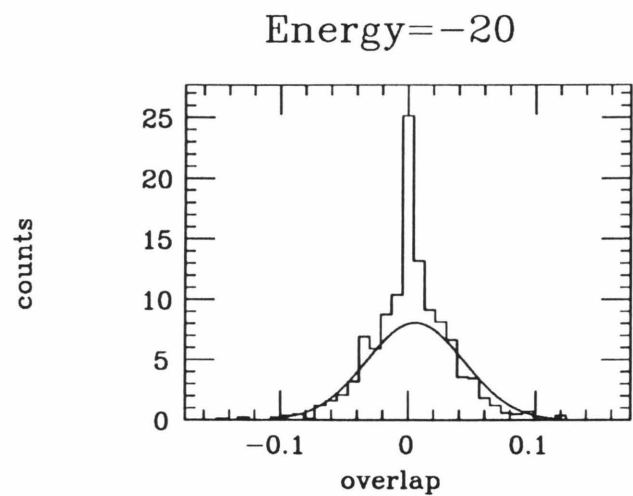


Figure 5.23

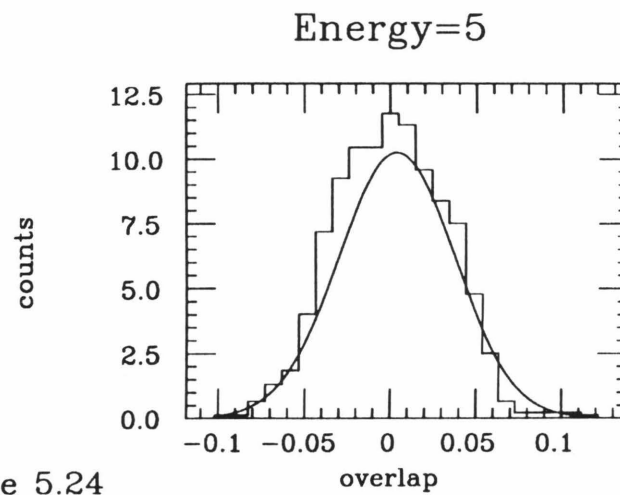
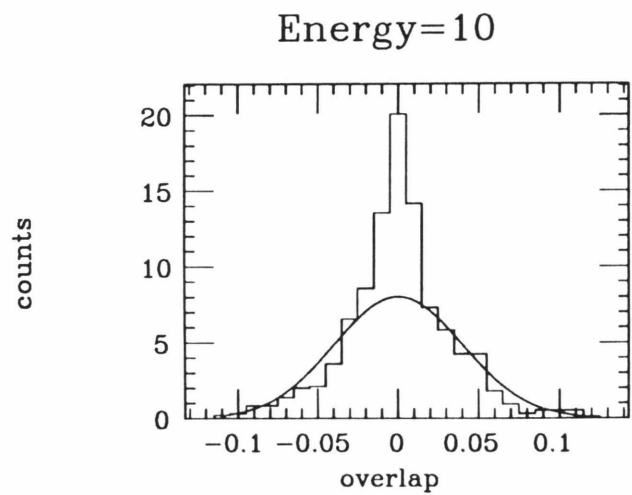
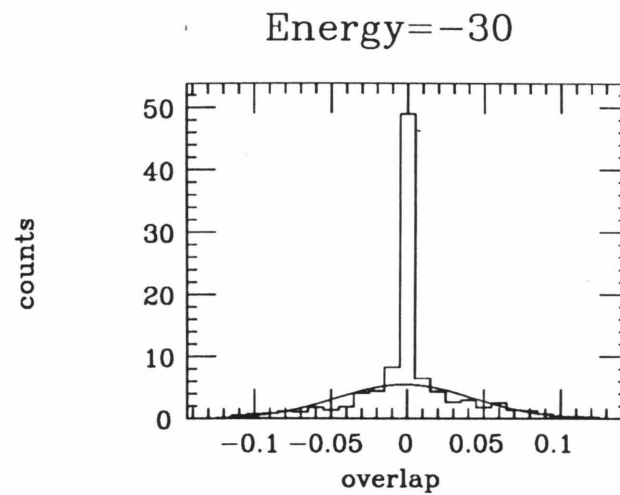
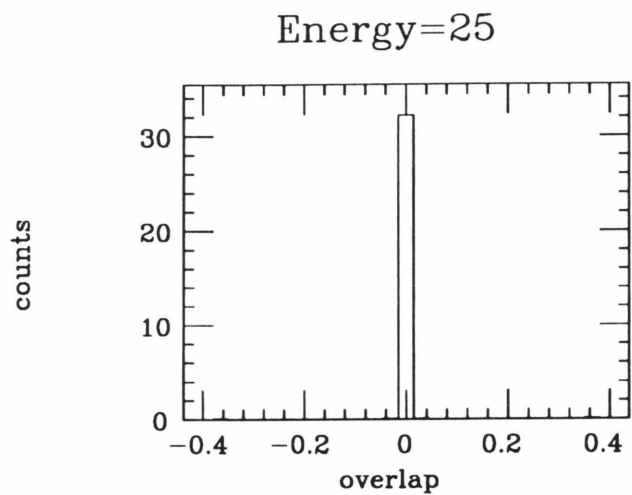
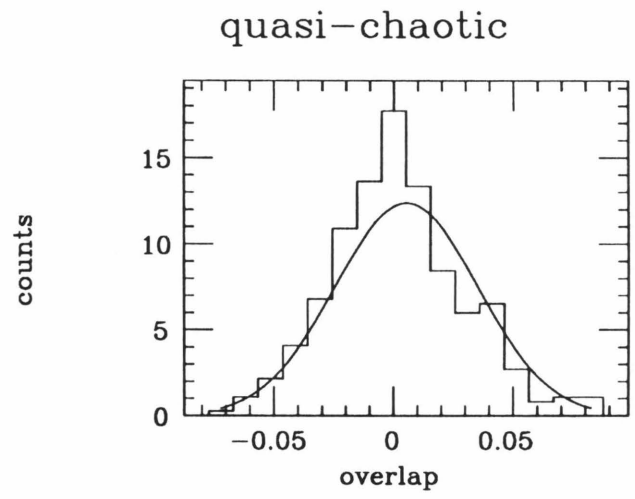
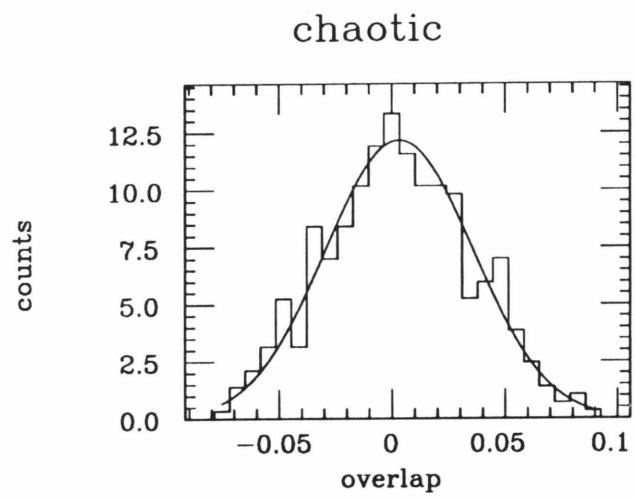


Figure 5.24



$\lambda=500$

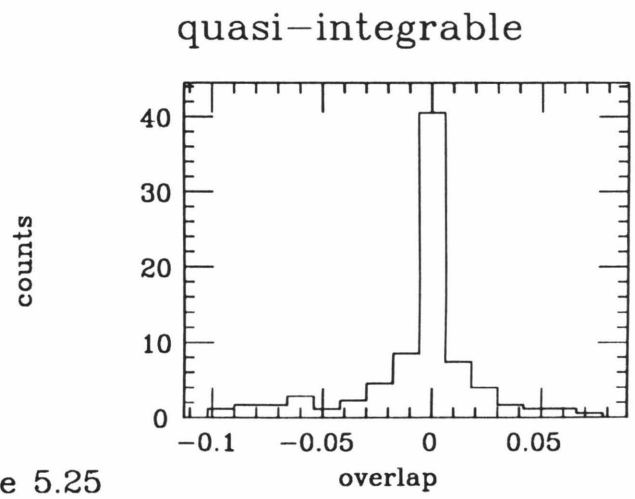
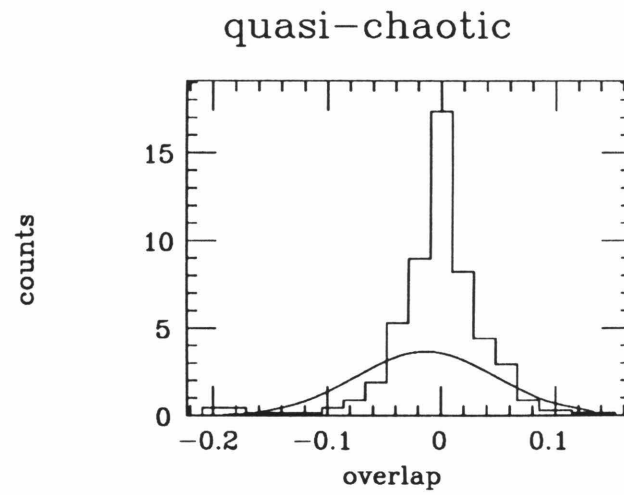
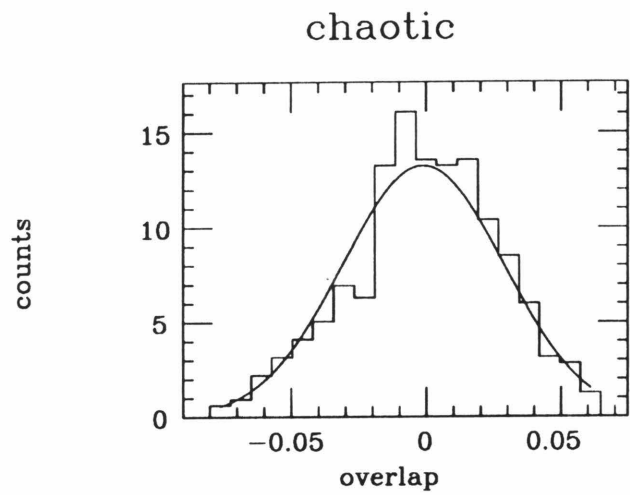


Figure 5.25



$\lambda=451$

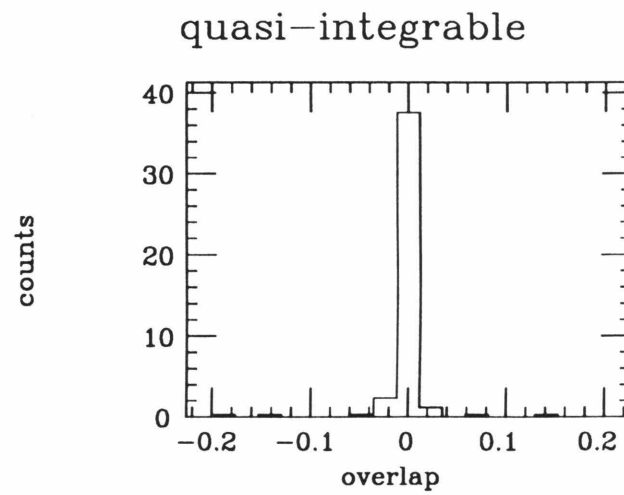
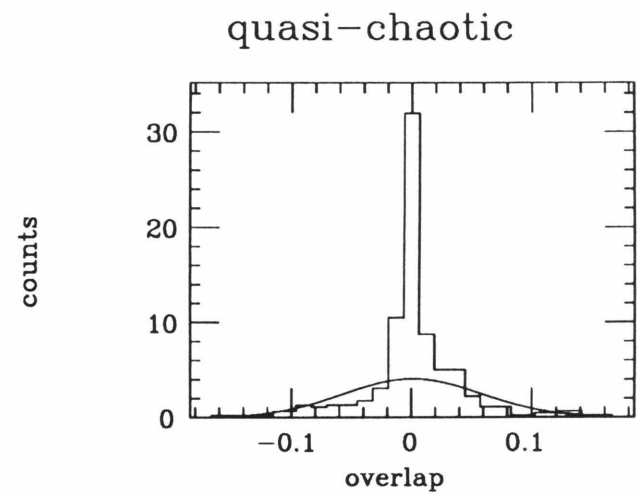
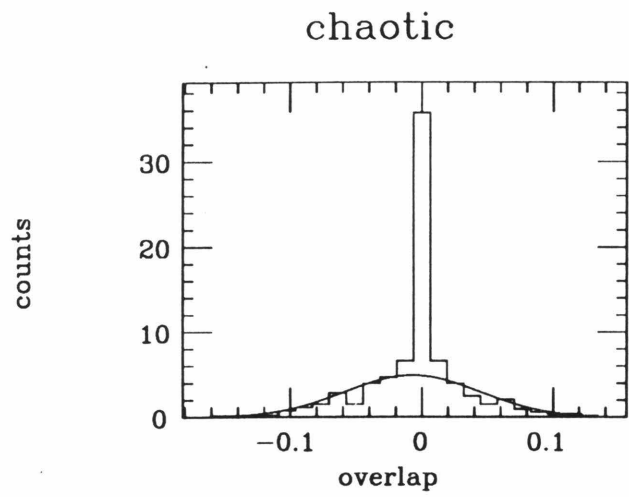


Figure 5.26



$\lambda=823$

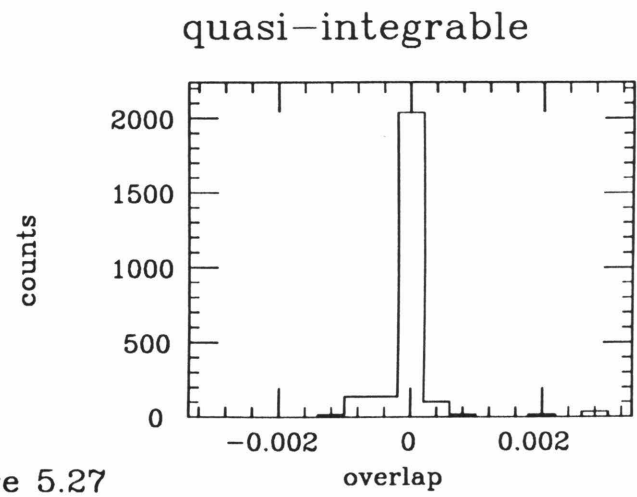
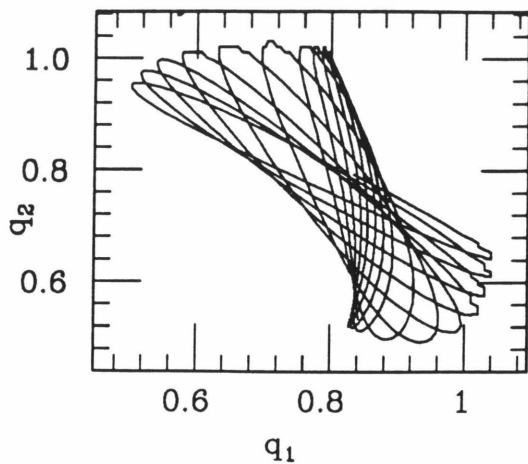
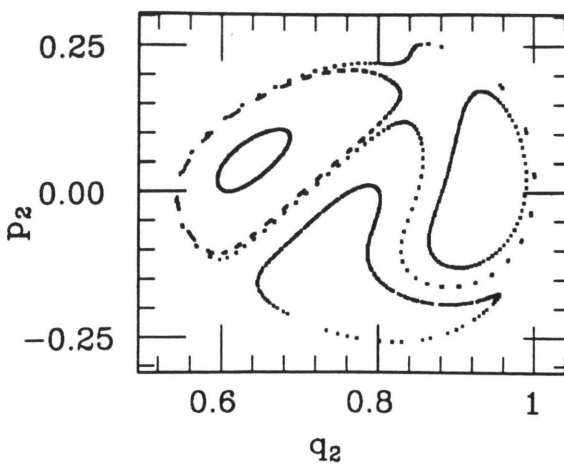


Figure 5.27

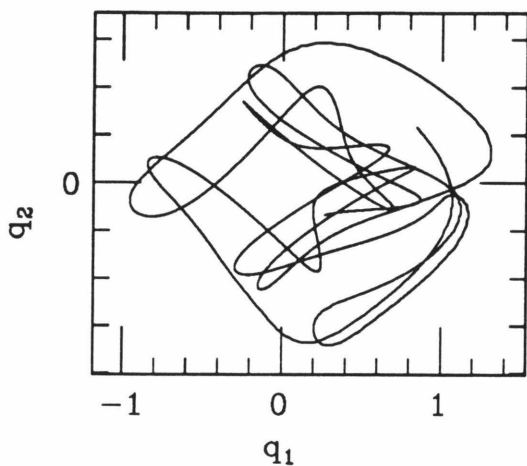
Energy = -30



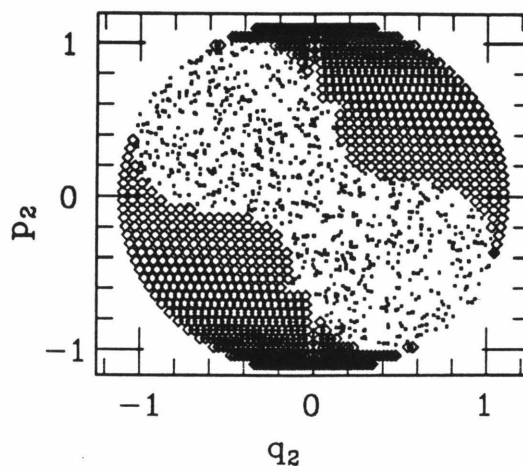
$q_1 = .8165$



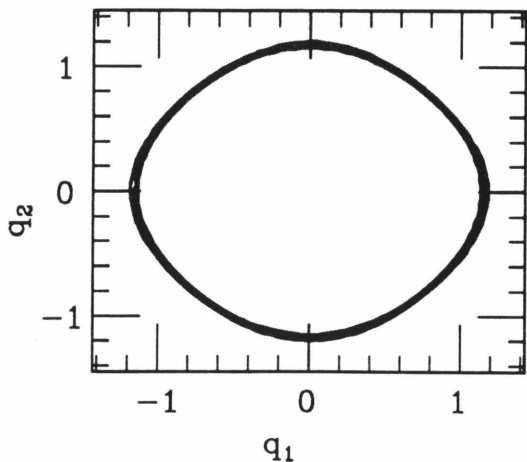
Energy = -2



$q_1 = .8165$



Energy = 10



$q_1 = .8165$

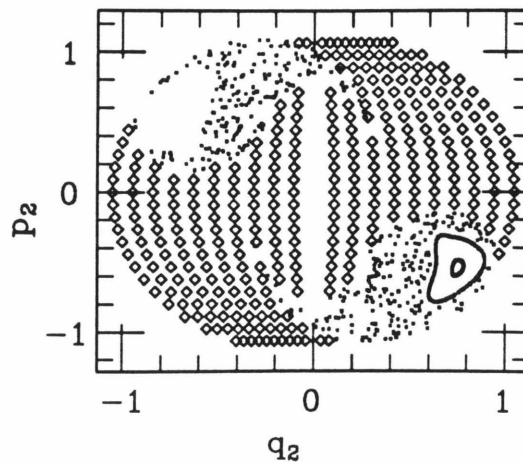


Figure 5.28

Chapter Six

Summary and Conclusions

There is a wide spectrum of dynamics for deterministic classical systems. The most regular motion is seen in integrable systems for which the number of conserved quantities equals the number of degrees of freedom ($\equiv N$). The trajectories in such a system lie on a single N dimensional torus in $2N$ dimensional phase space, and the time evolution on the tori is known in analytical form. Ergodic systems show less regular behavior. Such systems only conserve energy, and the trajectories cover the entire $2N - 1$ dimensional energy surface in phase space. Next in the hierarchy of irregularity are the chaotic systems, which are characterized by the stretching of phase space which gives rise to instability with respect to initial conditions. Finally, there are systems which are completely random, i.e., for which a series of measurements on the system yield uncorrelated results. Chapter I details the features of these different systems as well as the topology of their phase space.

These properties of classical chaotic systems have obvious implications for the corresponding quantum system. If only energy is conserved, a complete set of commuting observables does not exist; therefore, a complete set of quantum numbers cannot be assigned to each eigenstate. Also, the eigenvectors of nearly the same energy look very much the same since they both evenly cover the entire $2N - 1$ dimensional phase space. This is in sharp contrast to the integrable quantum systems which do have good quantum numbers. Also, for regular systems, two eigenvectors with nearly the same energy typically look very different in phase space because they have a very different set of quantum numbers. Therefore the features of spectra corresponding to regular and irregular classical motion must be different.

These differences are best seen in the fluctuations of the spectra. In Chapter II we studied Random Matrix Theories which offer a theory of spectral fluctuations based on ensembles of random matrices. The two ensembles which are most relevant to our study are the Poisson and Gaussian Orthogonal Ensembles (GOE): Poisson displays level clustering and spectral softness, while GOE displays level repulsion and spectral stiffness.

Chapter III gives some simple examples of the level fluctuations for quantum systems whose classical analogs are regular or irregular. Regular systems are well described by Poisson statistics, while chaotic systems are described by GOE statistics. Systems which are between regular and chaotic have statistics between Poisson and GOE. The success of RMT, both in chaology and in nuclear physics, have led to a hypothesis of the universality of level fluctuations: all chaotic quantum systems have GOE fluctuations; all regular systems have Poisson fluctuations. However, it is now clear that RMT do not give the whole picture. This is evidenced by the kink in the Δ_3 statistic which is not present in the RMT picture, but has been explained by semiclassical arguments.

Therefore quantum chaology is still in the years of “botany”, i.e., the collecting of examples to support or challenge our current understanding of the field. In this spirit, we have chosen a unique model to test ideas about quantum chaology: the three level Lipkin-Meshkov-Glick model. Its salient features are a compact Hilbert space and a classical analog with quartic momentum dependence. This model, its spectral fluctuations, and overlap distributions are the subject of Chapter V.

Our results are in good agreement with current ideas. When the classical analog is chaotic, the spectral statistics are in good agreement with GOE; when it is regular, the results are closer to Poisson. We also see the Δ_3 kink predicted by Berry. While it is well known that discrete symmetries destroy statistics, we found that partially conserved discrete symmetries can do so, too. The overlap distributions are in general agreement with GOE, showing near Gaussian results for the overlaps of

chaotic eigenvectors with fixed basis vectors, but narrower distributions for quasi-chaotic and quasi-integrable eigenvector overlaps. However, the results are not universal for the chaotic vectors, and this subject is still under investigation.

Throughout this paper, the term “chaos” has been applied to quantum systems whose classical analog is chaotic; what is lacking is a definition of quantum chaos which does not refer to classical dynamics, and which agrees with our common notions of chaos. If we define quantum chaos as level repulsion and spectral rigidity, this satisfies the first requirement, but it is not intuitively appealing: the rigid spectra of chaotic systems seem more ordered than the soft spectra of integrable systems. As another approach, we might try to carry over the definition of classical chaos, i.e., instability with respect to initial conditions. However, since the Schrödinger equation is linear, such instabilities cannot arise in quantum systems. This definition will not do either.

There are, however, some efforts to combine the body of evidence about spectral fluctuations with our intuitive notions of chaos. Casati, Guarneri, and Valz-Gris [CGV84] have made an attempt to show that eigenvalues of regular systems have zero complexity, while eigenvalues of irregular systems have positive complexity. (The algorithmic complexity of a string of numbers depends on the length of the program needed to calculate that string to a finite precision.) This work, therefore, links quantum chaos to complexity.

Also, there is some evidence that irregular quantum systems are more sensitive to perturbations. A recent paper by Feingold and Peres [FP85] used semiclassical methods to estimate the strengths $A_{ij} \equiv \langle i|A|j \rangle$ where i, j are eigenvectors of H and A is an operator. They showed that in the semiclassical limit $A_{ij} \gg |E_i - E_j|$ for chaotic systems, while for regular systems most $A_{ij} = 0$. If we consider A to be a perturbation to the Hamiltonian, this implies that the canonical perturbation expansion does not converge, and two close Hamiltonians have completely different eigenvalues and eigenvectors. Therefore quantum chaotic systems do have sensitive dependence, but this is dependence on Hamiltonian and not initial conditions.

The ideas of the last few paragraphs combine to give some intuitive notion of quantum chaos, parallel to the classical definition, but not dependent on it. The eigenvalues and eigenvectors are sensitive to perturbations, and are difficult to calculate (according to algorithmic complexity theory). Therefore solving an eigenvalue equation is difficult and of limited use since the results apply only to that Hamiltonian and can't be extended to other Hamiltonians by perturbation theory. This is analogous to the difficulty of calculating $x(t)$ for chaotic classical systems. Therefore, according to Weidenmüller [Wi84] the only reasonable way to describe a chaotic spectrum is to obtain the smooth density of states obtained from physics arguments and then to tack on the GOE fluctuations.

Appendix

The purpose of this Appendix is to show results for coherent states which are quoted in §5.2.

In order to calculate the classical Hamiltonian (5.2.5), we need some adeptness at calculating expectation values between the coherent states (5.2.2). First, we rewrite the coherent states

$$\begin{aligned}
 |\Phi(z)\rangle &\equiv \exp(z_1 G_{10} + z_2 G_{20}) |0\rangle \\
 &= \exp\left(\sum_{m=1}^M [z_1 a_{1m}^\dagger a_{0m} + z_2 a_{2m}^\dagger a_{0m}]\right) |0\rangle \\
 &= \prod_{m=1}^M \exp\left(z_1 a_{1m}^\dagger a_{0m} + z_2 a_{2m}^\dagger a_{0m}\right) |0\rangle \\
 &= \prod_{m=1}^M \left(1 + z_1 a_{1m}^\dagger a_{0m} + z_2 a_{2m}^\dagger a_{0m}\right) |0\rangle,
 \end{aligned}$$

where we have used the relations

$$\begin{aligned}
 a_{0m} a_{0m} |0\rangle &= 0 \\
 [a_{im}^\dagger a_{0m}, a_{jn}^\dagger a_{0n}] &= 0 \quad m \neq n.
 \end{aligned}$$

Then the vacuum state is substituted for the ground state

$$|0\rangle \equiv \prod_{m=1}^M a_{0m}^\dagger |-\rangle,$$

and using the relations

$$\begin{aligned}
 [a_{jm}^\dagger a_{0m}, a_{0n}^\dagger] &= 0 \quad m \neq n \quad j = 1, 2 \\
 a_{0n} a_{0n}^\dagger |-\rangle &= |-\rangle
 \end{aligned}$$

we obtain

$$|\Psi(z)\rangle = \prod_m^M \left(a_{0m}^\dagger + z_1 a_{1m}^\dagger + z_2 a_{2m}^\dagger\right) |-\rangle.$$

For ease of writing we define

$$C_m^\dagger(z) \equiv a_{0m}^\dagger + z_1 a_{1m}^\dagger + z_2 a_{2m}^\dagger .$$

Using this new form for $\Phi(z)$, we calculate the overlap of two states

$$\langle \Phi(\zeta) | \Phi(z) \rangle = \langle - | \prod_m C_m(\zeta) \prod_l C_l^\dagger(z) | - \rangle .$$

From Wick's Theorem [PB82], this may be rewritten in terms of all possible pairs of the C 's between the vacuum state, times all leftover terms normal ordered between the vacuum state. Normal ordering between the vacuum state will give zero, and the only pairs which survive are those which contract C_l with C_l^\dagger :

$$\begin{aligned} \langle \Phi(\zeta) | \Phi(z) \rangle &= \prod_l \langle - | C_l(\zeta) C_l^\dagger(z) | - \rangle \\ &= \prod_l (1 + \zeta_1^* z_1 + \zeta_2^* z_2) \\ &= (1 + \zeta_1^* z_1 + \zeta_2^* z_2)^M . \end{aligned} \tag{A.1}$$

The overall sign, which is determined by permutations of the C_l 's, is positive because of the symmetry of the ordering of the operators.

We also need to know the expectation value of the collective operators

$$G_{ij} \equiv \sum_m a_{im}^\dagger a_{jm} .$$

This is calculated as follows:

$$\begin{aligned} \langle \Psi(\zeta) | G_{ij} | \Psi(z) \rangle &= \sum_m \langle - | \prod_l C_l(\zeta) a_{im}^\dagger a_{jm} \prod_n C_n^\dagger(z) | - \rangle \\ &= \sum_m \prod_{l \neq m} \langle C_l(\zeta) C_l^\dagger(z) \rangle \langle C_m(\zeta) a_{im}^\dagger \rangle \langle a_{jm} C_m^\dagger(z) \rangle \\ &= \sum_m (1 + \zeta_1^* z_1 + \zeta_2^* z_2)^{M-1} \zeta_i^* z_j \\ &= M \zeta_i^* z_j (1 + \zeta_1^* z_1 + \zeta_2^* z_2)^{M-1} , \end{aligned}$$

with the understanding that $\zeta_0 = z_0 = 1$. If we use normalized states $\equiv |z\rangle$,

$$\langle z|G_{ij}|z\rangle = \frac{Mz_i^*z_j}{1 + |z_1|^2 + |z_2|^2}. \quad (A.2)$$

Using similar arguments

$$\langle z|G_{ij}G_{kl}|z\rangle = \frac{M(M-1)z_i^*z_k^*z_jz_l}{(1 + |z_1|^2 + |z_2|^2)^2}. \quad (A.3)$$

From these last two equations, we see that $\langle G_{ij}\rangle^2 = \langle G_{ij}^2\rangle$ for $M = \infty$, as claimed in 5.2.1, and that $\langle H/M\rangle$ is independent of M as claimed in the discussion about the action S .

We will now show that the overlap of different normalized coherent states vanish in the $M = \infty$ limit. We write

$$\begin{aligned} \frac{\langle \zeta|z\rangle}{\sqrt{\langle \zeta|\zeta\rangle\langle z|z\rangle}} &= \frac{\left(\sum_{j=0}^2 \zeta_j^* z_j\right)^M}{\left(\sum |\zeta_j|^2 \sum |z_j|^2\right)^{M/2}} \\ &= \left[\frac{\sum \zeta_j^* z_j}{\sqrt{\sum |\zeta_j|^2 \sum |z_j|^2}} \right]^M. \end{aligned}$$

Changing variables

$$\zeta_j = \rho_j e^{i\phi_j} \quad z_j = r_j e^{i\theta_j} \quad \Delta_j = \theta_j - \phi_j,$$

we may rewrite the overlap

$$\begin{aligned} &= \left[\frac{\sum \rho_j r_j e^{i\Delta_j}}{\sum \rho_j^2 r_k^2} \right]^M \\ &= \eta^M e^{iM\psi}, \end{aligned}$$

where η is the modulus of the numerator divided by the modulus of the denominator, and ψ is the phase of the numerator. If $\eta < 1$ then the overlap vanishes as $M \rightarrow \infty$.

The moduli are written

$$\begin{aligned} m_{\text{num}} &\equiv \sum_{jk} \rho_j \rho_k r_j r_k e^{i(\Delta_j - \Delta_k)} \\ m_{\text{den}} &\equiv \sum_{jk} \rho_j^2 r_k^2. \end{aligned}$$

When $k = j$ the terms in m_{num} and m_{den} are equal, and may be ignored in the comparison of the moduli, leaving for the numerator

$$\sum_{j < k} 2\rho_j \rho_k r_j r_k \cos(\Delta_j - \Delta_k) ,$$

and for denominator

$$\sum_{j < k} (\rho_j r_k + \rho_k r_j) .$$

If we consider $\rho_j r_k \equiv y$ and $\rho_k r_j \equiv x$ as two sides of a triangle, with an angle $\Delta_j - \Delta_k$ in between, we may invoke the law of cosines to compare the moduli. Since

$$2xy \cos(\Delta_j - \Delta_k) = x^2 + y^2 - z^2$$

and $z^2 > 0$, the modulus of the denominator is larger, $\eta < 1$, and the overlap vanishes in the $M = \infty$ limit. This also holds if $\Delta_j = \Delta_k$ and $\rho_k \neq r_k$, although a slightly different approach must be used. If $\Delta_j = \Delta_k$ and $\rho_k = r_k$, then $\eta = 1$ and $\psi = 0$ and the overlap is unity as we'd expect when $\zeta = z$.

Now we turn to the completeness relation for the coherent states. We will not give a proof, but only make the answer plausible. Starting from the result of Blaizot and Orland [BO81] for coherent states with $M = 1$, we guess a result of the form

$$1 = \int C \frac{dz_1 dz_2 dz_1^* dz_2^* |z\rangle \langle z|}{(1 + |z_1|^2 + |z_2|^2)^l} .$$

C and l will be determined from requiring that

$$\langle k|k\rangle = 1 = \int d\mu(z) |\langle k|z\rangle|^2 ,$$

where $d\mu(z)$ is the measure given above and $|k\rangle$ is a normalized state. If we choose

$$|k_1\rangle \equiv |0\rangle ,$$

i.e., the non-interacting ground state, then

$$\langle 0|z\rangle = 1 .$$

The integral is easily evaluated by changing to polar coordinates, and we obtain

$$C = \frac{(l-1)(l-2)}{4\pi}.$$

To determine l , we choose

$$|k_2\rangle \equiv \frac{G_{10}|0\rangle}{\sqrt{M}},$$

and the overlap is now

$$\langle k_2|z\rangle = \sqrt{M}z_1.$$

The elementary integrals give

$$l = M + 3.$$

Putting this altogether, we have

$$1 = \int (M+1)(M+2) \frac{dz_1 dz_2 dz_1^* dz_2^* |z\rangle \langle z|}{(1 + |z_1|^2 + |z_2|^2)^{M+3}}. \quad (\text{A.4})$$

As a check, $\langle k_1|k_2\rangle$ should equal zero when the completeness relation is inserted between the two states. Indeed, the angular integral give zero:

$$\int_0^{2\pi} d\phi e^{i\phi} = 0.$$

Therefore these orthogonal state are still orthogonal, and the completeness relation passes the test.

References

- AL86 Y. Alhassid and R.D. Levine, *Phys. Rev. Lett.* **57**, 2879 (1986).
- Ar78 V.I. Arnold, *Mathematical Methods of Classical Mechanics* (Springer Verlag, New York, 1978).
- Ba68 R. Balian, *Nuovo Cimento* **B57**, 183 (1968).
- Be78 M.V. Berry, in *Topics in Nonlinear Dynamics, a Tribute to Sir Edward Bullard*, edited by S. Jorna (American Institute of Physics, New York, 1978).
- Be77 M.V. Berry, *J. Phys. A* **10** 2083, (1977).
- Be81 M.V. Berry, *Ann. Phys.* **131**, 163 (1981).
- Be85 M.V. Berry, *Proc. R. Soc. Lond. A* **400**, 229 (1985).
- BG75 O. Bohigas and M.-J. Giannoni, *Ann. Phys.* **89**, 393 (1975)
- BG83 O. Bohigas and M.-J. Giannoni, in *Mathematical and Computational Methods in Nuclear Physics*, Granada, Spain, edited by J.S. Dehesa, J.M.G. Gomez, and A. Polls (Springer-Verlag, Berlin, 1983).
- BGS76 G. Benettin, L. Galgani, J.-M. Strelcyn, *Phys. Rev. A* **14**, 2338 (1976).
- BGS84 O. Bohigas, M.-J. Giannoni, and C. Schmit, *Phys. Rev. Lett.* **52**, 1 (1984).
- BH76 H.P. Baltes and E.R. Hilf, *Spectra of Finite Systems* (Wissenschaftsverlag, Mannheim, 1976).
- BHP85 O. Bohigas, R.U. Haq, A. Pandey, *Phys. Rev. Lett.* **54** 1645 (1985).
- BO80 J.P. Blaizot and H. Orland, *Phys. Rev. C* **24**, 1740 (1981).
- Br76 T.A. Brody, E. Cota, and J. Flores, *Nucl. Phys A* **259**, 87 (1976).
- Br81 T.A. Brody, J. Flores, J.B. French, P.A. Mello, A. Pandey, and S.S.M. Wong, *Rev. Mod. Phys.* **53**, 385 (1981).

- BR84 M.V. Berry and M. Robnik, *J. Phys.* **A17**, 2413 (1984).
- BT77 M.V. Berry and M. Tabor, *Proc R. Soc. Lond.* **A 365**, 375 (1977).
- Ca85 G. Casati, editor *Chaotic Behavior in Quantum Systems* (Plenum Press, New York 1985).
- CCG85 G. Casati, B. Chirikov, and I. Guarneri, *Phys. Rev. Lett* **54**, 1350 (1985).
- CF79 G. Casati and J. Ford, editors, *Stochastic Behavior in Classical and Quantum Hamiltonian Systems* (Springer-Verlag, Berlin, 1979).
- CGV84 G. Casati, I. Guarneri, and F. Valz-Gris, *Phys. Rev.* **A 30**, 1586 (1984).
- CVG80 G. Casati, F. Valz-Gris, and I. Guarneri, *Lett. Nuovo Cim.* **28** 279 (1980).
- DFW77 J.P. Draayer, J.B. French, and S.S.M. Wong, *Ann. Phys.* **106**, 472, 503 (1977).
- DM63 F.J. Dyson and M.L. Mehta, *J. Math. Phys.* **4**, 701 (1963).
- Dy62 F.J. Dyson, *J. Math. Phys.* **3**, 140 (1962).
- ER85 J.-P. Eckmann and D. Ruelle, *Rev. Mod. Phys.* **57**, 617 (1985).
- Fl80 B. Flanders, Ph.D. Thesis, Caltech, 1980.
- FM73 J. Flores and P.A. Mello, *Rev. Mex. Fis.* **22**, 185 (1973).
- FP86 M. Feingold and A. Peres, *Phys. Rev.* **A 34**, 591 (1986).
- FS57 K.O. Friedrichs and H.N. Shapiro, in *New York University-Courant Institute Lecture Notes* (unpublished, 1957).
- FST73 J. Ford, D. Stoddard, and J.S. Turner, *Prog. Theor. Phys.* **50**, 1547 (1973).
- Ga61 M. Gaudin, *Nucl. Phys.* **25**, 447 (1961).
- Gu66 F. Gustavson, *Astron. J.* **21**, 670 (1966).
- Gu67 M.C. Gutzwiller, *J. Math. Phys.* **8**, 1979 (1967); *J. Math. Phys.* **10**, 1004 (1969); *J. Math. Phys.* **11**, 1791 (1970); *J. Math. Phys.* **12**, 343 (1971).

- He80 R.H.G. Helleman, in *Fundamental Problems in Statistical Mechanics*, volume 5, edited by E.G.D. Cohen (North Holland Publishing, Amsterdam, 1980).
- He74 M.Henon, Phys. Rev. **B9**, 1925 (1974).
- HH64 M Henon and C. Heiles, Astron. Journ. **69**, 55 (1977).
- HPB82 R.U. Haq, A. Pandey and O. Bohigas, Phys. Rev. Lett. **48**, 1086 (1982).
- Ka79 K.-K. Kan, J.J. Griffin, P.C. Lichtner, and M. Dworzecka, Nucl. Phys. **A332**, 109 (1979).
- Ka 81 K.-K. Kan, Phys. Rev. **A24**, 2831 (1981).
- Li72 H.I. Liou, H.S. Camarada, S. Wynchank, M. Salgowitz, G. Hacken, F. Rahn, and J. Rainwater, Phys. Rev. **C5**, 974, (1972).
- LL83 A.J. Lichtenberg and M.A. Lieberman *Regular and Stochastic Motion*, (Springer Verlag, New York 1983).
- LMG65 H. Lipkin, N.Meshkov, and A.J. Glick, Nucl. Phys. **62**, 188 (1965).
- MdC72 M.L. Mehta and J. des Cloizeaux, Ind. Journ. of Phys. and App. Math. **3**, 329 (1972).
- MK79 S.W. McDonald and A.N. Kaufman, Phys. Rev. Lett. **18**, 1189 (1979).
- Os68 V.I. Oseledec, Trans. Moscow Math. Soc. **19**, 197 (1968).
- Pa65 L.A. Pars, *A Treatise on Analytical Dynamics* (Wiley, New York, 1965).
- Pa79 A. Pandey, Annals of Physics **119**, 170 (1979).
- PB82 M.A. Preston and R.K. Bhaduri, *Structure of the Nucleus*, (Addison-Wesley, Reading, Massachusettes, 1982).
- Pe73 I.C. Percival, J. Phys. **B6**, L229 (1973).
- Pe83 P. Pechukas, Phys. Rev. Lett. **51**, 943 (1983).
- Pe77 Y. Pesin, Russian Math. Surveys **32** 55 (1977).

- Po65 C.E. Porter, *Statistical Theories of Spectra: Fluctuations* (Academic Press, New York, 1965).
- PR60 C.E. Porter and N. Rosenzweig, Ann. Acad. Sci. Fennicae **AVI** No. 44 (1960).
- Pr86 W.H. Press, B.P. Flannery, S.A. Teukolsky, and W.T. Vetterling, *Numerical Recipes* (Cambridge University Press, Cambridge, 1986).
- RP60 N. Rosenzweig and C.E. Porter, Phys. Rev. **123**, 853 (1960).
- RS80 P. Ring and P. Schuck, *The Nuclear Many Body Problem* (Springer-Verlag, New York, 1980).
- Sh80 R. Shankar, Phys. Rev. Lett. **45**, 1088 (1980).
- Sh81 R. Shaw, Z. Naturforsch **36a**, 80 (1981).
- SN79 I. Shimada and T. Nagashima, Prog. Theor. Phys. **61**, 1605 (1979).
- SN86 T.H. Seligman and H. Nishioka, editors *Quantum Chaos and Statistical Nuclear Physics* (Springer-Verlag, Berlin, 1986).
- SVZ84 T.H. Seligman, J.J.M. Verbaarschot, and M.R. Zirnbauer, Phys. Rev. Lett. **53**, 215 (1984).
- SV85 T.H. Seligman, J.J.M. Verbaarschot, J. Phys. **A18** 2227 (1985).
- SVZ85 T.H. Seligman, J.J.M. Verbaarschot, and M.R. Zirnbauer, J. Phys. **A 18**, 2715 (1985).
- vR82 O.S. vanRoosmalen, PhD. Thesis, University of Groningen, 1982.
- Wf79 S.S.M. Wong and J.B. French, Nucl. Phys. **A198**, 188 (1972).
- Wi57 E.P. Wigner, in *Canadian Mathematical Congress Proceedings* (University of Toronto Press, Toronto, 1957).
- Wi67 E.P. Wigner, SIAM Rev. **9**, 1 (1967).
- Wi83 R.D. Williams, Ph.D. Thesis, Caltech, 1983.
- Wi84 H.A. Weidenmüller, in Lectures given at the Cargese Summer School on Heavy Ion Reaction, 1984.

- WK82 R.D. Williams and S.E. Koonin, Nucl. Phys. **A391**, 72 (1982).
- Wo85 A. Wolf, J.B. Swift, H.L. Swinney, and J.A. Vastano, Physica **16D** 285 (1985).
- Ya82 L.G. Yaffe, Rev. Mod. Phys. **54**, 407 (1982).
- Za81 G.M. Zaslavsky, Phys. Repts. **80**, 157 (1981).